Passivation Mechanisms in the Initial Oxidation of Iron by Oxygen and Water Vapor

Passivation Mechanisms in the Initial Oxidation of Iron by Oxygen and Water Vapor

Passiveringsmechanismen in de initiële oxidatie van ijzer door zuurstof en waterdamp

(met een samenvatting in het Nederlands)

PROEFSCHRIFT

TER VERKRIJGING VAN DE GRAAD VAN DOCTOR AAN DE UNIVERSITEIT UTRECHT OP GEZAG VAN DE RECTOR MAGNIFICUS, PROF. DR. H. O. VOORMA, INGEVOLGE HET BESLUIT VAN HET COLLEGE VOOR PROMOTIES IN HET OPENBAAR TE VERDEDIGEN OP WOENSDAG 15 DECEMBER 1999 DES NAMIDDAGS TE 12.45 UUR

DOOR

Sander Jurgen Roosendaal

GEBOREN OP 19 APRIL 1972 TE AMSTELVEEN

PROMOTOR: PROF. DR. F. H. P. M. HABRAKEN
CO-PROMOTOR: DR. A. M. VREDENBERG

Faculteit Natuur- en Sterrenkunde
Universiteit Utrecht

The work described in this thesis was supported by the Dutch organization "Fundamenteel Onderzoek der Materie (FOM)"

CIP-GEGEVENS KONINKLIJKE BIBLIOTHEEK, DEN HAAG

Roosendaal, Sander

Passivation Mechanisms in the Initial Oxidation of Iron by Oxygen and Water Vapor/
Sander Roosendaal. - Utrecht : Universiteit Utrecht,
Faculteit Natuur- en Sterrenkunde, Debye Instituut
Proefschrift Universiteit Utrecht. - Met literatuuropgave.
Met samenvatting in het Nederlands.
ISBN 90-393-2250-3
Trefw.: ijzer / oxideren / dunne lagen / kinetiek / samenstelling.

Druk: Ipskamp Printpartners, Enschede

Gedanken. – Gedanken sind die Schatten unserer Empfindungen, – immer dunkler, leerer, einfacher, als diese.

Friedrich Nietzsche – Die fröhliche Wissenschaft

Contents

Chapter 1

Introduction

1.1 Background

Iron is the most abundant metal on earth and the most widely used metal for construction purposes. Steel consists for the largest part of iron. Moreover, iron is a valuable catalyst and it is important for its magnetic properties. For most of the applications of iron, corrosion (the chemical reaction of the solid with the environment [1]) is an important problem. Oxidation is one of the most important processes involved in corrosion. In the same time, the very thin (several nanometers or less) oxide layers on metal surfaces are of large practical importance: they play a crucial role in the fields of wear and friction, hydrogen embrittlement of stainless steels or poisoning of hydrogen storage materials [2]. Also in the production of modern electronic components by thin-film techniques, the importance of thin oxide films increases, due to the continuous decrease of the dimensions of the structure, down to the nanometer range.

Therefore, the growth of oxide films on iron (and other metal) surfaces has been widely studied. A large number of (experimental and theoretical) papers has appeared on the high temperature (> 500℃) interaction of several oxygen containing gases (*e.g.* O_2, H_2O vapor) with many metals and alloys. At these temperatures, the oxidation is fast and the oxide layers grown are thick and can be investigated by traditional experimental methods such as gravimetry or volumetry [2].

At temperatures below 500℃ and for thin oxide layers ($< 1\mu$m), the knowledge concerning the kinetics of the oxidation process is incomplete. Although the interactions between metal and gas for very low exposures

(several Langmuir, where a Langmuir equals 10^{-6} Torr s or 1.32×10^{-6} mbar s) has been studied widely, there are few reliable experimental studies of the oxidation kinetics after the growth of the first monolayer. The most important reason for this is that the thickness range of interest is too thick for surface science techniques (sensitive in the range of a few monolayers) and too thin for the techniques used for the study of oxidation above 500℃. Moreover, the preparation of the clean metal was only possible after the introduction of ultra-high vacuum (UHV) systems.

Another reason why the study of the low temperature oxidation of iron is interesting is that the range of possible oxide phases formed is large. From a thermodynamical point of view, α-Fe_2O_3 and α-FeOOH are the most stable oxides. For the room temperature oxidation of iron in O_2, one would expect a thin layer of Fe_3O_4 to be formed, followed by α-Fe_2O_3. Fe_xO (with x between 0.9 and 0.95) is not stable at temperatures lower than 560℃ (833K). However, the Gibbs free energies of the reactions between iron and oxygen or iron and water vapor forming the different oxides may very well be changed by interfacial effects and finally, kinetic barriers may prevent the thermodynamically most stable oxide to be formed. At low H_2O vapor pressures at room temperature, for example, FeOOH is not stable with respect to the reaction $2\text{FeOOH} \rightarrow Fe_2O_3 + H_2O$. (The Gibbs free energy of the reaction has a very low value of $\Delta_r G \approx 5.7$ kJ/mole [3].) However, Goethite (FeOOH) is found to be one of nature's most stable oxides. Furthermore, there is a distinct particle size effect on the value of $\Delta_r G$ [3] for this dehydration reaction, which is an indication of a strong interface energy effect, possibly making FeOOH more stable. Arguments based on epitaxy pro and contra the formation of different oxide phases are not decisive, either: most bulk oxide lattices (Fe_xO, γ-Fe_2O_3, α-Fe_2O_3, Fe_3O_4, FeOOH) fit on Fe(100) with lattice mismatches of less than 5%.

Despite the scarcity of experimental data, a number of oxidation models has evolved during the last 40 years. These are extensively treated in a number of reviews and monographs [1,4]. A special place among these (early) theories is taken by the so-called Fromhold-Cook theory (FC) [1]. This theory is not only physically consistent, it can also be shown that, in limiting cases, it reduces to several of the more phenomenological relations used to explain experimental results, such as direct logarithmic oxidation (where the film thickness L is proportional to the logarithm of time, $\log t$), inverse logarithmic oxidation ($1/L \propto \text{const} - \log t$) or square root oxidation

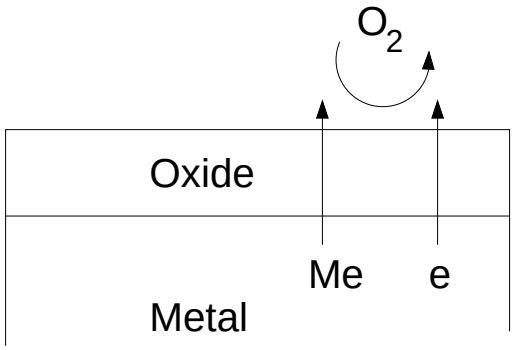

FIGURE 1.1: A schematic representation of the initial oxidation of a metal in O_2.

($L \propto \sqrt{t}$) [1]. The Fromhold-Cook theory accounts for the transport processes of ions, electrons and atoms from the metal and from the gas phase into and (if necessary) through the oxide. In the FC-theory, the reaction between metal and oxygen takes place at the growing oxide/oxygen interface, requiring both metal ions and electrons to move through the oxide layer to the surface, as is shown schematically in figure 1.1. An important feature of the FC theory is the concept of coupled currents: the net electrical current across the oxide layer is zero. At sufficiently high oxygen pressures, transport of either electrons or metal ions is rate limiting. In the FC-model, the transport of electrons can proceed by two mechanisms: tunneling and thermionic emission. For temperatures below ∼150℃ (∼420K), there is virtually no thermionic emission at the metal-oxide interface, and electron tunneling is the dominant process. Above this temperature, the thermionic emission current of electrons increases rapidly and becomes the dominant electron transport mechanism at layer thicknesses above oxide thicknesses of approximately 2 nm.

By a smart combination of surface sensitive and ion beam techniques (which give accurate results in the thickness region between 1 monolayer and several hundreds of nm), Leibbrandt *et al* [5,6] have shown that the oxidation of Fe(100) in O_2 forms a model system for the Fromhold-Cook theory: above 150℃, all the requirements for the application of the theory are met: the oxide layers grown are flat and homogeneous and the transport of Fe cations from the Fe/oxide interface – through the oxide – to the surface of the growing oxide accounts for the mass transport needed for

the reaction. Furthermore, on the kinetics the theory proved to be fully consistent with the experimental data: after an initial stage in which the reactants (O_2) supply is rate limiting (due to the low pressures applied), a stage is reached in which the oxidation rate is determined by the electron transport from the metal to the oxide surface, which at these temperatures proceeds by thermionic emission. Calculations based on the thermionic emission of electrons (and taking into account the transport of Fe cations through the oxide layer as well) are in quantitative agreement with the appropriate measured data. In this way, Leibbrandt and co-workers were able to determine the (realistic) values of a number of important parameters in the FC theory, valid for oxidation temperatures above 150℃. At lower temperatures, the predicted (almost complete) saturation was found, *i.e.* the oxidation rate decreases almost completely to zero at a certain oxide thickness. However, the FC theory predicts that this saturation thickness is independent of the oxidation temperature. Although there was a qualitative agreement between the oxidation curves and the model, this temperature independence was not observed.

Similar experiments were carried out by Görts *et al* on low-index Co single crystal surfaces [7]. Again, the system was shown to meet all the requirements for the application of the FC model and, indeed, qualitative agreement was found between the oxidation curves and the FC model. In the low temperature regime, however, again the FC theory could not predict the observed changes in the saturation thickness.

The dependence of the saturation thickness on temperature is one aspect of the seeming contradictions between FC theory and experiment which will be treated in this thesis. It will be shown that this conflict can be solved when the (changing) electronic structure of the oxide is taken into account.

Another drawback of the FC theory is that it does not take into account the kinetics of the processes at the surface of the growing oxide. However, the establishment of the kinetic potential needed in the theory is a reaction between electrons in the bulk and acceptor species on the oxide surface. Furthermore, the equilibrium concentration of ions in the oxide layer can be a result of surface reactions. Especially at low temperatures, these surface reactions may proceed slow enough to change the local equilibria of charged species in the surface region of the sample and thus change the kinetics of the oxidation process. Fromm [2] has recognized this problem

and proposed a model incorporating rate equations of surface processes into the FC theory, thus obtaining a model which (in principle) describes the complete oxidation, starting from an almost uncovered clean metal surface and ending with extremely slow reaction rates after the formation of a several nm thin oxide layer.

In this thesis, it will be shown that the equilibrium of species at the surface of the growing oxide is very important for the oxidation of iron in H_2O vapor: surface reactions have to be considered in a description of the oxidation process. We will even show that an oxidation model taking into account *only* surface reactions (and not the transport properties of the oxide layer) is sufficient to describe the measured oxidation curves.

1.2 Goal, Definitions and Outline

The goal of the work presented in this thesis was to study the low temperature (< 150℃) oxidation of low-index iron single crystal surfaces in O_2, H_2O vapor, and O_2/H_2O vapor mixtures and to find the origin of the disagreement between the FC theory and the results found for Fe (and, possibly, Co). Roughly speaking, there are two possible causes for the disagreement: either the theory is wrong or the system studied is not a model system for the low temperatures. Therefore, we assessed whether the oxide layers grown at low temperatures are flat and homogeneous. We also attempted to determine the moving species during the growth of the thin (0-4 nm) oxide layers. We applied MeV ion beam methods for the accurate determination of H, O and Fe areal densities in the oxide layer, ellipsometry for the *in-situ* measurement of the oxidation rate and oxide thickness and quantitative X-ray Photoelectron Spectroscopy (XPS) for the determination of the oxidation state of Fe atoms in the oxide layer and possible identification of OH groups. The determination of the moving species was done in an experiment in which we combined nitrogen deposition to form a marker layer, quantitative XPS and Elastic Recoil Detection (ERD) for the determination of the nitrogen coverage. By monitoring the evolution of the XPS N(1s) signal, results were obtained on the mass transport during the oxidation.

By studying the oxidation mechanism and the oxidation rate in H_2O vapor and O_2/H_2O mixtures, we attempted to resolve the importance of surface processes in the oxidation. The dissociation of H_2O on the surface of

the growing oxide is expected to proceed much slower than that of O_2 [8,9]. At the same time, the oxide layer formed in H_2O may be different from the oxide layer formed in O_2 (stoichiometry, Fe oxidation state, H content), leading to different (ion and electron) transport properties. Again, our aim is to determine the nature of the mass transport during oxidation and the rate-limiting step in the oxidation process.

In this work, we concentrate on experiments on Fe(100). For comparison, some experiments were performed on Fe(110).

The saturation thickness is a very important parameter for comparison between oxidation theory and measurement. A correct definition would be the oxide thickness which is reached asymptotically for $t \to \infty$ (with t the oxidation time). Because of the limited time that was available for this project, we will work with a different definition: Saturation means that the oxygen incorporation rate has decreased to 10^{11} atoms cm^{-2} s^{-1}. As can be seen from most oxidation curves or plots of the oxygen incorporation rate vs. the oxygen coverage in this thesis, our definition coincides with the "intuitive value" for the "real" saturation coverage or thickness. Passivation means the saturation of the reaction due to (properties of) the oxide layer formed.

Other terms which need definition are the *rate-limiting step* and the *rate-determining steps* of the oxidation reaction. As mentioned above, the oxidation process can be divided into many subprocesses, such as arrival of molecules from the gas phase, establishment of a surface equilibrium of species by surface reactions and reactions with electrons and ions arriving from or leaving into the oxide layer, and finally the transport of electrons and ions through the oxide layer. The *rate-determining steps* are the subprocesses which are sufficient (and necessary) to describe the observed oxidation rates. The *rate-limiting step* is the rate-determining step with the lowest rate constant. Consequently, during the oxidation process a balance of species is established in such a way that the rate-limiting step proceeds at the maximum possible rate. As can be seen in chapter 7, the relatively fast arrival, dissociation, recombination and desorption of H_2O molecules determine the OH coverage on the surface. Slow steps in the reaction are the dissociation of OH at oxide island edges, leading to typical nucleation and growth kinetics, and (at temperatures below 340K) the desorption of H_2. The oxidation rate is determined by the product of the OH coverage

and the rate constant for island growth. Similarly, in chapter 5, the oxidation kinetics for the growth of FeO can be fully described (above a certain oxide thickness) by the transport of electrons and Fe cations through the oxide layer: these are the rate-determining steps. At low temperatures, it is found that the rate-limiting step is the diffusion of Fe cations (up to the saturation thickness, where the electron tunnel current decreases rapidly and becomes rate-limiting). At temperatures above 150℃, we found that the rate-limiting step is the thermionic emission of electrons into the conduction band of the oxide.

In chapter 2, an overview is given of the experimental techniques used and the UHV system in which the experiments were performed. We give the basic equations for the interpretation of the experimental data and perform a calibration (using ERD) of the ellipsometer needed to quantify the results. The experimental parameters for our experiments are given.

Chapter 3 deals with quantitative XPS and the quantification of the mean escape depth of photoelectrons from iron oxide layers, needed to quantify our XPS results.

In chapter 4, we investigate the nature of the oxide layer grown in O_2. Analysis of XPS, ERD and ellipsometry results leads to conclusions about the refractive index of the oxide layer grown and the oxidation state of Fe atoms in the oxide layer as a function of depth and temperature. Furthermore, using a marker layer consisting of nitrogen atoms deposited at the the Fe(100) substrate before oxidation and (angle-dependent) quantitative XPS to monitor the evolution of the nitrogen signal as the oxide grows, we obtain information about the moving species during oxidation (O anions or Fe cations) and the oxidation mechanism at room temperature.

In chapter 5, experiments are presented to correlate the oxide electronic structure and stoichiometry (chapters 3 and 4) with the oxidation rate. The most important equations for the calculation of theoretical oxidation rates in the FC model are given and calculated oxidation rates are compared with the experimental results. It will be shown that the growth of a homogeneous FeO layer on Fe(100) is described accurately and consistently by the FC model.

The oxidation of Fe in H_2O and H_2O/O_2 mixtures is treated in chapters 6 and 7. Chapter 6 deals with the room temperature (35℃, or 308K) oxidation of Fe(100) and Fe(110) in H_2O and D_2O. Also results on the

oxidation in H_2O/O_2 mixtures (at room temperature) and oxidation in O_2 after pre-oxidation in H_2O vapor (also at room temperature) are presented. The importance of the different surface and transport processes and the identity of the rate-limiting step are discussed and it is shown that the oxidation rate is dominated by the rates of surface processes such as, for example, the dissociation of H_2O molecules. Further investigations of the initial oxidation of Fe(100) in H_2O vapor, presented in chapter 7, involve the temperature and pressure dependence and the oxidation (in H_2O) of Fe(100) modified with nitrogen atoms at the surface. Finally, all observations are combined in a quantitative kinetic model for the oxidation. The ingredients of this model are the surface equilibrium of H_2O and its dissociation products and the nucleation and growth kinetics of oxide islands. The importance of the hydrogen desorption rate for the oxidation process is shown.

Chapter 2

Methods and Experimental Techniques

2.1 The Octopus

The study of surfaces and low-pressure surface reactions requires both ultra-high vacuum (UHV) and a multi-technique approach. Most surface analytical techniques involve the bombardment of the surface with (high energy) particles (photons, electrons or ions, with typical energies ranging from 1 keV to several MeV). The energy flux to the sample is much larger than the energies involved in the reactions studied. Therefore, these techniques influence the reactions studied. Moreover, by using electrons as probe, the charge balance, which turns out to be very important in the oxidation of metals [1,6,7,10], is changed. These problems can be avoided by using light as probe for the *in-situ* study of the reaction (ellipsometry). The quantification of the optical measurements and the structural analysis of the sample after reaction is then carried out via different surface analytical techniques present in the same vacuum system.

The experiments described in this thesis were carried out in the OCTOPUS which is a multi-chamber UHV preparation and analysis system connected to both a 3 MV single ended and a 6 MV Tandem Van de Graaff generator. The system contains among others facilities for Auger Electron Spectroscopy (AES), combined with sputtering, High-Energy Ion Scattering with Shadowing and Blocking (HEIS-SB), Elastic Recoil Detection analysis (ERD), X-ray Photo-electron Spectroscopy (XPS) and ellipsometry. The base pressure is in the 10^{-10} mbar region. A schematic

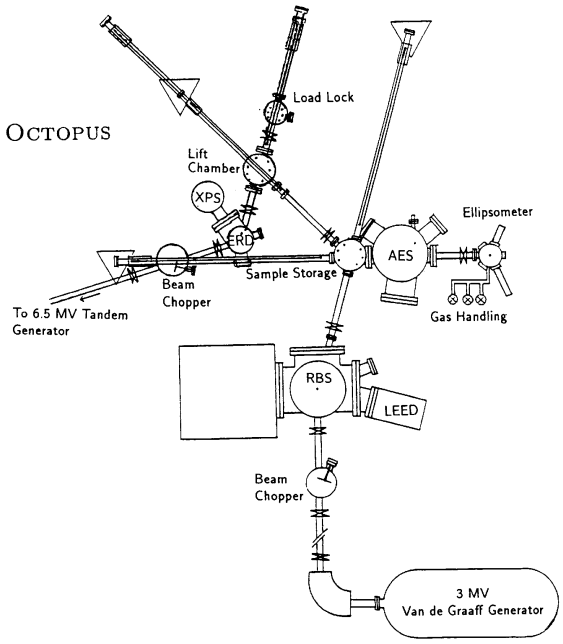

Figure 2.1: A schematic overview of the Octopus multi-chamber UHV system

overview of the Octopus is given in figure 2.1.

2.2 Sample Preparation

We obtained Fe(100) single crystals (10mm diameter × 1mm, purity 3N8) from the Surface Preparation Laboratory in Amsterdam. The surface orientation was 0.1° accurate (measured with Laue diffraction). These crystals were cleaned in situ by repeated Ar bombardment and annealing cycles (700K), as suggested by Musket *et al* [11]. After this, no contamination peaks were present in the AES spectrum. ERD measurements showed that there was an upper limit to the remaining carbon contamination of approximately 0.06 at% in the first 100 nm of the iron crystal.

2.3 Gas Exposure

Gas exposure was performed in a UHV chamber in the OCTOPUS with a base pressure of 10^{-10} mbar. The chamber is connected to a gas inlet system which can be filled with several high purity gases (for example H_2, O_2, $^{18}O_2$, CO and N_2). The chemical purity of the $^{16}O_2$ gas was 99.995%. The amount of $^{18}O_2$ in the $^{16}O_2$ gas was below the natural isotope abundance of 0.2%. The chemical purity of the H_2 gas was 99.999%.

The gas was introduced into the chamber through a Varian variable leak valve under constant flow, *i.e.* the chamber was continuously pumped during the gas exposure.

A special inlet system was designed for water vapor. This inlet system is connected to a glass bottle containing distilled water and is pumped by a cryopump. Water vapor is produced by pumping down the inlet system to remove the air which is dissolved in the water. The water vapor was introduced into the vacuum chamber through a Varian variable leak valve under constant flow.

A similar inlet system was used for the production of D_2O vapor from high purity (99.9%) D_2O.

The partial gas pressures were measured using a Balzers QMG-064 electrostatic quadrupole mass spectrometer. To prevent dissociation of the water molecules on the filaments, we switched off all ion gauges during the oxidation. To measure the high pressures ($>10^{-4}$ mbar) often used in the reduction experiments, we used a (Leybold) Pirani gauge.

The sample temperature was monitored with a Chromel-Alumel thermocouple, firmly pressed to the back of the sample to ensure a good thermal contact. The sample was heated by a thermo-resistive wire that is coiled around the sample holder. The heating power was controlled by an electronic PID (Proportional Integral Derivative) feed-back system. Once the temperature was stabilized, temperature fluctuations remained within 2°.

2.4 Auger Electron Spectroscopy

We used Auger Electron Spectroscopy (AES) to investigate the surface contamination of the sample. Auger spectra were recorded with a RIBER OPC-105 Cylindrical Mirror Analyzer (CMA) with an internal electron gun, operated at 1500 V. A modulation voltage was applied and lock-in-

detection was used, so the spectra were obtained in derivative ($E \cdot \frac{dN}{dE}$) mode. Usually, the Fe LMM, O KLL, C KLL, N KLL, and S KLL Auger electron peaks were measured.

2.5 Ellipsometry

During the exposure to gases, ellipsometry was used to study processes taking place at the surface of the sample. Ellipsometry is an optical technique for the characterization of processes taking place at an interface or film between two media and is based on the polarization changes that occur as a beam of polarized light is reflected through the interface or film. Two factors make ellipsometry a suitable tool to study the growth and reduction of thin oxide layers: **(1)** its essentially non-perturbing character, hence its suitability for *in-situ* experiments, and **(2)** its remarkable sensitivity to minute interfacial effects, for example the formation of a sub-monolayer of atoms or molecules.

2.5.1 Theoretical Background

The amount of reflection of the two components of a polarized electromagnetic wave (denoted E_s and E_p for polarization perpendicular and, respectively, parallel to the plane of incidence) is calculated by solving the Fresnel equations. The relation between the complex Fresnel-reflection coefficients r_s and r_p and the ellipsometry parameters Δ and Ψ is given by the Drude equation [12] as:

$$\rho \equiv r_p/r_s = \tan(\Psi)\exp(i\Delta) \tag{2.1}$$

The relation between the change in the electromagnetic field and the Fresnel coefficients is given by:

$$r_p = \frac{|E_p'|}{|E_p|}\,\mathrm{e}^{i(\delta'-\delta)_p} \quad \text{and} \quad r_s = \frac{|E_s'|}{|E_s|}\,\mathrm{e}^{i(\delta'-\delta)_s} \tag{2.2}$$

where the prime denotes the field after reflection, δ and δ' are the phase factors and $|E_{s,p}|$ and $|E'_{s,p}|$ are the amplitudes. For an electromagnetic wave traveling through a medium 0 and refracted at the interface with medium 1, the Fresnel-coefficients are given by:

$$r_p = \frac{N_1\cos\phi_0 - N_0\cos\phi_1}{N_1\cos\phi_0 + N_0\cos\phi_1} \quad \text{and} \quad r_s = \frac{N_0\cos\phi_0 - N_1\cos\phi_1}{N_0\cos\phi_0 + N_1\cos\phi_1} \tag{2.3}$$

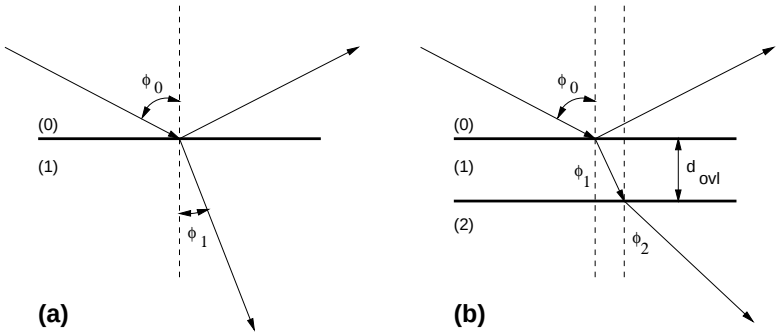

FIGURE 2.2: Reflection and transmission of a plane wave **(a)** at the interface between two semi-infinite media, and **(b)** by an ambient(0)-film(1)-substrate(2) system with parallel-plane boundaries. d_{ovl} is the film thickness. ϕ_0 is the angle of incidence in the ambient and ϕ_1 and ϕ_2 are the angles of refraction in the film and substrate.

where N_0 and N_1 are the indices of refraction in medium 0 and 1, respectively, and ϕ_0 and ϕ_1 the angles of incidence and refraction, as is depicted in figure 2.2 **(a)**.

The combination of equation (2.2) with the Drude equation (2.1) gives:

$$\Delta = (\delta' - \delta)_p - (\delta' - \delta)_s \tag{2.4}$$

$$\tan(\Psi) = \frac{|E'_p|/|E_p|}{|E'_s|/|E_s|} \tag{2.5}$$

This shows that Δ is related to the phase change and Ψ is related to the amplitude change.

Ellipsometry is often used to study the rates of changes taking place at or near the surface. Therefore it is customary to use $\delta\Delta$ and $\delta\Psi$ instead of Δ and Ψ. The definitions of $\delta\Delta$ and $\delta\Psi$ are:

$$\delta\Delta \equiv \Delta_0 - \Delta(t) \tag{2.6}$$

$$\delta\Psi \equiv \Psi_0 - \Psi(t) \tag{2.7}$$

with Δ_0, Ψ_0 the initial values and $\Delta(t)$, $\Psi(t)$ the values at time t.

If the growth of a thin oxide layer on a metal substrate is studied, a simple flat layer model is often used to describe the relation between $\delta\Delta$

and $\delta\Psi$ and the physical thickness (or oxygen coverage) of the oxide layer. The three phases present are the oxidizing gas (O_2 or H_2O) (medium 0), the growing oxide layer (medium 1) and the metal substrate (medium 2), as indicated in figure 2.2 **(b)**. Assuming that the metal substrate and the oxide layer are flat, the Fresnel equations can be solved [12]. Equations (2.1), (2.2), (2.4) and (2.5) now apply for the *resultant* reflected wave and the *overall* Fresnel reflection coefficients R_p and R_s, which are given, in terms of the reflection coefficients at the two interfaces, by:

$$R_p = \frac{r_{01p} + r_{12p}\mathrm{e}^{-i2\beta}}{1 + r_{01p}r_{12p}\mathrm{e}^{-i2\beta}} \quad \text{and} \quad R_s = \frac{r_{01s} + r_{12s}\mathrm{e}^{-i2\beta}}{1 + r_{01s}r_{12s}\mathrm{e}^{-i2\beta}} \tag{2.8}$$

where $r_{01p,s}$ and $r_{12p,s}$ are the Fresnel reflection coefficients at the 0-1 and 1-2 interface, respectively (see figure 2.2). The phase angle β for a layer of thickness d_{ovl} and complex index of refraction N_1 is given by:

$$\beta = 2\pi\left(\frac{d_{\mathrm{ovl}}}{\lambda}\right)\sqrt{N_1^2 - N_0^2 \sin^2\phi_0} \tag{2.9}$$

where λ is the wavelength of the polarized light.

Figure 2.3 shows an example of such a calculation ($\delta\Delta$ and $\delta\Psi$ vs. the physical thickness of the oxide layer). The values for the optical constants used in the calculation are $N_0 = 1.0$ for the oxygen ambient, $N_1 = 2.32$ for the overlayer and $N_2 = 3.21 - i3.66$ for the substrate. These values are appropriate for the growth of FeO on Fe, as will be shown in section 4.3. The angle of incidence ϕ_0 amounted to 70° and the wavelength of the light used for the calculation was 632.8 nm, in accordance with the values for our experimental setup.

As can be seen from figure 2.3, the relation between $\delta\Delta$ and $\delta\Psi$ and physical thickness is approximately linear for thin oxide layers ($\leq$ 40 nm for $\delta\Delta$ and $\leq$ 20 nm for $\delta\Psi$). The approximate relation between the ellipsometry parameters and the overlayer thickness d_{ovl} are given by:

$$\delta\Delta = S_\Delta d_{\mathrm{ovl}} \tag{2.10}$$

$$\delta\Psi = S_\Psi d_{\mathrm{ovl}} \tag{2.11}$$

If the optical constants of the substrate and overlayer are known, S_Ψ and S_Δ are easily calculated. The optical constants of bulk iron oxides are known. The structure of thin oxide layers on iron may however differ from known oxides. Therefore, the measured values of $\delta\Delta$ need to be calibrated.

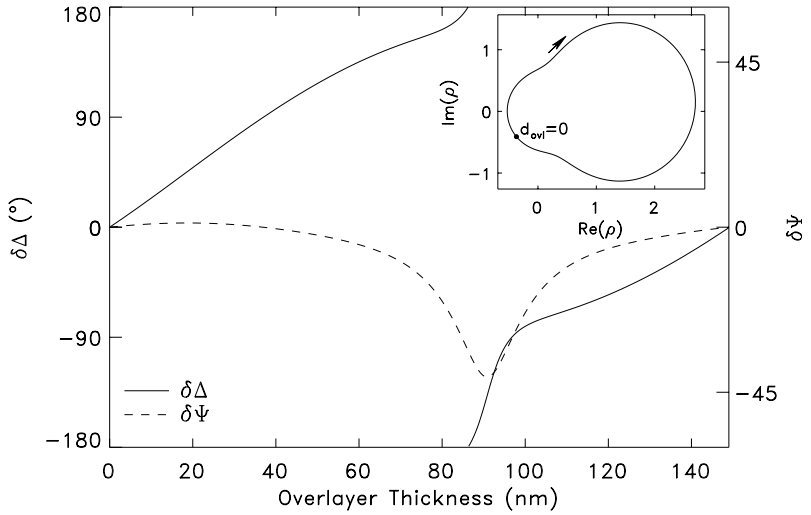

FIGURE 2.3: The calculated relation between $\delta\Delta$ and $\delta\Psi$ and the thickness of the overlayer for the FeO/Fe system. Inset: Polar curve for ρ for the given system. The arrow indicates the direction of increasing overlayer thickness (d_{ovl}). (See text for details of the calculation.)

This flat-layer model is of course a simplified representation of the complex change in the electronic structure of the sample taking place during the oxidation. More complicated situations are also encountered. The growth of the first monolayer of oxide, for example, will cause a simultaneous change in the electronic structure of the top layer of Fe in the substrate. Also the creation of surface defects by ion bombardment results in deviations from the simple model [13]. Finally, the result of exposure to oxygen is not necessarily a flat oxide layer. At higher oxidation temperatures, for example, oxygen is known to diffuse into the bulk of the substrate, and again the flat-layer model is not appropriate. In these cases a careful calibration of $\delta\Delta$ and $\delta\Psi$ is especially important.

2.5.2 Calibration of the Ellipsometer

Solutions of the ellipsometry equations (2.1) and (2.2) yield an approximately linear dependence of $\delta\Delta$ on the thickness of the oxide layer, for

$d_{\mathrm{ovl}} \leq 40$ nm, *i.e.* for all layer thicknesses considered in this work. The value of the proportionality constant S_Δ depends on the complex indices of refraction of the substrate and the overlayer. Using ellipsometry, we determined the substrate index of refraction to be:

$$N_2 = (3.22 \pm 0.05) + i(3.67 \pm 0.05)$$

for both Fe(100) and Fe(110). This is close to the values found in literature ($N_2 = 2.86 + i3.36$ [14], $N_2 = 2.88 + i3.05$ [15]). The uncertainty in our value for N_2 is due to uncertainties in the ellipsometry angle (which amounted to $70.0 \pm 0.2^{\mathrm{o}}$).

In figure 2.4 **(a)** measured values of $\delta\Delta$ for the initial oxidation of Fe(100) and Fe(110) are plotted against the oxygen coverage measured with ERD (for oxidation temperatures between room temperature and 475K and oxygen pressures between 10^{-8} and 10^{-5} mbar). Because we do not measure the physical thickness of the oxide but the oxygen coverage (in atoms/cm^2), we cannot determine S_Δ. Instead, by fitting a linear function to the data points we obtain the proportionality constant F_Δ, defined as:

$$F_\Delta \equiv \delta\Delta / N_{\mathrm{O}} = S_\Delta / \rho_{\mathrm{O}} \tag{2.12}$$

where N_{O} is the oxygen coverage and ρ_{O} is the volume density (in atoms cm^{-3}) of oxygen in the oxide layer. The experimental value for F_Δ obtained from the fit in figure 2.4 **(a)** amounted to $(0.426 \pm 0.010) \times 10^{-15}$ $^{\mathrm{o}}$cm^2/atom.

The fit in figure 2.4 **(a)** has a positive offset on the x-axis. Consistent with this, we observed that the parameter $\delta\Delta$ changed only slowly during exposure to the first 3 Langmuir of oxygen exposure. Apparently, the parameter $\delta\Delta$ is not sensitive to the first monolayer of (chemisorbed) oxygen. This insensitivity of ellipsometry for chemisorbed oxygen has been reported before by Vink *et al* [16,17]. A possible explanation for the slow change of Δ during the growth of the first monolayer is given by a model developed by Habraken *et al* [18,19]. This model not only considers the overlayer but also takes into account changes in the substrate. The first monolayer of oxygen forms a dipole layer with the iron atoms, changing the optical properties of the substrate. The value of $\delta\Delta$ is then the sum of two contributions: a change in Δ caused by a change in the substrate and a change in Δ, of opposite sign, caused by the uptake of oxygen, resulting in a low net value of $\delta\Delta$.

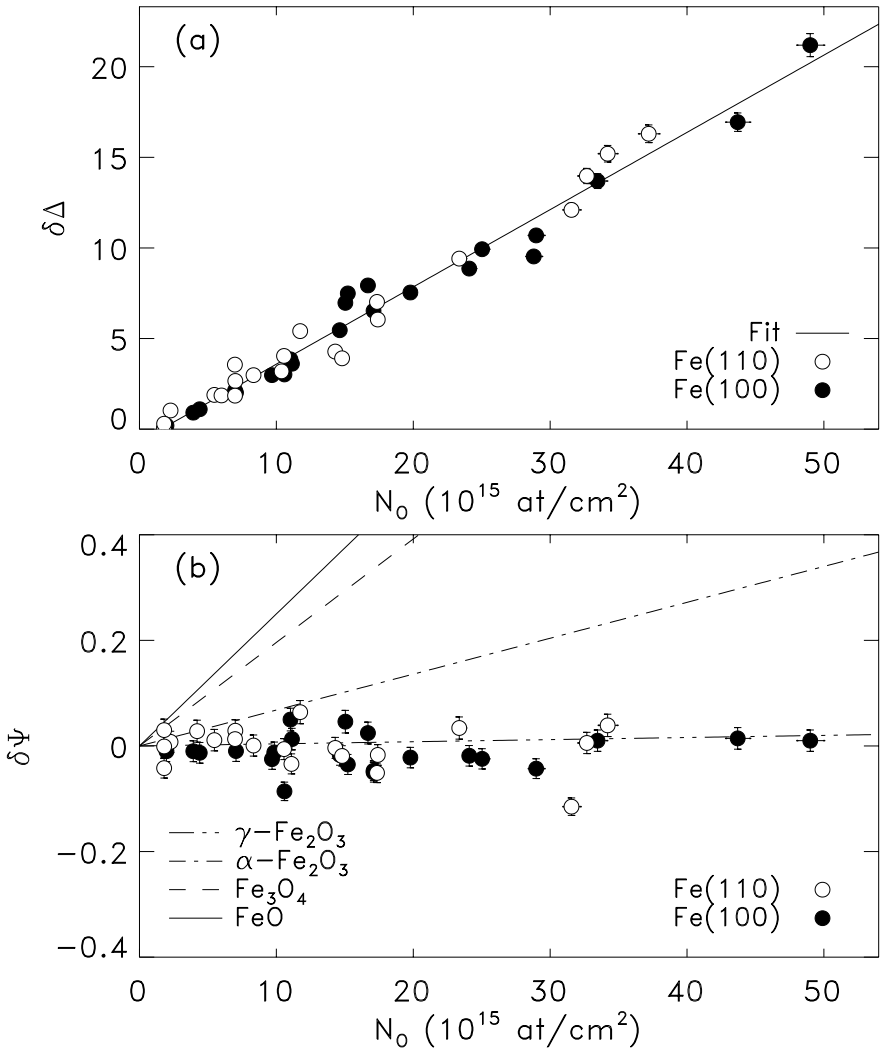

FIGURE 2.4: **(a)** $\delta\Delta$ vs. oxygen coverage determined with ERD (calibration curve for the ellipsometer). Open circles: oxidation of Fe(110). Closed circles: oxidation of Fe(100). Solid line: fit to the data (see text). **(b)** $\delta\Psi$ vs. oxygen coverage. Lines: expected dependence for several bulk oxides (discussed in section 4.3.2).

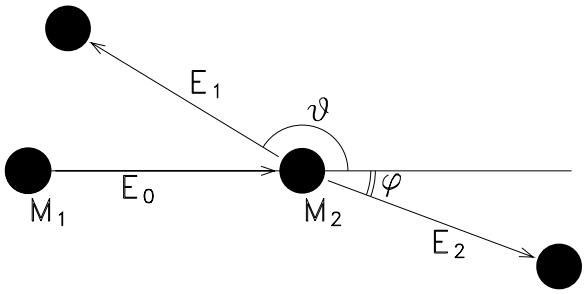

FIGURE 2.5: The elastic collision.

In a similar manner, a value for F_Ψ was obtained from a fit to the values of $\delta\Psi$ after oxidation, shown in figure 2.4 **(b)**. The value of F_Ψ thus determined amounted to (-2±5)×10^{-19} ^{o}cm^2/atom. A more detailed discussion is given in section 4.3.2.

2.5.3 Experimental Setup

Ellipsometry was done using a SOFIE STE 70 TURBO rotating birefringent ellipsometer [12], equipped with a fast rotating 5/4λ mica plate. A He-Ne laser with a wavelength of 632.8 nm was used as light source. The angle of incidence was 70° with respect to the sample normal. The calibration of the ellipsometer was performed using a Si substrate covered with a SiO_2 layer of known thickness, as prescribed by the manufacturer.

2.6 Ion Beam Methods

High energy (several MeV) ion beams are very useful for the characterization of materials. Rutherford Backscattering Spectrometry (RBS) and Elastic Recoil Detection (ERD) share the advantage of being accurate and quantitative spectroscopic techniques giving spectra which are easy to interpret.

In ion beam analysis, a beam of high energy ions from an accelerator is directed towards the sample. The energy of the accelerated ions is typically 1 MeV/amu. In the surface region of the sample (∼first μm, depending on

the actual primary ion, geometry, and energy), the ions collide with atoms in the sample. For these energies, the interactions between the ion and the sample atom are described well by a Coulomb repulsion between the two nuclei. After the collision (depicted in figure 2.5), the energy E_1 of the primary particle with mass M_1 and energy E_0, scattered over an angle θ, and the energy E_2 of the recoiled sample atom with mass M_2 can be calculated using conservation of energy and momentum. The kinematic factors, defined as the ratio of the particle energies before and after the collision, depend on M_1 and M_2 and the scattering angle θ or the recoil angle ϕ. Also the cross-section for the scattering and recoil processes can be expressed exactly and are functions of M_1, M_2, the atomic numbers Z_1 and Z_2, the primary energy E_0 and the geometry. For a more detailed discussion and expressions we refer to the literature [20–23].

2.6.1 High Energy Ion Scattering with Shadowing and Blocking

High Energy Ion Scattering with Shadowing and Blocking (HEIS-SB) is a method to enhance the surface sensitivity of RBS for monocrystalline samples. The scattered projectile (usually a light element, for example He) is detected over a scattering angle θ. Both the ion beam and the detector are aligned in the direction of one of the major crystallographic axes in the sample [24,25]. This reduces the spectral contribution of the crystalline substrate by a factor of $\sim$100. There remains a full interaction with the first monolayers of the solid and with atoms which are not on lattice positions, for instance in an amorphous or polycrystalline oxide layer or due to surface damage by ion sputtering. This is shown in figure 2.6 **(a)** for clean Fe(100).

To determine the amount of iron atoms (per unit area) in the surface peak, a background has to be subtracted, as is shown in figure 2.6 **(b)**. A step function and a second order polynomial are used for the background. The number of visible iron atoms is now given by:

$$N_{\mathrm{Fe}} = \frac{A\xi}{H_0 S_{\mathrm{Fe}}} \tag{2.13}$$

where A is the area of the surface peak, H_0 is the height of the random spectrum (evaluated at the surface energy), ξ is the energy width of one channel of the multichannel analyzer, and S_{Fe} is the energy loss factor. (The energy loss factor is a factor relating an energy difference in the spectrum

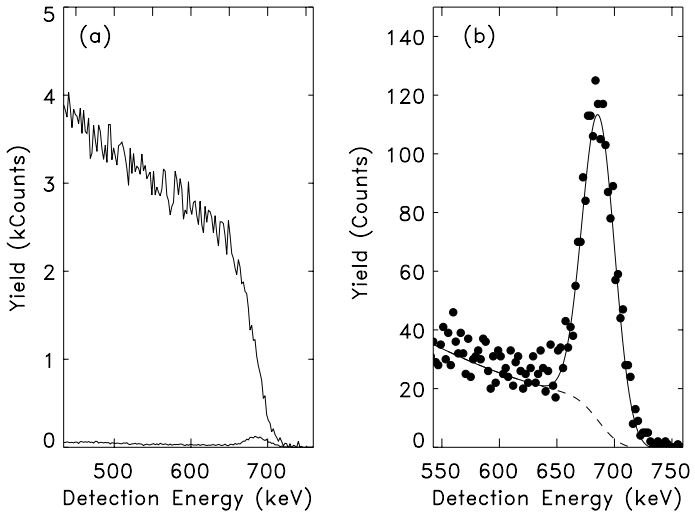

FIGURE 2.6: HEIS-SB spectra of a clean Fe(100) sample. **(a)** Random direction and $[\bar{1}11] \rightarrow [111]$ double alignment, showing the effect of shadowing and blocking. **(b)** Double alignment spectrum. The solid line represents the result of a fit to the data, with the dashed line representing the background contribution.

to a depth interval in the sample, usually expressed in eV/(at cm^{-2})). To determine the coverage of a different element (*e.g.* oxygen), from its peak area, equation (2.13), multiplied by the ratio of the cross-sections ($\sigma_{\mathrm{Fe}}/\sigma_{\mathrm{O}}$) is used.

For all HEIS-SB experiments on Fe(100) described in this thesis, we used a 750 keV He^+ beam. Backscattered particles were detected using an ion-implanted Si detector. The beam was aligned in the direction of the $[\bar{1}11]$ crystal axis while aligning the detector in the direction of the the [111] axis. A beam chopper was used to determine the projectile fluence. The random spectrum was obtained by rotating the sample around the normal axis during the measurement (while keeping the scattering geometry fixed).

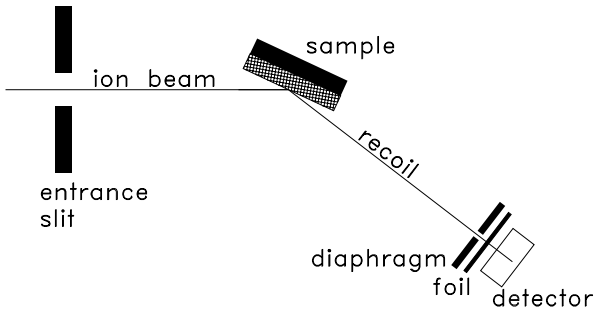

FIGURE 2.7: Set-up for conventional ERD experiments.

2.6.2 Elastic Recoil Detection

Principle and Experimental Setup

Heavy ion ERD is the complementary technique of Rutherford Backscattering Spectrometry (RBS) [26]. It combines the quantitative properties of MeV scattering techniques with an excellent sensitivity for light elements (including hydrogen) at and below the surface [22]. In ERD, recoiled particles are detected in a forward direction with recoil angle ϕ, as is shown in figure 2.7. We used different ion beams from the 6.5 MV Tandem accelerator (*e.g.* 28 MeV Ag^{6+}, 35 MeV Cl^{6+}, 2.13 MeV He^{+}). Recoils created by binary collisions with primary ions were detected at a forward angle of 37.5° with the incoming beam, and the angle of the incoming beam with the target surface amounted to 25°. A beam chopper in combination with a 30 nm SiO_2/Si or a 75 nm Si_3N_4:H (3at%) reference sample was used to determine the projectile fluence. To prevent flooding of the detector with scattered projectiles, a 11.2 μm thick mylar foil was placed in front of the detector. Also the recoils lose energy while traversing the foil, and therefore the resulting detection energy is not determined solely by the kinematic factor.

ERD Spectra of thin Oxide Layers on Fe

ERD is especially useful for the detection of light elements in a heavy matrix, as for example hydrogen and oxygen in iron oxide. As an example,

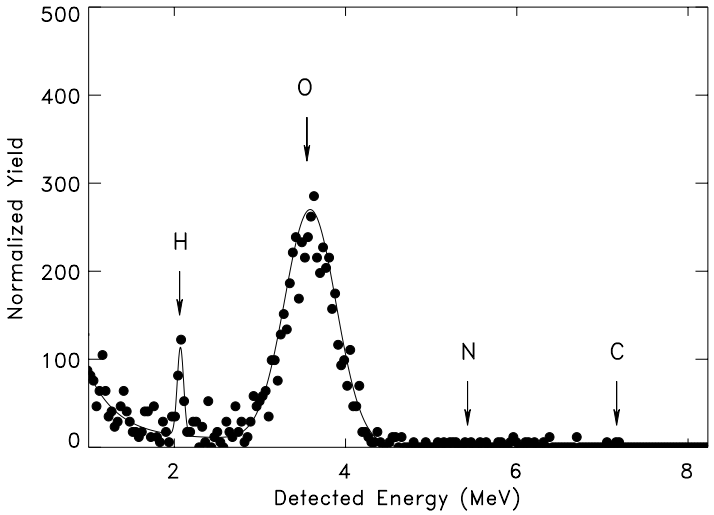

FIGURE 2.8: The ERD spectrum of Fe(110) oxidized at RT for 105 min in oxygen at 10^{-6} mbar. The oxygen areal density is 10.9×10^{15} atoms/cm^2. A solid line to guide the eye is plotted.

the ERD spectrum of Fe(110) after exposure to 4790 L of O_2 at RT is given in figure 2.8. The spectrum was measured using a 36 MeV Cl^{6+} beam. Surface energies of the light elements are indicated. The contribution at lower energy is due to multiple scattering events in the mylar foil. From the peak integral the areal density of the respective element is determined. The quantitativity of the technique is based on the knowledge of the recoil cross section of high energy ions. For oxygen, amounts of 10^{14} atoms/cm^2 are determined with an accuracy of about 5×10^{13} atoms/cm^2. The width of the peak is determined by the energy resolution of the detection setup and, therefore, does not yield information on the depth distribution of oxygen in this case. In these analyses the depth resolution for oxygen and nitrogen amounts to ∼25 nm. The width of the hydrogen peak is smaller (less straggling in the foil), but due to a very low energy loss factor S, this corresponds to a worse depth resolution (∼60 nm). In the case of figure 2.8 the oxygen areal density is 10.9×10^{15} atoms/cm^2, while that of hydrogen (which must be present in the surface region of the sample) is 4.3×10^{14} atoms/cm^2.

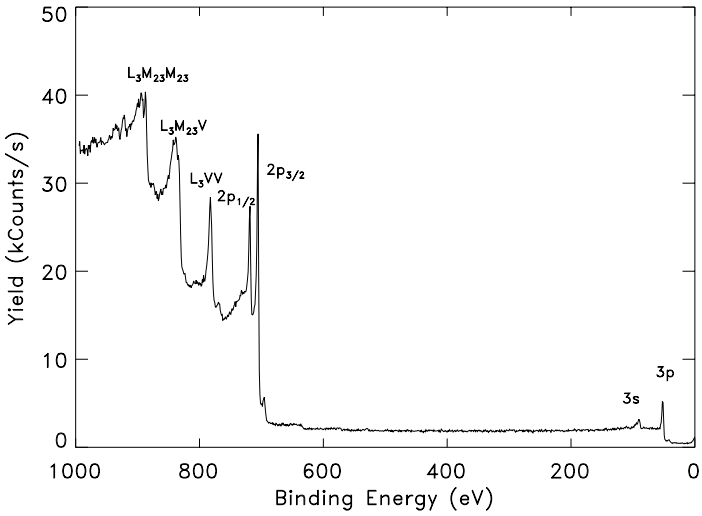

FIGURE 2.9: The measured XPS spectrum of Fe

2.7 X-ray Photoelectron Spectroscopy

X-ray photoelectron spectroscopy (XPS) is a surface analytical technique which has proved to be useful for the study of the initial oxidation of metals. The intensities and positions of photoelectron peaks contain information on overlayer thickness, chemical state of near-surface atoms and the stoichiometry of the overlayer.

The principle of XPS is simple: The sample is irradiated by photons from an X-ray source. In the sample, photoelectrons (and Auger electrons) are created. Photoelectrons created within a certain length from the sample surface (defined by the *Attenuation Length* AL) can reach the surface of the sample. An electron detector (usually a so-called hemispherical analyzer (HSA) operated in constant pass energy (E_{pass}) mode) is placed in front of the sample to detect the kinetic energy of the electrons leaving the sample. An example of the XPS spectrum of clean iron, measured with the experimental setup described below, is shown in figure 2.9.

2.7.1 Quantitative XPS

In qualitative XPS the composition of the sample under study is found by comparing the spectrum with reference spectra. The composition is deduced from the chemical shift or the peak shapes of the measured spectrum. The chemical shift is the change of binding energy of core photoelectrons caused by a change in the chemical environment of the atom emitting the photoelectron. The changes in peak shape due to different compositions are, for instance, noticeable by multiplet splitting and the occurrence of shake-up satellites. This qualitative method is useful if large differences are expected between the various compositions. The differences between the spectra of the different iron oxides and hydroxide, however, are small. Therefore, quantitative XPS has to be done to obtain accurate results.

In quantitative XPS, the intensities of the different peaks are used to obtain the composition of the sample. Usually, quantification methods involve correction for the spectrometer work function and transmission function (described in sections 2.7.2 and 2.7.3), followed by the subtraction of the background due to inelastically scattered electrons. In this work, the formalism of Tougaard *et al* [27,28] is used for the calculation of the backgrounds. The basic expressions for the quantification of XPS results are given in appendix A.

Based on the Tougaard formalism, a method has been developed by Graat *et al* [29–31] to reconstruct the measured spectrum from reference spectra of Fe, FeO and Fe_2O_3, measured in the same instrument. In this way the use of sensitivity factors, which can differ from instrument to instrument, is avoided. Also the fitting of several more or less arbitrary Gaussian or Lorentzian functions to a residual spectrum is avoided. This fitting procedure is also described in appendix A.

2.7.2 Spectrometer Work Function

The binding energy E_B of the photoelectrons is calculated from the measured kinetic energy $E_{K(\mathrm{meas})}$ with the following equation [32]:

$$E_{K(\mathrm{meas})} = E_{\mathrm{X-ray}} - E_B - W \tag{2.14}$$

where W is the spectrometer work function.

To obtain values for W and thus calibrate the energy scale of the spectrometer, a standard method proposed by the American Society of Testing

and Materials was used [33]. This method consists of measuring the kinetic energy of peaks with (very) different energies and determining the shift (value of W) found between the measured peak and the reference values for the kinetic energy. We used a Cu reference sample, and measured the energies of the Cu($2p_{3/2}$) and Cu(3p) photoelectron and the Cu($L_3M_{45}M_{45}$) Auger electron peaks. The measured kinetic energies were compared with reference data obtained by Powell [34] and Briggs and Seah [35].

We measured the kinetic energies of the Cu peaks with both Mg K_α and Al K_α radiation at E_{pass}=20 eV, and found that the work function depends slightly on energy. This energy dependence of W is caused by alinearity in the spectrometer electronics system and is described with a linear relation between W and the measured kinetic energy $E_{K(\text{meas})}$. The results of a fit to the data are:

$$W = (4.94 \pm 0.02)\,\text{eV} + (3.84 \pm 0.18) \times 10^{-4} \times E_{K(\text{meas})} \tag{2.15}$$

with $E_{K(\text{meas})}$ and W in eV.

2.7.3 Spectrometer Transmission Function

After correcting for the spectrometer work function W, the measured spectra have to be corrected for the so-called spectrometer transmission function, before the intensities of different peaks can be compared. The sensitivity of the spectrometer depends on the kinetic energy of the electrons. This energy dependence is different for different spectrometer designs and operation modes and is expressed in the transmission function T. To obtain reliable values, this transmission function has to be measured for the complete detection setup, including additional transfer lenses.

The transmission function T is defined as the ratio between the measured energy distribution of the photoelectrons and the energy distribution of the photoelectrons emerging from the sample. If we denote these by $n'(E_K)$ and $n(E_K)$, respectively, T is given by:

$$n'(E_K) \equiv T(E_K)n(E_K) \tag{2.16}$$

For an ideal and simple Hemispherical Sector Analyzer without additional lenses $T(E_K)$ is expected to vary with $E_K^{-0.5}$ [36].

We determined the analyzer transmission function by comparing the spectrum of Cu with the true emission spectrum of Cu, as measured by

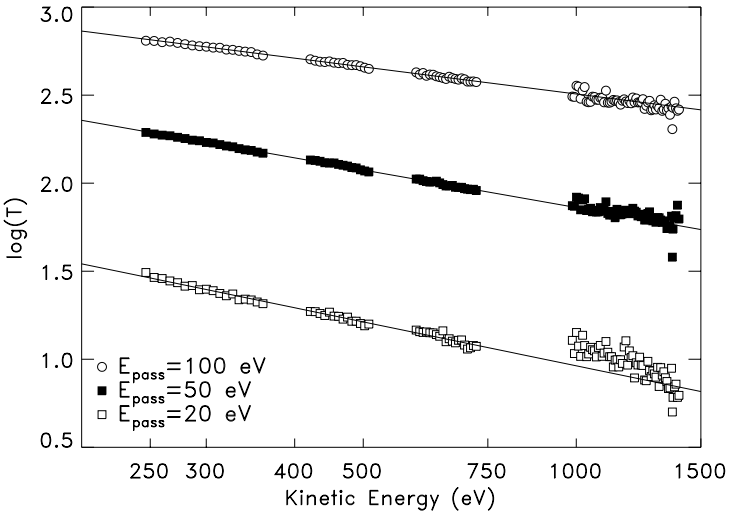

FIGURE 2.10: The transmission function of the CLAM-2 analyzer as measured with the Al K_α X-ray source with E_{pass}=100, 50 and 20 eV. The straight lines shown are linear least squares fits to the data over the energy range 250-800 eV.

Seah and Smith [37]. The spectrum of Cu was measured for E_{pass}=100, 50 and 20 eV using the Al K_α X-ray source. The resulting transmission function is shown in figure 2.10. The values thus obtained were fitted to a linear function on the log-log scale, obtaining $T \propto E_K^{-\alpha}$. The resulting values for α are shown in table 2.1.

2.7.4 Reference Samples

For the reconstruction of the Fe(2p) spectrum (see appendix A), reference spectra of bulk iron oxides of well known composition and Fe oxidation state are needed.

A FeO reference sample was prepared by oxidizing a Fe(100) sample at 573K, followed by mild sputtering in Argon (10 minutes, 800 V, P_{Ar}=3×10^{-5} mbar, target current I_t=4 μA) to reduce Fe^{3+} to Fe^{2+} [38]. A Fe_2O_3 reference powder sample was obtained by hydrolysis of a 0.1 M $Fe(NO_3)_3$ solution with 0.1 M NH_4OH at a temperature of 298K. At pH

E_{pass} (eV)	α
100	0.511 ± 0.004
50	0.709 ± 0.004
20	0.829 ± 0.013

TABLE 2.1: The exponent α in the transmission function $T(E_K) \propto E_K^{-\alpha}$ for the pass energies 100, 50 and 20 eV.

values between 5 and 7 FeO(OH) was formed which was cleaned in distilled water and dried at a temperature of 378K. To form bulk Fe_2O_3 the powder was heated to 673K for 48 hours in air. The thermodynamically stable Fe_2O_3 was then formed via the reaction 2FeO(OH)→ α-Fe_2O_3 + H_2O [3,38].

The measured Fe(2p) spectra of the Fe_2O_3, FeO and clean Fe reference samples are shown in figure 2.11. After Tougaard background subtraction, O(1s) and Fe(2p) peak intensity ratios were calculated. The ratio of the O(1s) peak intensities ($Y_{\text{O1s}}^{\text{FeO}}/Y_{\text{O1s}}^{\text{Fe}_2\text{O}_3}$) for bulk samples was found to be 0.8, which appears to be equal to the ratio of the oxygen atomic densities of FeO and Fe_2O_3. The ratio of the Fe(2p) intensities of the FeO and Fe_2O_3 samples amounted to 1.1, which equals the ratio of Fe atomic densities. The measured ratios are expected if the ALs in FeO and Fe_2O_3 are equal (ignoring matrix and composition effects [36]). In the case of the iron oxides, the atomic densities and mass densities of FeO, Fe_3O_4, and Fe_2O_3 are similar. Therefore, the AL values in the oxides are expected to be roughly the same and the ratio of peak intensities is approximated by the ratio of atomic densities according to equation (A.2).

The observed values for the binding energies are in good agreement with literature values [30,39–41] and also the typical satellite peaks for FeO and Fe_2O_3 are observed (indicated in figure 2.11). According to work by Bagus and Bauschlicher [42], the O(1s) binding energy changes approximately linearly as a function of the anionic charge. From the oxygen anionic charge and the (assumed) stoichiometry of the reference sample, the average charge on the iron cation could then be calculated. In figure 2.12, the Fe(2p), Fe(3s) and Fe(3p) binding energies, measured with XPS, are plotted as a function of this calculated Fe cation charge, together with linear fits to the data. The linear fits describe the data very well. The Fe(2p) and Fe(3p)

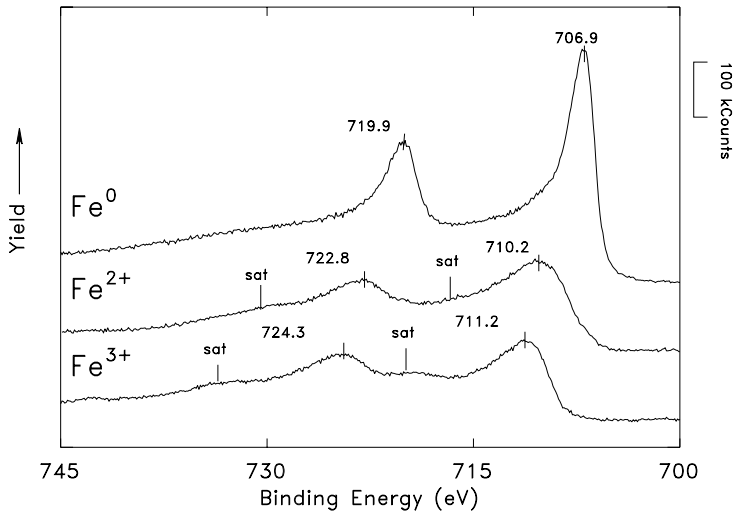

FIGURE 2.11: XPS reference spectra of clean iron (Fe^0), bulk FeO (Fe^{2+}), and bulk Fe_2O_3 (Fe^{3+}). Peak maxima and typical satellite peaks are indicated.

binding energy values for FeO seem to be slightly higher than expected. This might indicate the presence of a small amount of Fe^{3+} in the FeO reference sample, which would lead to an overestimation of the amount of Fe^{2+} by the reconstruction of spectra. A detailed calculation has to be done, however, to replace the linear approximation by a more accurate theoretical curve, before one can draw conclusions from the small deviations observed for the FeO reference sample.

A FeO(OH) sample measured showed a Fe(2p) spectrum in agreement with literature and a O(1s) spectrum containing the typical OH^- shoulder at 532 eV. The Fe(2p) and O(1s) yields of this sample are in agreement with the yields obtained from the FeO and Fe_2O_3 reference samples. So, ignoring effects of surface roughness and using Tougaard background subtraction methods, one can use the traditional relations for quantitative XPS [36] for the reference samples.

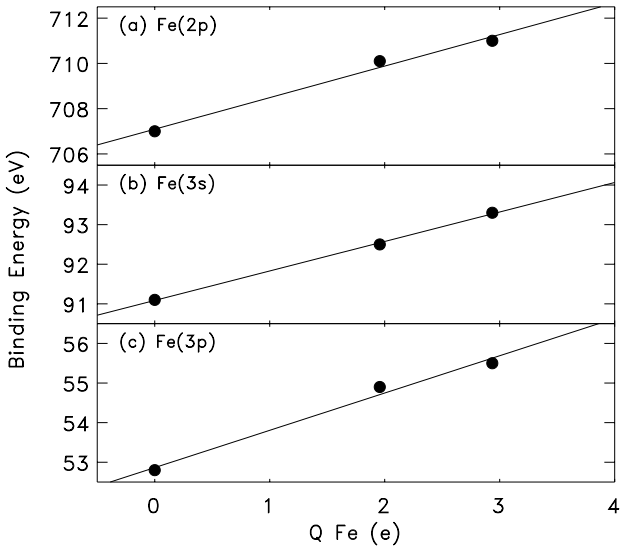

FIGURE 2.12: Fe(2p), Fe(3p) and Fe(3s) binding energies of clean iron (Fe^0), bulk FeO (Fe^{2+}), and bulk Fe_2O_3 (Fe^{3+}) (measured with XPS) vs. Fe cation charge. The solid lines are linear fits to the data.

2.7.5 Experimental Setup

XPS was done using a CLAM-2 Hemispherical Sector Analyzer with a mean radius of 100 mm and a Vacuum Generators XR2E2 Twin Anode X-ray Source with the standard Al/Mg anodes. Spectra were recorded using the Al-K_α source operated at a power of 120 W. The most used values for the pass energy (E_{pass}) for the analyzer, governing both resolution and count rate, were 100, 50 and 20 eV. Quantitative XPS (see sections A.1 and A.2) was always done with a pass energy of 20 eV and the Al-K_α source. The energy resolution then amounted to 1.44 eV FWHM (measured on the Cu(2p3/2) peak). To reduce the influence of magnetic fields on low-energy electrons the vacuum chamber consists of mu-metal. The angle θ between the sample normal and the analyzer amounted to 15° and the angle β between the direction of detection and the X-ray source was 33.5°. The plane acceptance angle α_{XPS} of the analyzer amounted to 13°. Angular resolved XPS was done by rotating the sample around an axis parallel to the detector/X-ray source plane (β remained constant while θ was varied).

Chapter 3

Determination of Photoelectron Attenuation Lengths in Thin Oxide Films on Iron surfaces

3.1 Introduction

X-ray photoelectron spectroscopy (XPS) is a surface analytical technique which has proved to be useful for the study of the initial oxidation of metals. The intensities and positions of photoelectron peaks contain information on overlayer thickness, chemical state of near-surface atoms and the stoichiometry of the overlayer.

A number of articles has been published about XPS studies of the oxidation of iron in O_2, H_2O and O_2/H_2O mixtures [29,30,39,40,43–48]. In most of the reports [39,40,43–46] merely peak shapes and positions are considered. To obtain the intensities of Fe(2p) photoelectron peaks a background has to be subtracted from the spectrum. Usually the background is a linear or Shirley type [47,48]. Following background subtraction, Gaussian or Lorentzian functions, representing Fe^0, Fe^{2+} and Fe^{3+} contributions, are fitted to the resulting spectrum. From the peak intensities, layer thicknesses are calculated. Sometimes, sensitivity factors are used to calculate stoichiometries from peak intensities.

However, the errors introduced by incorrect background subtraction, the use of sensitivity factors and fitting can amount to about 30% [36]. The most correct way to analyze the spectra seems to be to use the formalism of Tougaard to subtract backgrounds, and to relate the intensities of the

resulting spectrum to those of reference spectra of bulk samples measured with the same instrument, under the same conditions. Tougaard has developed a general formalism to subtract backgrounds from XPS spectra in a physically meaningful way [27,28]. Based on this formalism, expressions were derived by Hansen and Tougaard [49] for the background function in case the depth profile of the different atoms in the analyzed part of the sample is known (see appendix A.3). Based on these expressions, a method has been developed by Graat *et al* [29–31] to reconstruct the measured spectrum from reference spectra of Fe, FeO and Fe_2O_3, measured in the same instrument (see appendix A.4). In this way the use of sensitivity factors, which can differ from instrument to instrument, is avoided. Also the fitting of several more or less arbitrary Gaussian or Lorentzian functions to a residual spectrum is avoided.

Yet, layer thicknesses can be expressed only in d_{ovl}/λ, where λ is either the Inelastic Mean Free Path (IMFP) of photoelectrons (if the effect of elastic scattering is ignored [50–52]) or the Attenuation Length (AL), and d refers to the thickness of the overlayer. Even in situations where the effect of elastic scattering is small, it is not clear whether one should use a "universal curve", *i.e.* a frequently used empirical relation for the IMFP [53], or a modified Bethe equation (by Tanuma *et al* [54–56]). In order to eliminate the error introduced by ignoring elastic scattering effects, Cumpson and Seah [57] have proposed to use the AL in an exponential description of the Depth Distribution Function (DDF), rather than the IMFP.

The aim of the present work is to investigate the validity of an exponential DDF for the XPS investigation of the initial oxidation of iron and to obtain values for the AL. The formalism of Hansen and Tougaard implies the use of an exponential DDF for the calculation of the backgrounds. If this is correct, the yields obtained as a function of oxide layer thickness should be described by an exponential DDF.

We present the results of XPS and *in-situ* Elastic Recoil Detection (ERD) measurements on thin iron oxide layers on single crystal iron substrates. The oxide layers are obtained by oxidizing Fe(100) and Fe(110) oriented substrates at room temperature (RT) and 473K in O_2, yielding oxide layers in a thickness range between 0 and 10 nm. At these temperatures the oxide layers grown are planar [6]. The Fe(2p) spectrum of iron covered with a thin oxide layer is too complicated to be analyzed with simple quantification methods (*e.g.* Gaussian peak fitting combined with

subtraction of a linear background). Instead, we use the formalism given in appendix A for the subtraction of the background arising from inelastically scattered electrons and to separate the contributions from the oxide and the substrate in the Fe(2p) spectrum. XPS Peak intensities are then compared to intensities of Fe, FeO and Fe_2O_3 reference spectra. Further, using *in-situ* ERD [22], the quantity of oxygen in the oxide layers is determined accurately in atoms/cm^2. Finally, by comparing these oxygen areal densities with the XPS peak intensities, the validity of an exponential DDF for the analysis of overlayer experiments is checked for this system and a value for the AL is obtained in atoms/cm^2.

To our knowledge, this is the first measurement of the AL of the O(1s) and Fe(2p) XPS peaks at kinetic energies of E_K=957 eV and E_K=776 eV, respectively, from iron oxide overlayers, using an accurate and quantitative technique. Using these AL values, overlayer thicknesses can be calculated directly from XPS yields.

3.2 Results

3.2.1 Stoichiometry

For a constant stoichiometry Fe_xO, and applying an exponential DDF, there should be an approximately linear relation between the O(1s) intensity Y_{O1s} and the intensity of the oxide part of the Fe(2p) spectrum Y_{ox} according to:

$$\frac{Y_{\mathrm{ox}}}{Y_{\mathrm{O1s}}} = x \cdot \left(\frac{1 - \exp[-d_{\mathrm{ovl}}/(\lambda_{\mathrm{Fe2p}} \cos\theta)]}{1 - \exp[-d_{\mathrm{ovl}}/(\lambda_{\mathrm{O1s}} \cos\theta)]} \right) \cdot \frac{Y_{\mathrm{ox}}^{\infty}}{Y_{\mathrm{O1s}}^{\infty}} \tag{3.1}$$

where Y_{ox}^{∞} and $Y_{\mathrm{O1s}}^{\infty}$ are the respective Fe(2p) and O(1s) intensities of a bulk FeO reference sample ($x = 1$). This relation holds if matrix effects are ignored [35] ($\lambda_{\mathrm{FeO}} \approx \lambda_{\mathrm{Fe_2O_3}}$, see appendix A.2). In figure 3.1, experimental values of Y_{ox} and Y_{O1s}, obtained at various overlayer thicknesses are plotted against each other. Lines are drawn in the figure representing the theoretical relation between Y_{ox} and Y_{O1s} according to equation (3.1). The Y_{ox} and Y_{O1s} values are the numerator and denominator of equation (3.1), respectively, with d_{ovl} running from zero to infinity. The lines are plotted for different values of x, corresponding to FeO, Fe_2O_3 and $Fe_{0.9}O$. To calculate the curves drawn in figure 3.1 we took the values obtained in section 3.2.2 of this thesis for λ_{O1s} and λ_{Fe2p}. It should be noted that only the ratio of

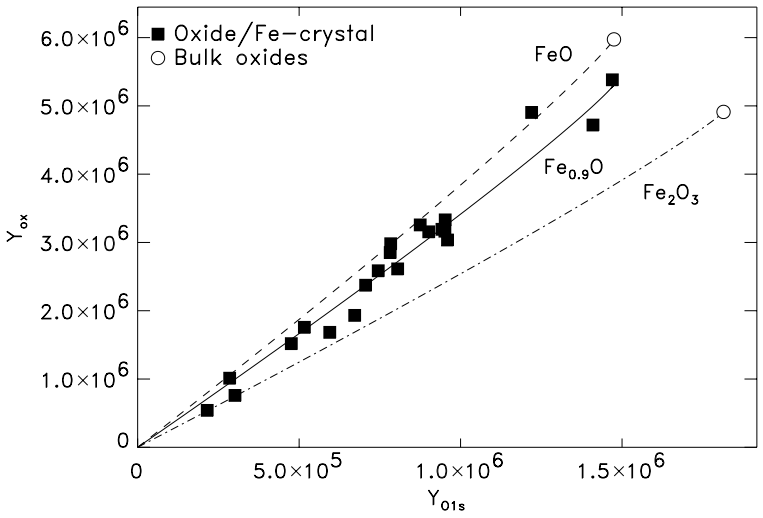

FIGURE 3.1: Oxide yield of the Fe(2p) spectrum vs. O(1s) yield. Solid line: fit to equation (3.1), yielding $Fe_{0.9}O$. Dashed and dash-dotted lines: curves for FeO and Fe_2O_3, respectively. Squares: measurement. Circles: measured data from FeO and Fe_2O_3 reference samples.

λ_{Fe2p} and λ_{O1s} influences the curvature of the lines, because it is the value of $d_{\mathrm{ovl}}/\lambda_{\mathrm{Fe2p}}$ which determines the value of Y_{Fe2p} on the y-axis of figure 3.1 while the value of $d_{\mathrm{ovl}}/\lambda_{\mathrm{O1s}}$ determines the value of Y_{O1s} on the x-axis. The ratio of our values of λ is in agreement with values of λ given by Seah and Dench [53].

A best fit to the overlayer data points yields $x = 0.90 \pm 0.05$. This value for x is in good correspondence with the quantitative results obtained with ion beam analysis published by Leibbrandt *et al* [6,58] and with the positions of the peak maxima reported in this work.

3.2.2 Determination of Attenuation Lengths

To determine the AL values of photoelectrons in the $Fe_{0.9}O$ overlayer, oxide layers of various thicknesses were grown and the oxygen areal densities were measured with ERD [22]. In figures 3.2 and 3.3 the relative Fe(2p) substrate intensity, the oxide yield of the Fe(2p) region, and the O(1s) yield are plot-

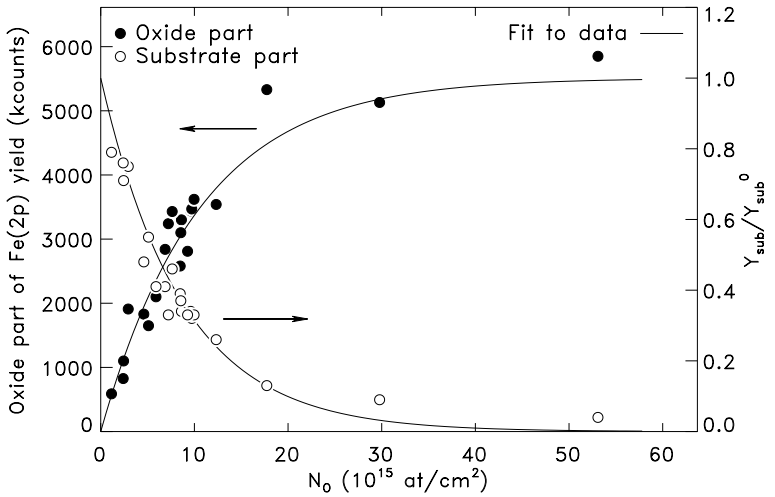

FIGURE 3.2: Fe(2p) XPS yields vs. oxygen coverage. Filled circles: oxide part. Open circles: Substrate part. Solid lines: fits to equations (A.3) and (A.5).

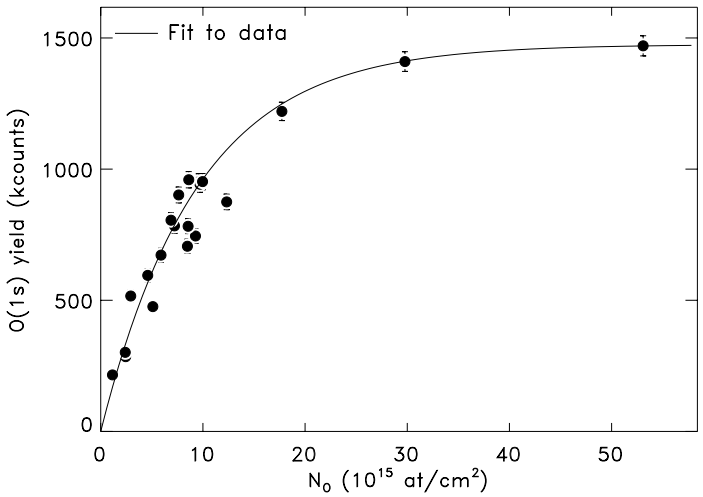

FIGURE 3.3: O(1s) XPS yields vs. oxygen coverage. Squares: measurement. Solid line: fit to equation (A.6).

ted against the oxygen coverage determined with the combined ellipsometry and ERD results. The solid lines in the figures are fits to equations (A.3), (A.5) and (A.6). The good agreement between the exponential functions and the data indicates that the use of an exponential DDF, for both the calculation of the background and the description of XPS yields as a function of oxygen coverage, is valid. For an electron kinetic energy of 776 eV (Fe(2p)) an AL corresponding to $(9.3\pm0.5)\times10^{15}$ O atoms/cm^2 (or $Fe_{0.9}O$ molecules/cm^2) is found. For a kinetic energy of 957 eV (O(1s)) an AL corresponding to $\lambda=(9.9\pm0.5)\times10^{15}$ O atoms/cm^2 ($Fe_{0.9}O$ molecules/cm^2) is found.

The second fit parameter in equations (A.5) and (A.6) for Y_{ox} and Y_{O1s} is the value for Y_{ox}^{∞} or Y_{O1s}^{∞}, respectively. The value of Y_{ox}^{∞} is slightly lower than that of the bulk FeO reference sample, while the value for Y_{O1s}^{∞} is – within the error – equal to the reference value. This implies that the oxygen density in the oxide is equal to that of the FeO reference value, which we assume to be equal to the literature value (4.75×10^{22} O atoms/cm^3). This is in agreement with results for bulk substoichiometric wüstite ($Fe_{1-x}O$) [3].

3.3 Discussion

Figure 3.4 shows the kinetic energy dependence of our values for λ (open circles), together with results of Leibbrandt *et al* [5], who determined the value of the AL in $Fe_{0.9}O$ from the evolution of the 63 eV NVV and 237 eV NNV Auger signals of Pt buried under the oxide. Leibbrandt applied Nuclear Reaction Analysis (NRA) to determine absolute oxygen coverages in atoms/cm^2, so the results are directly comparable. From the oxygen density of bulk FeO (4.75×10^{22} O atoms/cm^3 [3]) we calculate λ_{O1s}=7.6 monolayers and λ_{Fe2p}=7.1 monolayers. These can be compared to the empirical IMFP formula of Seah and Dench [53] (shown as a solid line in figure 3.4):

$$\lambda_i = 2170/E_K^2 + 0.72(aE_K)^{1/2} \text{ monolayers} \tag{3.2}$$

where a is the lattice constant of the solid in nm and E_K the kinetic energy of the electron in eV. For $E_K > 200$ eV, our values and those of Leibbrandt are 10% lower than predicted by the universal curve of Seah and Dench. A two-parameter fit to the formula of Seah and Dench, shown in figure 3.4, gave $\lambda = 8000/E^2 + 0.67(aE)^{1/2}$ monolayers. The IMFP formula of Seah and Dench was obtained by comparison with experimental data from over-

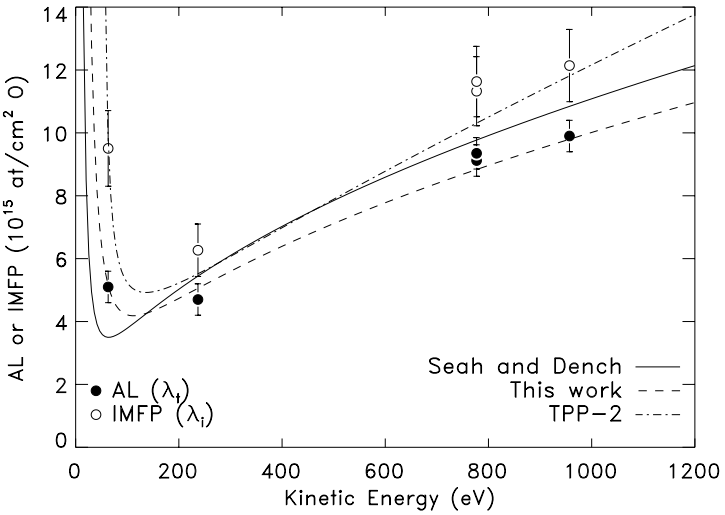

FIGURE 3.4: AL from this work and from Leibbrandt [5] as a function of kinetic energy E_K. Filled circles: AL values. Open circles: IMFP values (see text). Solid line: formula of Seah and Dench for inorganic compounds. Dashed line: Modified formula of Seah and Dench. Dash-dotted line: Modified Bethe equation of Tanuma *et al* for the IMFP.

layer experiments, so equation (3.2) should in fact be used for values of the AL and not for the IMFP.

The value of the AL is determined by the IMFP and the effect of elastic scattering, usually expressed as λ_{tr}, the transport mean free path.

Tilinin *et al* [59–62] have calculated both the differential and total cross-section for the elastic scattering process by means of a simple Thomas-Fermi potential and a quasi-classical approximation. They found that the reduced cross-section $\sigma_{\mathrm{tr}}/\pi r^2$ (where r is the Thomas-Fermi screening radius $0.885 r_0 Z^{-1/3}$) is a universal function of the reduced energy $\epsilon = E_K r/e^2 Z$, and obtained good agreement with experimental data. Using this universal function, we obtain, at a kinetic energy of $E_K = 957$ eV, $\sigma_{\mathrm{tr}} = 8.4{\times}10^{-18}$ cm^2 for oxygen atoms and $\sigma_{\mathrm{tr}} = 3.0{\times}10^{-17}$ cm^2 for iron atoms. For $Fe_{0.9}O$, this would lead to a value for the transport mean free path of $\lambda_{\mathrm{tr}} = 2.8{\times}10^{16}$ O/cm^2. In the same way, λ_{tr} could be calculated for the other data points. The results are given in table 3.1.

Photoelectron line	E_K (eV)	λ_t (10^{15} O/cm^2)	λ_{tr} (10^{15} O/cm^2)	λ_i (10^{15} O/cm^2)
Pt NNV	63	5.1±0.5	2.1±0.2	9.5±0.8
Pt NVV	237	4.7±0.5	5.7±0.5	6.3±0.5
Fe(2p)	777	9.12±0.5	21.4±1.7	11.3±1.0
	777	9.35±0.5	21.4±1.7	11.6±1.0
O(1s)	957	9.9±0.5	28±2	12.2±1.1

TABLE 3.1: The values of the measured AL (λ_t), the theoretical transport mean free path (λ_{tr}) and the calculated inelastic mean free path (λ_i) shown in figure 3.4.

From the values for λ_{tr}, we calculate the IMFP λ_i, using a correction formula by Jablonski and Tougaard, which can be applied if the geometry is close to normal emission and the detection angle is close to the magic angle (54^o) [63]:

$$\lambda_t = \frac{\lambda_i \lambda_{tr}}{\lambda_{tr} + a_1(\lambda_{tr} + \lambda_i)} \tag{3.3}$$

where $a_1 = 0.157764$ is a constant arising from a fit of the correction formula to Monte Carlo simulations of the DDF and λ_t is the resulting AL. The calculated values for λ_i, given our values for the AL and λ_{tr} as above, are given in table 3.1 and plotted in figure 3.4. The values for the AL are about 17% lower than the values for the IMFP, which is in agreement with observations by Cumpson *et al* [57].

Tanuma *et al* [56] proposed a modified Bethe equation (TPP-2) for the IMFP of inorganic compounds. We fitted our IMFP data to this modified Bethe equation, which is given (in Ångströms) by:

$$\lambda_i = E/\{E_p^2[\beta \ln(\gamma E) - (C/E) + (D/E^2)]\} \tag{3.4}$$

Here, $E_p^2 = 829 N_V \rho / M$ (eV^2), where N_V is the number of valence electrons per molecule, M is the molar mass (g/mol) and ρ is the mass density in g/cm^2. Expressions for the parameters β, γ, C and D are given in [56]. For the calculation we took the values for FeO (band gap energy E_g=2.3 eV [64], needed for the calculation of β, ρ=5.7 g/cm^3, M=72, N_V=10). The value for γ given by Tanuma's equation amounted to 0.08 eV^{-1}. Only this value was varied until a best fit was obtained for γ=2.14×10^{-2} eV^{-1} (shown in figure 3.4). There is good agreement between data and fit.

In summary, by subtracting the background as described by the formalism of Hansen and Tougaard and making use of reference spectra of clean iron, FeO and Fe_2O_3, we obtain meaningful results employing quantitative XPS. From the relation between the yield of the oxide part of the Fe(2p) spectrum and the O(1s) yield, we determined the stoichiometry of the oxide layer to be $Fe_{0.9}O$. By combining the XPS intensities with oxygen coverage data obtained with ERD and ellipsometry, we were able to determine a value for the AL at E_K=776 eV (Fe(2p)) as well as one for E_K=957 eV (O(1s)) in atoms/cm^2.

The used method to calculate backgrounds implies an exponential DDF. Our data could be well described by equations (A.3), (A.5) and (A.6), which means that the use of an exponential DDF is internally consistent and may indeed be used for this system. Furthermore, values of the AL have been obtained which are essential for the interpretation of XPS spectra.

3.4 Conclusions

Applying the Tougaard background subtraction formalism and using reference samples instead of using sensitivity factors, quantitative XPS in the way described by Briggs and Seah [35], with an exponential DDF, can be done for $Fe_{0.9}O$ films on iron. The AL values needed in this formalism are measured employing ERD, ellipsometry and XPS. These values are λ_t=9.3×10^{15} $Fe_{0.9}O$ molecules/cm^2 for E_K=776 eV (Fe(2p) region) and λ_t=9.9×10^{15} $Fe_{0.9}O$ molecules/cm^2 for E_K=957 eV (O(1s) region), which are about 10% smaller than the IMFP calculated with the empirical formula of Seah and Dench for inorganic compounds.

Comparison of IMFP values calculated from the data, using theoretical values for λ_{tr}, with Tanuma's TPP-2 formula showed good agreement (after a slight change of the parameter γ).

Chapter 4

The Iron Oxide Layer Grown in O_2

4.1 Introduction

Despite decades of research on the oxidation of Fe(100) [6,40,65–71] little is known about the (electronic) structure of the oxide layer grown upon exposure to O_2 gas and its influence on the oxidation kinetics. This is mainly due to the fact that most studies focus on the growth of the first monolayer of oxide in the low pressure regime (10^{-10}-10^{-8} mbar), while little attention is paid to the (electronic) structure, optical properties, stoichiometry, oxidation state or oxidation kinetics of the oxide formed upon further exposure.

In some earlier studies, a multi-technique approach has proved to be successful. Leibbrandt *et al* [6] showed that the oxide growth (after 1 ML) at temperatures between 423K and 623K could be described consistently with the oxidation model of Fromhold and Cook [1,72,73] (see section 5.4 for a brief description of this model): at these temperatures a homogeneous and planar FeO layer forms, Fe cations are the moving species during oxide growth and the oxidation rate is limited by the thermionic emission of electrons from the Fermi level of Fe into the conduction band of the growing oxide.

The aim of the present work is twofold: First, we report the optical properties, the Fe oxidation state in the oxide and the temperature dependence of this oxidation state, by a careful analysis of results obtained with a combination of ERD, ellipsometry and XPS. Second, we describe experiments to determine the moving species during the oxidation of Fe(100) at room temperature.

These results enable us to interpret the results on the oxidation kinetics within the framework of the Fromhold-Cook model, as will be done in chapter 5.

4.2 The Oxidation State of Fe in the Oxide Layer

Attempts to determine the oxide formed from the Fe MNN Auger peak have been made, but at room temperature for instance, FeO [68] as well as Fe_2O_3 and Fe_3O_4 [67] have been reported. Recently, Sault [45] showed that the Fe(MNN) line-shapes cannot be used to discriminate between Fe_2O_3 and Fe_3O_4. Other techniques used are Electron Energy Loss Spectroscopy (EELS), work function measurements, spin polarized electron spectroscopy and High Energy Ion Scattering with Shadowing and Blocking (HEIS-SB). With most of these techniques the determination of the oxide stoichiometry or Fe oxidation state means qualitative interpretation of spectra and consequently most authors report that the formation of a particular iron oxide is *suggested*. In contrast, HEIS-SB [6] is a quantitative technique which yields among others the overall stoichiometry of thin iron oxide layers. With this technique Leibbrandt *et al* [6] determined the stoichiometry of thin oxide layers formed by oxidation in O_2 of Fe(100) to be Fe_xO (with $x = 0.95$) at room temperature and 473K. Using XPS, we have determined the (overall) stoichiometry of thin layers grown in O_2 on Fe(100) to be Fe_xO with $x = 0.90 \pm 0.05$ (chapter 3).

To determine the oxidation state of iron in iron oxides, in principle X-ray Photoelectron Spectroscopy (XPS) is a powerful technique. Brundle *et al* [40] reported on the oxidation of Fe(100) in O_2 at room temperature. They found Fe^{3+} at high oxygen exposures and Fe^{2+} as well as Fe^{3+} at lower exposures. Again, these results are only qualitative. In the present work, we applied the method of Graat *et al* [31] to reconstruct the Fe(2p) spectra and accurately determined the fractions of Fe^{2+} and Fe^{3+}(see appendix A.4). The fitting parameters in this method are the overlayer thickness d_{ovl} (relative to the AL λ), and the fractions of Fe^{2+} and Fe^{3+} in the oxide layer, $C_{\mathrm{Fe^{2+}}}$ and $C_{\mathrm{Fe^{3+}}}$, respectively. We report on the oxidation state after different oxidation temperatures (300K to 473K) and at different oxide thicknesses *i.e.* after different exposures.

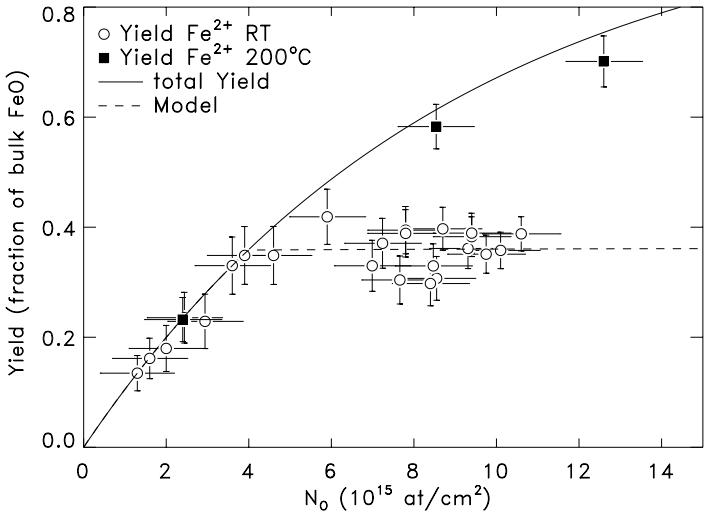

FIGURE 4.1: Normalized Fe^{2+} yield vs. oxygen coverage. The solid line indicates the yield if all the iron in the oxide layer is in the 2+ state. Open circles: RT measurement. The dashed line indicates the two-layer model mentioned in the discussion. Squares: 473K measurement.

4.2.1 The Initial Oxidation at Room Temperature

Results

Figure 4.1 shows the Fe^{2+} yield of the Fe(2p) spectrum as a function of oxide layer thickness for oxidation at RT and at 473K. This yield is normalized to the total Fe(2p) yield of the FeO reference sample (see chapter 3). The vertical error bars in the figure indicate the range within which the fitting parameter for the relative amount of Fe^{2+} could be varied without changing the quality of the fit. The solid line indicates the relation between oxygen coverage and Fe^{2+} yield if a pure FeO layer is formed, calculated using the AL and the yield of the FeO reference sample. For oxygen coverages up to 4.0×10^{15} atoms/cm^2 the layer formed consists of 100% Fe^{2+}, indicating the growth of FeO. For coverages larger than this value the Fe^{2+} yield of the RT oxidized samples does not continue to grow and significant amounts of Fe^{3+} are found. (For example $C_{Fe^{3+}}=0.45\pm0.06$ for $N_O=10\times10^{15}$ atoms/cm^2.)

Oxide layers prepared at different O_2 pressures (between 10^{-8} and 10^{-6}

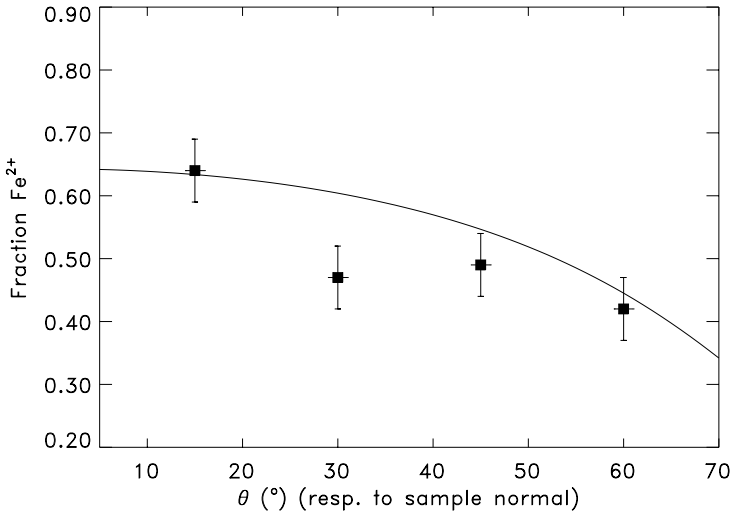

FIGURE 4.2: Relative amount of Fe^{2+} in the oxide layer vs. XPS detection angle. The oxygen coverage was 8.5×10^{15} atoms/cm^2, 65% Fe^{2+}. The solid line shows the expected behavior for a Fe^{2+} containing thin layer buried under a layer containing Fe^{3+}.

mbar), but with the same final oxygen coverage ($\sim8\times10^{15}$ atoms/cm^2), yielded the same XPS spectra. Apparently, in the considered range there is no pressure dependence in the ratio $C_{Fe^{2+}}/C_{Fe^{3+}}$.

To determine whether the Fe^{3+} is present near the oxide/substrate interface or in the top region of the oxide layer, angle-dependent XPS measurements were done on a layer grown at room temperature until near saturation (N_O=8.5×10^{15} O atoms/cm^2) in an oxygen pressure of 2×10^{-6} mbar. The spectra obtained at 15°, 30°, 45° and 60° were fitted with reference spectra obtained at the same angles. The values of d_{ovl} found in this way were consistent with each other.

In figure 4.2 the relative amount of Fe^{2+} fitted is plotted as a function of detection angle. For more grazing angles, the ratio $C_{Fe^{2+}}/C_{Fe^{3+}}$ fitted decreased, indicating that the Fe^{3+} is present mostly in the top part of the sample (at the oxide/oxygen interface during oxidation).

The Two-Layer System

In many previous studies of the initial oxidation and oxidation kinetics of Fe(100), the growth of a homogeneous layer was assumed, *i.e.* the authors assumed that there is no depth dependence of the oxide structure [10,67–71,74].

Our results, however, show that this is not the case: At RT, first an oxide layer consisting predominantly of Fe^{2+} grows (indicating the formation of FeO). When an oxygen coverage of 4.0×10^{15} O atoms/cm^2 is reached, a second layer starts to form, which contains Fe^{3+}, but possibly also Fe^{2+} and Fe^0. Results of variable angle XPS indicate that the Fe^{3+} is mainly present near the surface of the layer structure. This is consistent with the results of Leibbrandt *et al* [6], who **(a)** showed that iron is the moving species during the oxidation and the reaction takes place at the oxide/oxygen interface and **(b)** determined the Fe/O ratio to be 0.95 using HEIS-SB.

To determine the fraction of Fe^{2+} in the second layer, we fitted the results in figure 4.1 to a simple model. Assuming a two-layer system with a sharp interface, the expected Fe^{2+}yield as a function of oxygen coverage can be calculated. The Fe^{2+}/Fe^{3+} ratio was assumed to be constant in each sublayer. The best fit was obtained for the growth of $Fe_{0.77}O$ (*i.e.* with a Fe^{2+}/Fe^{3+} ratio of 0.67:1) on top of an FeO layer with an oxygen coverage of 4.0×10^{15} atoms/cm^2(dashed line in figure 4.1).

The formation of a double layer or a mixed oxide layer has been reported qualitatively several times over the past 20 years. Our quantitative analysis and model thus is in agreement with many previous results [6,40,65,68–70,75,76]. Sewell *et al* [65] report on a first layer of about 3 ML thickness (which corresponds to an oxygen coverage of 3.9×10^{15} atoms/cm^2). After this layer, they report the growth of a spinel structure, which is possibly γ-Fe_2O_3 or Fe_3O_4. The formation of FeO or a FeO-like oxide is also reported by Leibbrandt *et al* [6], Brucker *et al* [75] and – on polycrystalline iron – by Guo *et al* [76]. Brundle *et al* [40] present qualitative XPS results which are in agreement with the conclusions of this study (evidence of Fe^{3+} for exposures larger than 200 Langmuirs). Sinkovic *et al* [70] report an oxide containing a γ-Fe_2O_3-like oxide (magnetic structure and oxidation state are similar) as well as some Fe^{2+}, for exposures larger than 16 Langmuirs. The probe depth of their spin-resolved photo-emission technique is about 3 ML, so only the surface of the sample is probed, which is rich in Fe^{3+}. A similar result is obtained by Sakisaka *et al* [69], reporting γ-Fe_2O_3 after

20 Langmuirs with a similar probe depth. Both Sinkovic *et al* [70] and Sakisaka *et al* [69] report that they find a FeO-like oxide after annealing.

Although some of the above-mentioned authors assumed the formation of a homogeneous oxide layer, their experimental results are in agreement with the data presented here. The stoichiometry of the oxide layer obtained by fitting the coverage dependence of the Fe^{2+} yield in figure 4.1 ($Fe_{0.77}O$) seems to suggest the formation of Fe_3O_4. The combination of our results with the literature suggests, however, that the second layer consists of a mixture of a γ-Fe_2O_3-like phase and a Fe_xO-like phase. However, we cannot rule out the possibility that the oxide formed represents a unique phase with properties different from the known bulk oxides. Additional displaced Fe^0 is present.

4.2.2 Temperature Dependence of the Amount of Fe^{3+}

For layers thicker than 4.0×10^{15} O atoms/cm^2 there is a clear difference in the amount of Fe^{3+} present in the oxide layer between oxidation of Fe(100) at room temperature and 473K (circles and squares in figure 4.1, respectively). For layers grown at 473K, the relative amount of Fe^{3+} is at most $\sim$5%, consistent with the growth of an oxide layer with stoichiometry $Fe_{0.9}O$ for all thicknesses.

To measure the temperature dependence, oxide layers with a value of $\delta\Delta\simeq3.0^\circ$ were prepared at different temperatures between room temperature and 473K. The Fe(2p) and O(1s) spectra are plotted in figure 4.3. There are slight differences in the oxide layer thickness, which range from 8 to 9×10^{15} atoms/cm^2. As can already be seen from the spectra, the Fe^{2+} fraction increases with oxidation temperature. As a result of the quantitative analysis of the spectra, the fraction of Fe^{2+} versus the oxidation temperature is plotted in figure 4.5 (open circles), showing a gradual increase from 50% (room temperature) to 95% (473K). Figure 4.3 also shows the O(1s) spectra of these experiments. There are no large differences in the peak area for the different oxidation temperatures. The small differences can be due to both a different Fe/O ratio as well as to slight differences in the thickness of the oxide layer (as seen in the Fe(2p) spectrum and from the value of $\delta\Delta$).

In a separate experiment, an oxide layer with a thickness of $\delta\Delta=3.0^\circ$ was prepared at room temperature. After taking the Fe(2p) and O(1s) XPS spectra the sample was heated in vacuum during 15 minutes to 325K,

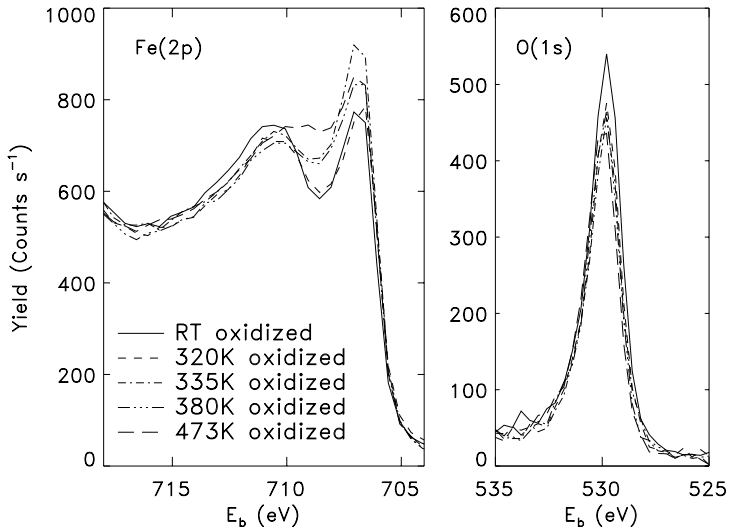

FIGURE 4.3: Fe(2p) and O(1s) measured spectra (not normalized) of Fe(100) oxidized to $\delta\Delta\simeq 3^\circ$ at different temperatures.

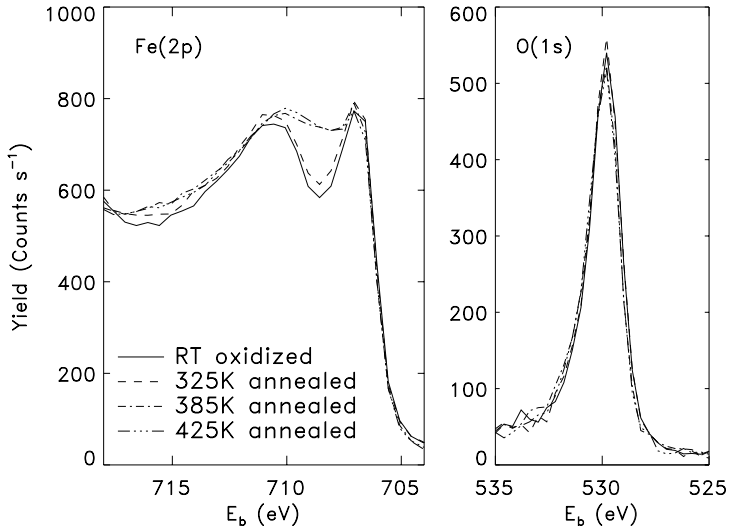

FIGURE 4.4: Fe(2p) and O(1s) measured spectra (not normalized) of Fe(100) oxidized to $\delta\Delta=3^\circ$ at room temperature and after subsequent annealing at different temperatures.

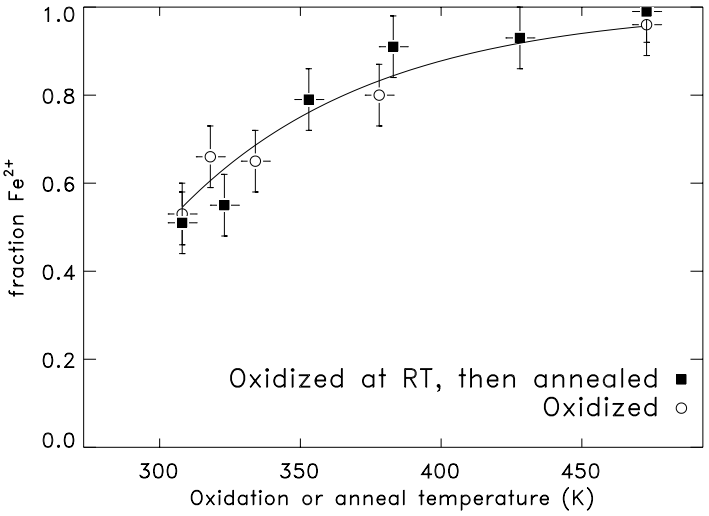

FIGURE 4.5: Relative amount of Fe^{2+} vs. oxidation or anneal temperature of Fe(100) oxidized to $\delta\Delta\simeq 3°$.

then to 380K and finally to 425K. The Fe(2p) and O(1s) spectra obtained (at room temperature) after each annealing period are shown in figure 4.4. From the raw data already a transition from an oxide layer containing a significant amount of Fe^{3+} to one containing mainly Fe^{2+} is visible. In the O(1s) spectrum no change is visible. The amount of Fe^{2+} fitted from the Fe(2p) spectrum after each heating cycle is also plotted in figure 4.5 (closed squares), again showing a gradual transition from an oxide layer with $C_{Fe^{2+}}=0.53\pm0.06$ present to one with $C_{Fe^{2+}}=0.93\pm0.06$.

For the oxide layer to remain charge neutral, the ratio of oxidized iron to oxygen in the layer must change during annealing. This means that either oxygen leaves the oxide layer, or there will be more oxidized iron in the oxide layer after annealing. The XPS results suggest that the amount of oxygen in the layer remains constant during the anneal. This was confirmed by two separate ERD measurements on Fe(100), oxidized to full saturation at RT, before and after 15 minutes annealing at $T = 475$K, as shown in figure 4.6. Indeed, the amount of oxygen in the oxide layer remained constant at $(9.0\pm0.3)\times10^{15}$ O atoms/cm^2. Consistent with this observation, the yield of oxidized iron (Fe^{2+} + Fe^{3+}) in the Fe(2p) part of the spectrum

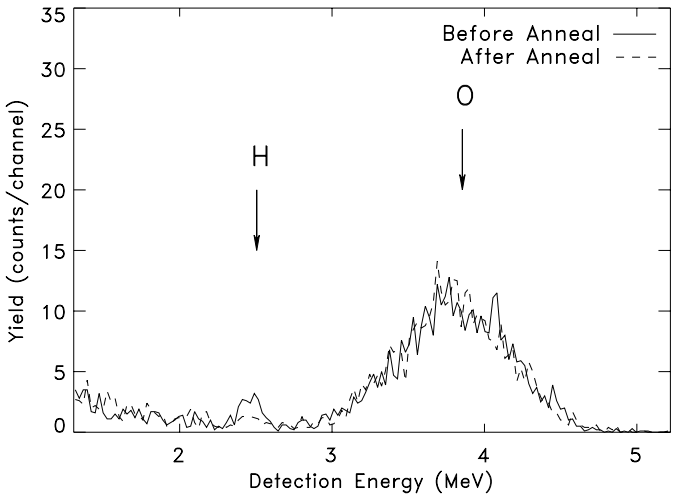

FIGURE 4.6: ERD spectra of Fe(100) oxidized to $\delta\Delta$=3.2, before and after a 475K anneal. The amount of oxygen in the sample does not change significantly ($9.0\pm0.3\times10^{15}$ atoms/cm^2).

increases with about 20%.

Using HEIS-SB we determined the amount of displaced iron atoms. The surface peak in the HEIS-SB spectrum (figure 4.7) is due to iron atoms which are not on substrate crystal lattice positions, and are therefore ascribed to Fe atoms in the oxide layer. The increase of the Fe surface peak as a result of RT oxidation corresponds to an increase of 8.8×10^{15} atoms/cm^2 of displaced iron. (The O/Fe ratio determined in this experiment is 1.0 ± 0.1.) This amount of displaced iron does not change upon annealing. This implies that part of the iron atoms, displaced during oxidation, must be in the Fe^0 state.

So, after oxidation at higher temperatures or after post-oxidation annealing of the sample in the range 320K-475K, the amount of Fe^{3+} is diminished: Almost all the Fe in the oxide layer is in the Fe^{2+} state.

The HEIS-SB results suggest that additional Fe^0 is displaced during the oxidation. This additional Fe^0 must be present in the first 30 nm of the sample. The assumption that the additional Fe^0 is distributed homogeneously over the oxide film does not give significantly different reconstructions of

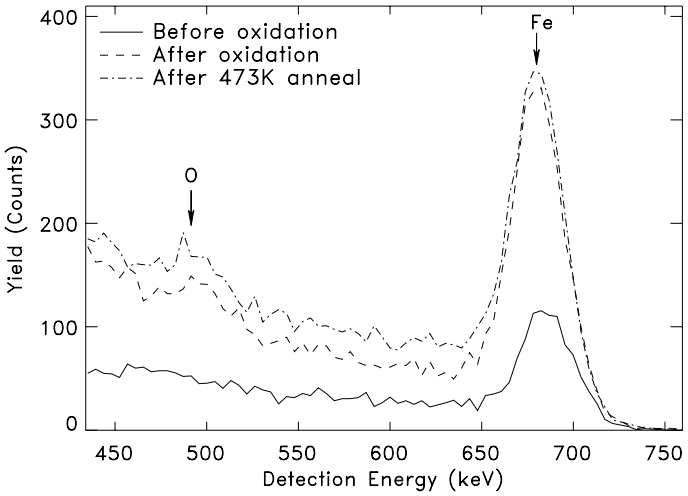

FIGURE 4.7: HEIS-SB spectra of Fe(100) oxidized to $\delta\Delta$=3.4, before and after a 475K anneal. The amount of displaced iron in the sample remains constant upon annealing (8.8×10^{15} atoms/cm^2).

the Fe(2p) spectra, so the actual Fe/O ratio in the oxide layer may be higher than determined with XPS. On the other hand, it is more likely that the displaced atoms in the Fe^0 state are present directly underneath the oxide film. However, such a distinction cannot be made with our present data. The increase of the Fe^{2+} yield during the anneal, combined with the constant HEIS-SB Fe yield, suggests that during the anneal, the additional Fe^0 is oxidized to Fe^{2+}.

4.3 The Optical Constant of the Overlayer

The dielectric constant of the oxide film (which is related to the optical constant via $\epsilon = N^2$) contains information about the response of the material to excess charge. This response changes the barrier for thermionic emission – as can be seen from equations (5.10) in section 5.4.1 – and thereby influences the thermionic emission rate of electrons into the conduction band of the oxide. Therefore, a change in the electronic structure of the oxide has a direct influence on the oxidation rate.

	overall	RT, $\delta\Delta$<1.0±0.3	RT, $\delta\Delta$>1.0±0.3
F_Δ (10^{-15} °cm^2/atom)	0.426±0.010	0.426	0.426
F_Ψ (10^{-19} °cm^2/atom)	-2±5	120±80	-130±60
n_1	2.67±0.02	2.4±0.3	2.9±0.3
k_1	0.82±0.02	0.6±0.2	1.0±0.2

TABLE 4.1: Experimental values for F_Δ and F_Ψ and the optical constants obtained in the flat layer model, assuming $\rho_O = 4.75\times10^{22}$ atoms/cm^3.

The response of the material to excess charge is of course determined by the number and arrangement of dipoles in the oxide and their strength. Therefore, a change of the optical constant of the oxide is always connected to a change in the oxide structure. This change of oxide structure may also affect other parameters important for the transport of charged species through the oxide layer (for example the barrier for diffusion of Fe cations W or the metal-oxide work function χ_0).

The oxidation kinetics of Fe(100) is discussed in chapter 5. The aim of this section is to obtain a value for the optical constant of the oxide film grown at room temperature in O_2 on Fe(100).

4.3.1 Results

Figure 2.4 **(b)** shows the parameter $\delta\Psi$ vs. oxygen coverage measured at several temperatures between RT and 475K. From the data, a value for F_Ψ was obtained (given in table 4.1). The symbols in figure 2.4 are measurements of $\delta\Psi = \Psi(0) - \Psi_{end}$ where Ψ_{end} is the value after oxidation. However, room temperature oxidation values of $\delta\Psi$ do not increase linearly with the oxygen coverage, as can be seen from the Ψ-Δ-plot given in figure 4.8. The figure shows a typical example of the change in Δ and Ψ during one oxidation experiment. The general trend is as follows: For $\delta\Delta < (1.0 \pm 0.3)$, Ψ and Δ decrease. For $\delta\Delta > (1.0 \pm 0.3)$, Ψ increases while Δ decreases further (negative value of F_Ψ). Straight lines were fitted to the data corresponding to $0 < \delta\Delta < 0.5$ and $1.5 < \delta\Delta < 3.5$, as shown for the measurement in figure 4.8. In this way, a value for $\delta\Delta$, at which the transition occurs, was determined. Assuming that the value of F_Δ remains constant, we could calculate a value for F_Ψ from the fitted linear relations between Δ and Ψ. These values of F_Ψ for $\delta\Delta$<1.0 and $\delta\Delta$>1.0 show a large

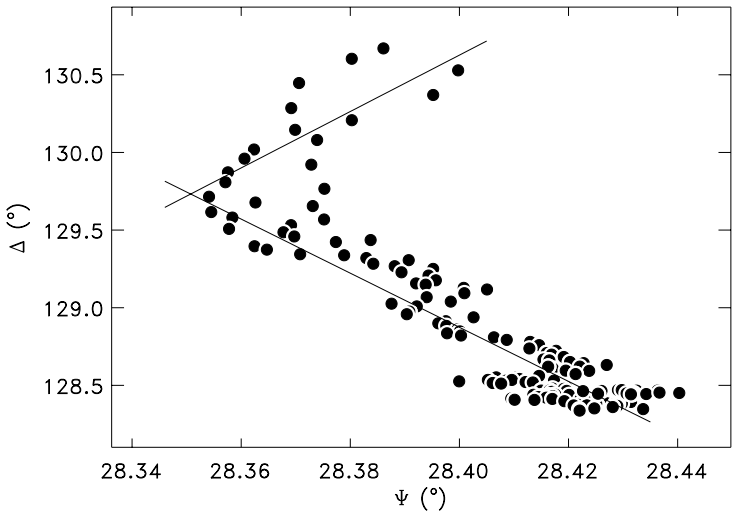

FIGURE 4.8: Δ vs. Ψ for the initial oxidation of Fe(100) at room temperature in 10^{-6} mbar O_2. The solid lines are linear least squares fits for the two regimes described in the text.

spread. The averages values are given in table 4.1. The value of $\delta\Delta$=1° corresponds to an oxygen coverage of $N_O = 3.9\times10^{15}$ atoms/cm^2.

4.3.2 Discussion

As shown in section 3.2.1, the oxygen density of bulk FeO (4.75×10^{22} atoms cm^{-3}) is a good estimation of the oxygen density in the layer grown. Assuming this density, we can calculate F_Δ and F_Ψ for different values of the real and imaginary part of the index of refraction n_1 and k_1 of the oxide layer (with $N_1 = n_1 + ik_1$, see section 2.5.1). For n_1=2.67±0.01 and k_1=0.82±0.01, the calculated values of F_Δ and F_Ψ are in agreement with the fits from figure 2.4. Figure 2.4 **(b)** also shows the curves for $\delta\Psi$ vs. N_O if literature values for the refractive index of bulk FeO, γ-Fe_2O_3, α-Fe_2O_3, and Fe_3O_4 are used [3]. These values are given in table 4.2. Because we found no values of k in the literature, we assumed that the imaginary part of the refractive index is zero.

Clearly, there is a large disagreement for F_Ψ, while the values for F_Δ

oxide	n_1	k_1	ρ_O 10^{22} at/cm^2	F_Δ 10^{-15} °cm^2/atom	F_Ψ 10^{-19} °cm^2/atom
FeO	2.32	?	4.75	0.48	244
α-Fe_2O_3	2.78	?	5.88	0.43	63.4
γ-Fe_2O_3	2.95	?	5.47	0.48	2.44
Fe_3O_4	2.42	?	5.37	0.44	189

TABLE 4.2: Literature values of the optical constants of bulk iron oxides [3,77]. Values for k are not present in the literature.

are within two standard deviations from the experimental value.

We fitted the RT data for $\delta\Delta<1$ and $\delta\Delta>1$ separately. The results are summarized in table 4.1. This table also gives the 'overall' results obtained in section 2.5.2

All values for the indices of refraction given in table 4.1 are obtained with the assumption that the oxide layers grown on Fe(100) and Fe(110) are flat. Under this assumption, we notice that the values obtained for the refractive index differ from literature values for bulk oxides. This is not surprising, because values for thin layers can differ considerably from those of bulk materials [78]. Especially the values of k are larger than the (low) bulk values, corresponding to a lower resistivity in the film than in the bulk oxide [79].

In section 4.2.1, we have found that the oxidation state of Fe atoms in the oxide formed at RT changes at 4×10^{15} O atoms/cm^2. It is not surprising that this change in the oxidation state (and probably also in the oxide structure) leads to a change in the refractive index at approximately 4×10^{15} O atoms/cm^2. Furthermore, also the possible presence of roughness or growth of oxide islands may cause a change in the (apparent) index of refraction [13,80]. The growth of the first 3.9×10^{15} atoms/cm^2 corresponds to the regime where the supply of oxygen from the gas is rate limiting (see chapter 5). Possibly, during this regime, oxide nuclei form which rapidly reach a thickness of about 3 ML and then grow laterally, until coalescence is reached at 3.9×10^{15} O atoms/cm^2. After this, a flat oxide layer continues to grow.

4.4 Room Temperature: Determination of the Moving Species and the Influence of Nitrogen

For high temperatures, iron is the moving species in the oxide growth [6]. This was shown by a combination of sputter-AES and NRA. However, the depth resolution obtained with this technique ($\sim 10^{16}$ atoms/cm^2) is not sufficient to determine the moving species for low temperature oxide growth.

Therefore, we used a nitrogen monolayer as a marker to determine the moving species in the oxidation. For this purpose, first we determined the amount of nitrogen deposited using ERD. Then we had to assess that the presence of nitrogen does not influence the oxidation. This was done using ellipsometry, ERD and XPS.

Finally, the depth distribution of the nitrogen layer was determined using angle resolved XPS and by monitoring the evolution of the N(1s) peak as a function of the oxide thickness.

4.4.1 Formation of the N Marker Layer

Nitrogen was introduced using the sputter source in an ambient of 3.0×10^{-5} mbar N_2 at 1500 eV for 1 hour. The sample current was approximately 20 μA/cm^2. After this implantation step the sample was heated to 700K for 40 minutes to heal the induced lattice damage. Some samples were annealed at a lower temperature of 600K.

In figure 4.9 the ERD spectra (before and after 600K annealing) of the N implanted Fe(110) sample are shown. For both cases only a peak due to N was visible. From the peak integral an areal density of 1.4×10^{15} atoms/cm^2 nitrogen after annealing was calculated. Also after 700K anneal cycles, the amount of nitrogen remaining amounted to approximately 1.4×10^{15} atoms/cm^2. It is clear that during the anneal step most of the nitrogen present after implantation has disappeared from the surface region of the sample (probably into the bulk [81–83]) and we assume that the remaining nitrogen is trapped at the Fe surface, which was also indicated by the AES results (large N peak after annealing). This is in agreement with the enthalpy diagram of N in Fe [82,83].

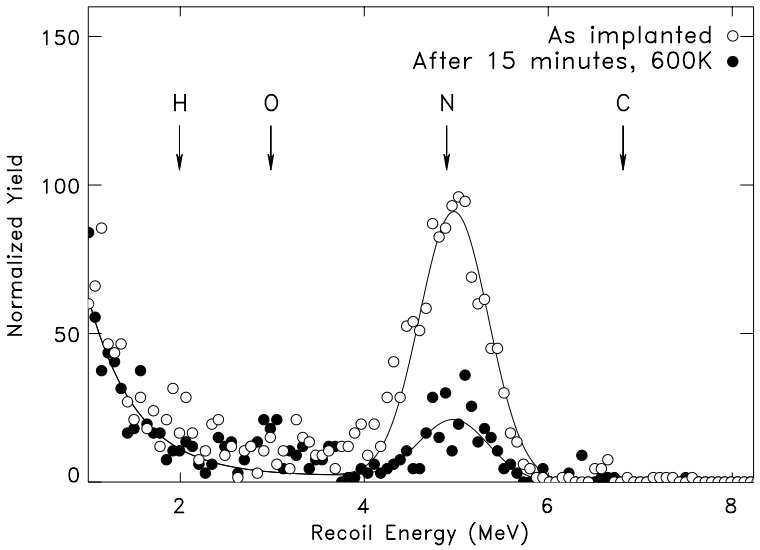

FIGURE 4.9: 35 MeV Cl ERD spectra of Fe(110): Closed circles: Implanted with N, after 600K anneal. Open circles: Implanted with N, before anneal.

4.4.2 The Influence of N on the Initial Oxidation

To measure the kinetics of the oxide layer growth ellipsometry was done during the exposure to oxygen at room temperature. Figure 4.10 shows the ellipsometry parameter $\delta\Delta$ as a function of exposure at an oxygen pressure of 10^{-6} mbar, for both a clean and a N covered sample. The annealing temperature prior to oxidation was 700K for both samples. The inset of figure 4.10 shows $\delta\Delta$ vs. exposure for the initial oxidation, measured at an oxygen pressure of 10^{-8} mbar. Apparently, the ellipsometric response is very similar.

To see whether the ellipsometric response corresponds to the same oxygen uptake in both cases, ERD measurements were performed after various oxygen exposures, indicated by the arrows in figure 4.10. The oxygen coverages are plotted in figure 4.11. Apparently, there is no clear difference in oxygen uptake with or without N pre-deposition. It should be noted that for these experiments the N covered samples were annealed at 600K. Although the resemblance in the oxygen uptake rates of the clean and N covered samples is quite clear, there is a possibility that the uptake rate is

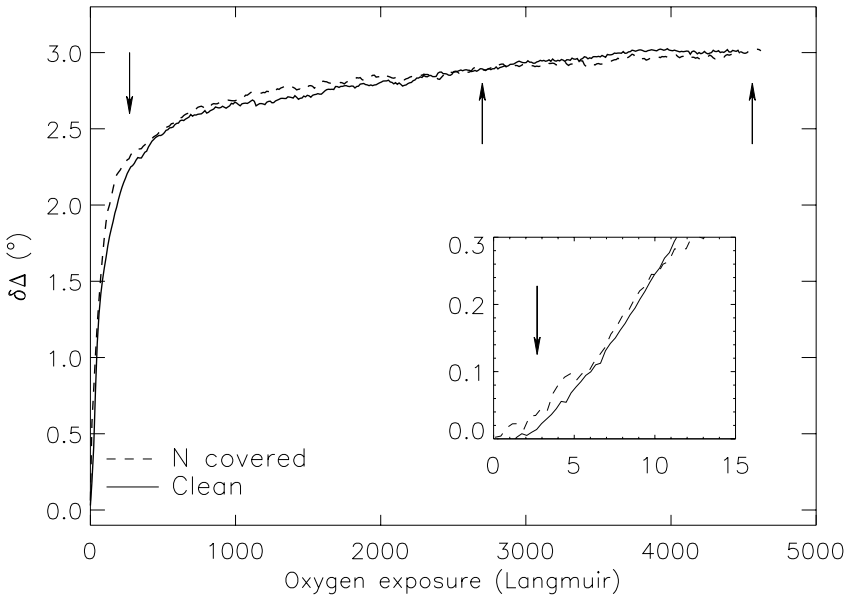

FIGURE 4.10: $\delta\Delta$ vs. oxygen exposure at an O_2 pressure of 10^{-6} mbar. Solid lines: clean Fe(110). Dashed lines: N covered Fe(110). Inset: Same experiment for low coverages at an O_2 pressure of 10^{-8} mbar. The arrows indicate exposures at which separate samples were prepared for *in-situ* ERD measurements.

influenced by the subsurface structure of the iron, which might be different due to the different annealing temperatures. This has to be investigated further. The ERD measurements also revealed that no nitrogen is lost from the surface region during oxidation at room temperature. On the other hand, because no nitrogen signal appears in the AES spectra taken after oxidation, we conclude that the nitrogen is buried under the oxide layer, presumably at the Fe/oxide interface. This we have further investigated by angular dependent XPS, reported in section 4.4.3.

Figure 4.12 shows the O(1s) and Fe(2p) XPS spectral regions of oxidized Fe(110), with and without N pre-deposition. The XPS spectra taken after oxidation at room temperature, after complete saturation, show that the valence of the iron atoms in the oxide layer is the same for the oxidation of clean and N covered Fe(110). The parameter values obtained from the reconstruction of the Fe(2p) spectrum are given in table 4.3.

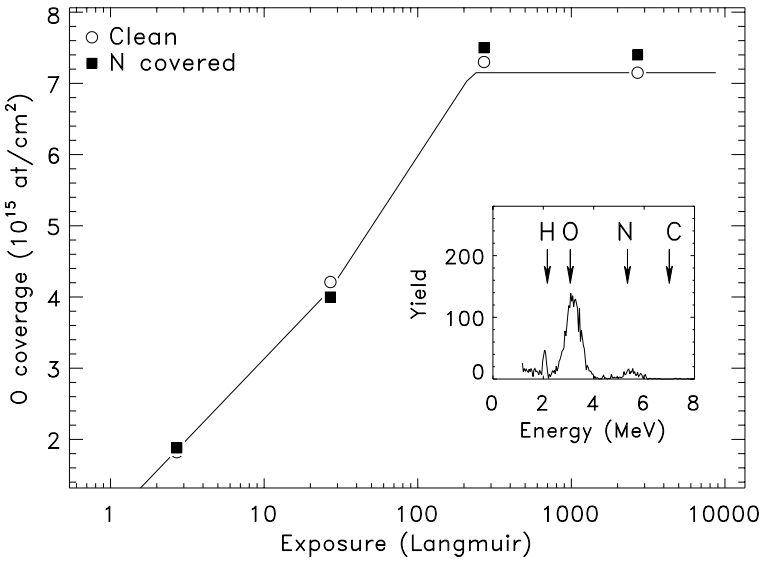

FIGURE 4.11: Oxygen coverage as measured with ERD vs. oxygen exposure. A solid line is drawn to guide the eye. Inset: Example of the ERD spectrum of the sample covered with nitrogen, after an exposure of 27 Langmuir at an oxygen pressure of 10^{-7} mbar, measured with a 36 MeV Cl beam.

Summarizing, the presence of adsorbed nitrogen has no large influence on the kinetics of the oxidation process nor on the kind of oxide that grows. After oxidation nitrogen is present under the oxide layer, presumably at the Fe/oxide interface.

Apparently, adsorbed nitrogen is inert; it does not change the chemical properties of the reactive surface nor of the growing oxide [72,73]. Hence, the fact that the N AES yield diminishes during oxidation, while the amount of N does not decrease, indicates that the mass transport which is needed for the oxide to grow, is largely carried by the iron cations, just as in the high temperature case [6].

Within our absolute accuracy of measuring Δ (1°), there is no difference between the clean and N covered substrate. XPS results show that the same oxide structure grows. A model explaining the slow change of Δ during the first 2 Langmuir is given in section 2.5. In this model, the formation of a

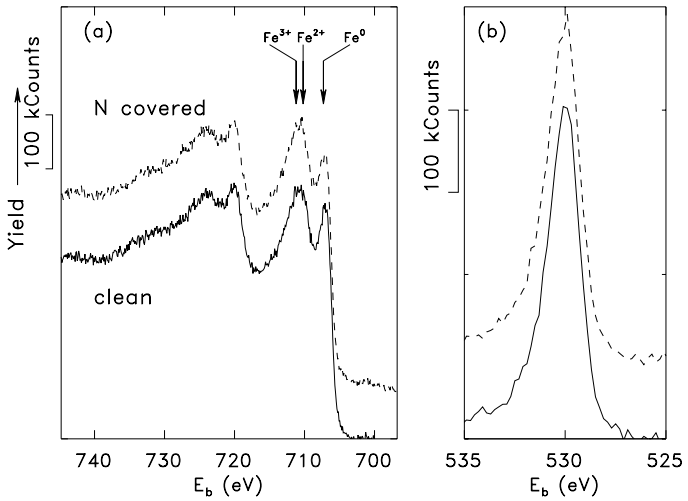

FIGURE 4.12: **(a)** Fe(2p) spectra of oxidized clean (solid line) and N covered Fe(110) after full saturation (dashed line). **(b)** O(1s) spectra.

	d_{ovl}/λ	$C_{\mathrm{Fe^{2+}}}$	$C_{\mathrm{Fe^{3+}}}$	χ^2
clean	1.18	0.57	0.43	0.98
N covered	1.21	0.55	0.44	1.05

TABLE 4.3: Parameters and value of the reduced chi square obtained from the reconstruction of the Fe(2p) spectra taken after room temperature oxidation (full saturation).

dipole layer with the iron atoms by the first monolayer of oxygen causes a low net value of $\delta\Delta$. XPS results reveal that nitrogen adsorbs as a neutral atom so that no dipole layer is present at the N covered surface. As soon as oxygen is introduced, an Fe-O dipole layer starts to form, just as in the non-covered case.

Together with the suggestion that nitrogen remains at the metal/oxide interface, this would mean that the N monolayer is an excellent marker for the study of mass transport across the interface.

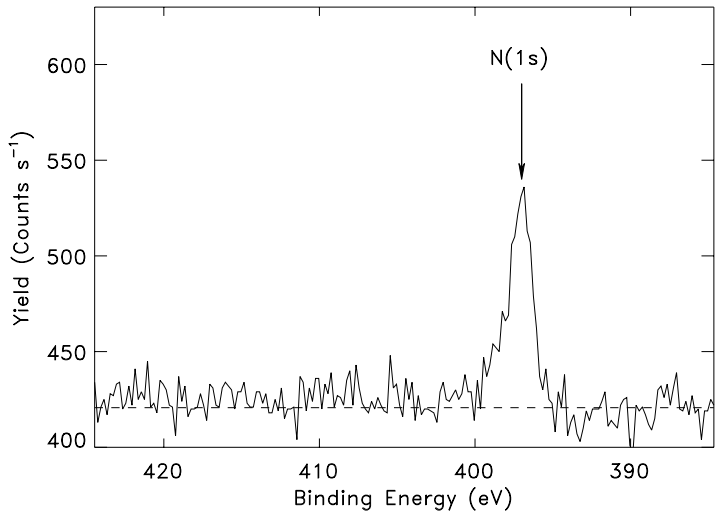

FIGURE 4.13: The N(1s) peak on Fe(110) after deposition of N. The dashed line indicates the background subtracted to obtain the N(1s) yield.

4.4.3 The Depth of the N layer

Figure 4.13 shows the N(1s) spectrum of Fe(110) after deposition of nitrogen and before oxidation. Assuming that the N forms a δ-layer at the surface, we expect no background of inelastically scattered electrons. As is indicated in the figure, the background at kinetic energies lower than that of the N(1s) peak is equal to that at higher kinetic energies. However, the amount of N present is so low, that even if the N were buried, we would not expect a detectable change of the background. The N(1s) yield (Y_{N1s}) was obtained by simply subtracting a constant background (due to inelastically scattered electrons from Fe peaks at higher kinetic energy).

Figure 4.14 shows the relative N(1s) yield ($Y_{\mathrm{N1s}}/Y^0_{\mathrm{N1s}}$) after room temperature oxidation of Fe(110), for different values of the detection angle θ. Here, Y^0_{N1s} is measured with the same value of θ, before oxidation. In this case, the oxygen coverage amounted to 8.2×10^{15} O atoms/cm^2. The angular dependence of the values of Y_{ox}, Y_{sub} and Y_{O1s}, divided by the yields of reference spectra (clean Fe and FeO) for the same value of θ showed the expected behavior, described by equations (A.3), (A.5) and (A.6). The

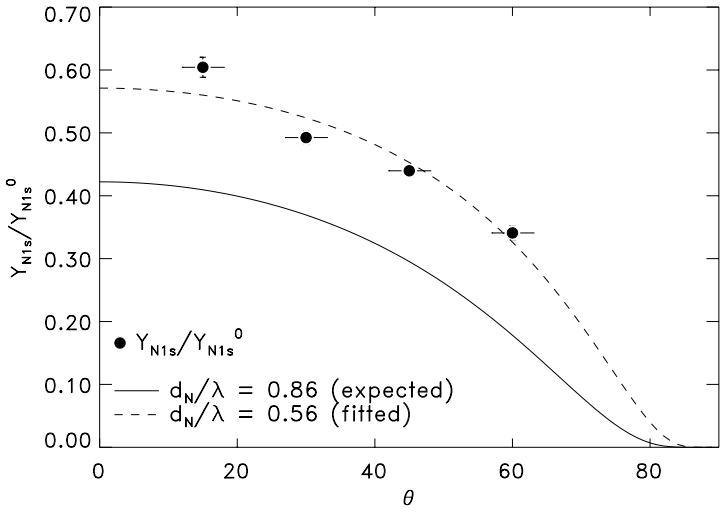

FIGURE 4.14: The relative N(1s) yield vs. detection angle θ. Solid line: N at the oxide/substrate interface ($d_N/\lambda = 0.86$). Dashed line: $d_N/\lambda = 0.56$ (fit to the data)

measured relative N(1s) yield, however, was higher than expected for all values of θ, if we assume a δ-layer at the oxide/substrate interface. The solid line in figure 4.14 shows the expected behavior for a δ-layer at the interface between the iron substrate and the oxide overlayer. The value of d_{ovl}/λ used (0.86) was obtained from an extrapolation of the fit to the formula of Seah and Dench for the AL, shown as a dashed line in figure 3.4. The data in figure 4.14 indicate that either the N is present in the sample at shallower depths than expected or the value of λ used is wrong. A fit to the function for a δ-layer buried at depth d_N (dashed line in figure 4.14) gives d_N/λ=0.56, which would mean that, if the second possibility were true, the AL is 1.5 times larger than expected from figure 3.4. Therefore, this possibility seems unrealistic.

Figure 4.15 shows the relative N(1s) yield for different thicknesses of the overlayer. The oxygen coverages on the horizontal axis were determined from the value of $\delta\Delta$. The O(1s) and Fe(2p) yields were slightly (5-10%) lower than expected from the value of $\delta\Delta$. Figure 4.15 clearly shows that, again, the N(1s) yields are higher than expected, indicating that N is not

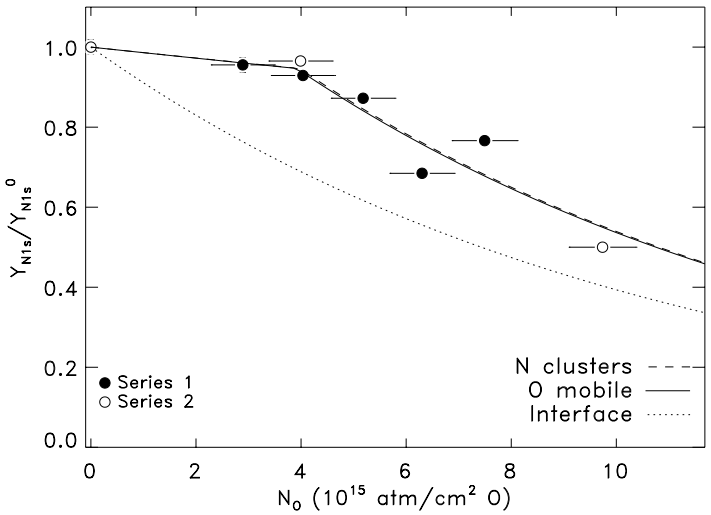

FIGURE 4.15: The relative N(1s) yield vs. oxygen coverage. The open symbols are measured during a different oxidation experiment than the solid symbols. Dotted line: N δ-layer at the oxide/substrate interface ($d_N/\lambda = 0.86$). Solid line: both O and Fe transport during the oxidation, for $N_O < N_{O,trans}$. Dashed line: oxide growth mainly between N clusters. See the text, table 4.4 and figure 4.16 for explanation of the two models.

present as a δ-layer at the metal/oxide interface. The data even suggest a slow decrease for low oxygen coverage, followed by a more rapid decrease at higher coverage. There are two possible explanations for this:

1. At low coverages, both oxygen and iron are mobile. The N marker layer is crossed by Fe cations from one side and O anions from the other. From the resulting position in the growing oxide layer, the ratio of Fe mobility to O mobility can be calculated.

2. During the anneal step before oxidation, the N forms small clusters (possibly iron nitride). During oxidation, first mostly the space between the clusters is filled. Then, a flat oxide layer grows on top of the mixed oxide/nitride layer. In this case, the N-layer does not play its role as a marker layer correctly.

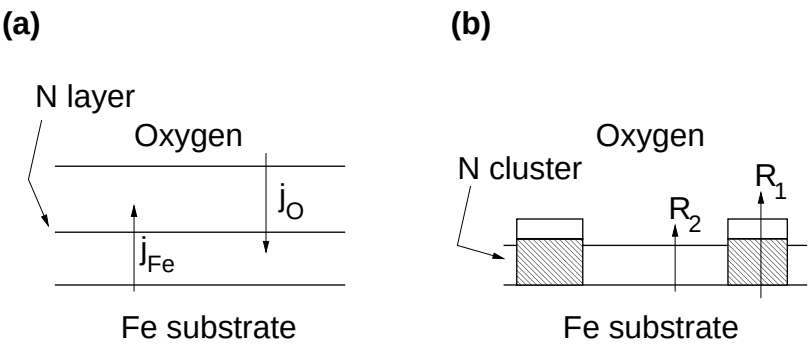

FIGURE 4.16: Schematic depictions and explanation of the fit parameters in the case: **(a)** Both O and Fe are mobile. j_{O} and j_{Fe} indicate the current densities of O and Fe, respectively. **(b)** Nitride clusters. R_1 and R_2 indicate the growth rates on and between the N clusters, respectively.

model	$N_{\mathrm{O,trans}}$	fit parameter	value
1. O mobile	$(4.0\pm0.5)\times10^{15}$ atoms/cm^2	$(j_{\mathrm{Fe}}/j_{\mathrm{O}})$	0.18 ± 0.05
2. Clusters	$(4.0\pm0.5)\times10^{15}$ atoms/cm^2	(R_1/R_2)	0.08 ± 0.05

TABLE 4.4: Parameters (for $N < N_{\mathrm{O,trans}}$) for the two possible explanations of the N(1s) yield vs. depth. The physical meaning of the fit parameters is depicted schematically in figure 4.16. $N_{\mathrm{O,trans}}$ is the total oxygen coverage at which a transition to flat layer growth occurs.

In figure 4.16, these explanations are schematically depicted. The fitted behavior for both explanations is plotted in figure 4.15. As can be seen from the figure, we cannot distinguish between the two explanations. We also investigated a model where the roughness of the oxide layer reduces the apparent value of d_{ovl}/λ, but this yielded very unlikely parameter values.

Table 4.4 gives the parameters for the fits. For both models, the transition coverage amounts to $4.0\pm0.5\times10^{15}$ atoms/cm^2. After this coverage, our results are accurately described by the Fromhold-Cook model: A flat oxide layer grows and Fe cations are transported through this oxide to the oxide/oxygen interface where the reaction takes place.

However, it is unlikely that the oxidation rate is not influenced in the

second explanation, which assumes an oxidation rate which is more than 10 times smaller through the N clusters. From figures 4.10 and 4.11, we see that the total oxidation rate is not significantly changed, which would mean that the 1.4×10^{15} atoms/cm^2 N (about 1 ML) cover only a very small fraction of the surface. In our view, this is very unrealistic.

Therefore, we conclude that the most logical explanation for our results is the first: for coverages below 4×10^{15} O atoms/cm^2, O is the most mobile species. After this coverage, our data suggest that only Fe is the mobile species and the reaction between O and Fe takes place at the oxide/oxygen interface. We emphasize that the mobility ratio given in table 4.4 is only the overall resultant mobility ratio which does not necessarily reflect the actual processes taking place at the microscopic level. Nevertheless, the apparent mobility of oxygen for low coverages suggests that the Fromhold-Cook model is not valid for oxide layers consisting of less than 3 ML of oxide (4×10^{15} O atoms/cm^2).

4.5 Discussion

In many previous studies of the initial oxidation and oxidation kinetics of Fe(100), the growth of a homogeneous layer was assumed [10,67–71,74].

Indeed, our data (especially from XPS) also show that at $T = 473$K a homogeneous oxide, with composition $Fe_{0.9}O$ and containing mainly Fe^{2+} forms.

At room temperature, however, a two-layer system forms. Several observations led us to this conclusion. At roughly the same oxygen coverage (3.9×10^{15} O atoms/cm^2), there is:

1. A transition of a layer containing Fe^{2+} only (FeO) to a layer containing both Fe^{2+} and Fe^{3+} (a mixture of FeO and γ-Fe_2O_3). (Section 4.2.)

2. A change in the optical constant of the oxide layer. (Section 4.3.)

3. A change in the apparent mobility of O atoms. (Section 4.4.)

As will be shown in chapter 5, for oxygen coverages below 4×10^{15} atoms cm^{-2}, the growth rate is determined by the oxygen flux from the O_2 gas. The maximum cation and electron current to the surface, extrapolated from data at higher coverages, are more than one order of magnitude larger than

the oxidation rate. Therefore, it is hard to believe that the oxygen is really moving into the grown oxide layer.

In spite of this, we concluded in section 4.4 that mobile oxygen was a more probable explanation of the XPS results than the formation of N clusters. In section 4.3, we mentioned oxide clusters or, alternatively, the growth of a different oxide, as a possible explanation for the change of the optical properties. The XPS results unambiguously indicated the growth of a different oxide.

These seemingly incompatible observations can be combined into a coherent description of the oxidation process. We assume that for $N_O < 4\times10^{15}$ atoms/cm^2, the oxide coverage increases by the nucleation and growth of oxide clusters. Because the oxygen incorporation rate is entirely limited by the oxygen flux from the gas phase, it is not affected by the deposition of N (which might change the density of growing nuclei). During the lateral growth of the nuclei, the N atoms remain almost entirely at the surface. At $N_O = 4\times10^{15}$ atoms/cm^2, the clusters coalesce and further oxidation proceeds via the homogeneous thickening of the oxide layer present. Simultaneously, the oxidation state of iron changes. During the growth of this new phase with stoichiometry $Fe_{0.77}O$, Fe cations are the moving species. The N marker atoms remain at the FeO/$Fe_{0.77}$O interface.

4.6 Conclusions

We investigated the optical constant of the oxide layer grown in O_2 on Fe(100) and Fe(110). Using XPS, we determined the oxidation state of iron in the oxide layer. The influence of a N marker layer on the oxidation was investigated and using this marker the mobile species during oxidation was determined. From the results, the following conclusions can be drawn:

1. At room temperature, a double layer structure evolves. Up to $N_{O,trans}$ ($\sim4\times10^{15}$ O atoms/cm^2), a homogeneous layer forms, containing only Fe^{2+}. Above $N_{O,trans}$, a layer containing both Fe^{2+} and Fe^{3+} forms, with a stoichiometry of $Fe_{0.77}O$.

2. The change in oxide structure at $N_{O,trans}$ is also reflected in a change of the index of refraction, corresponding to the formation of a γ-Fe_2O_3-like oxide. In addition, at $N_{O,trans}$, the growth mode and corresponding mass transport seem to change from nucleation and (lat-

eral) growth to in-depth growth with the Fe cations as the moving species.

3. The amount of Fe^{3+} decreases with increasing oxidation or annealing temperature, until, at $T = 473$K , an oxide layer containing almost only Fe^{2+}remains.

4. During oxidation, some Fe^0 is displaced from lattice positions and possibly incorporated in the oxide layer.

5. Covering Fe(110) with nitrogen does not change the oxygen uptake rate or the chemical properties of the growing oxide at room temperature. The nitrogen seems to reside at the oxide/oxide interface of the double layer.

The growth of an oxide double layer implies that special care has to be taken for the description of the initial oxidation of Fe(100) in O_2.

Chapter 5

The Passivation of Iron: Application of the Fromhold-Cook Model to the Initial Oxidation of Fe(100) in O_2

5.1 Introduction

The understanding of the mechanism and the kinetics of the initial oxidation of metals is a frequent topic in the physics and chemistry of surfaces and thin layers. The Fromhold-Cook theory (FC) [1,72,73,84] describes the initial oxidation of metals (0-20 nm). It potentially unifies oxidation kinetics for plasma induced oxidation, anodic (electrochemical) oxidation and thermal oxidation, including a description of temperature dependence, metal (surface orientation) dependence and the dependence on (externally applied) electric fields.

In the FC-theory, the reaction between metal and oxygen takes place at the growing oxide/oxygen interface, requiring both metal ions and electrons to move through the oxide layer to the surface. An important feature of the FC theory is the concept of coupled currents: the net electrical current across the oxide layer is zero. At sufficiently high oxygen pressures, transport of either electrons or metal ions is rate-limiting. The transport of electrons can proceed by two mechanisms: tunneling and thermionic emission. For temperatures below 420K, there is virtually no thermionic emission at the metal-oxide interface, and electron tunneling is the dom-

inant process. The Fromhold-Cook model is described in more detail in section 5.4.

Leibbrandt *et al* [6] demonstrated that the oxidation of Fe(100) represents a model system to test the FC theory. For a few ML thin oxide films, they deduced the value for the energy barrier for thermionic emission of electrons from the Fe Fermi level into the oxide conduction band. They also showed that Fe ions are the moving species in the oxide growth. The Fromhold-Cook theory states that at low temperatures the oxide layer growth effectively stops at the thickness, where the tunnel current of electrons through the oxide becomes negligibly small. This is indeed observed: at room temperature the oxide growth virtually stops [6,85].

However, there is one problem left: unlike the predictions of Fromhold that this saturation thickness does not depend strongly on the oxidation temperature [1], the measurements indicate an increase in saturation oxide thickness with increasing temperature for *e.g.* Fe [6] and Co [86]. This suggests that not only the decrease of the tunnel current retards the oxide growth, but that also another factor is relevant.

In chapter 4, we have shown that the room temperature grown oxide layer consists of two parts, one containing only Fe^{2+} and a part containing both Fe^{3+} and Fe^{2+}, the latter part being present at the larger oxide thickness.

This presence of a mixed oxide layer may have important consequences for the kinetics of oxide layer growth and the modeling thereof: in an earlier combined electrochemical and surface analytical study it has been concluded that Fe^{3+} oxide layers may act as a barrier for ion transport, and therefore may cause oxidation rates to diminish [87]. However, kinetic modeling in oxidation studies is based on simple oxidation models, usually assuming the growth of a homogeneous layer [88–91].

By modeling the oxidation using FC-theory, more information on the nature of the passivating layer might be obtained.

Therefore, we carefully investigated the oxide electronic structure and stoichiometry on a Fe(100) single crystal as a result of low pressure exposure to O_2 at different temperatures and correlated this to the oxidation rate. This is achieved by combining ellipsometry, the high energy ion beam technique Elastic Recoil Detection (ERD) [22] and (polar angle resolved) X-ray photo- electron spectroscopy (XPS). This enables us to probe both the monolayer regime and the range of oxide layer thicknesses up to 10 nm.

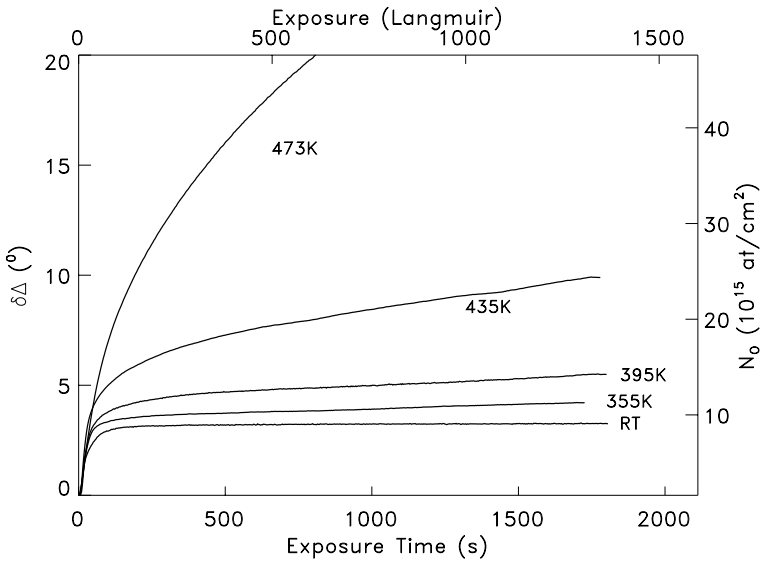

FIGURE 5.1: $\delta\Delta$ vs. time during 10^{-6} mbar O_2 exposure of Fe(100) at the sample temperatures indicated.

5.2 Temperature Dependence of the Oxidation Kinetics

Figure 5.1 shows the growth curves of Fe(100), exposed at different temperatures to 1.0×10^{-6} mbar O_2. For low coverages (N_O <5×10^{15} atoms/cm^2), the amount of oxygen incorporated increases linearly with the exposure. Here, the reactant supply is rate-limiting. At 473K, the oxidation does not saturate. At temperatures below 420K near saturation is observed. According to the FC-formalism, at $T \leq 420$K, electron transport proceeds by tunneling through the oxide layer and therefore the limiting film thickness should be nearly independent of the oxidation temperature. However, the measurements show that the saturation thickness does depend on the temperature and varies between 8.5×10^{15} O atoms/cm^2 at room temperature (RT) and 15×10^{15} O atoms/cm^2 (395K). In figure 5.2, the oxidation rate vs. oxygen coverage, calculated from the measurements shown in figure 5.1, are shown.

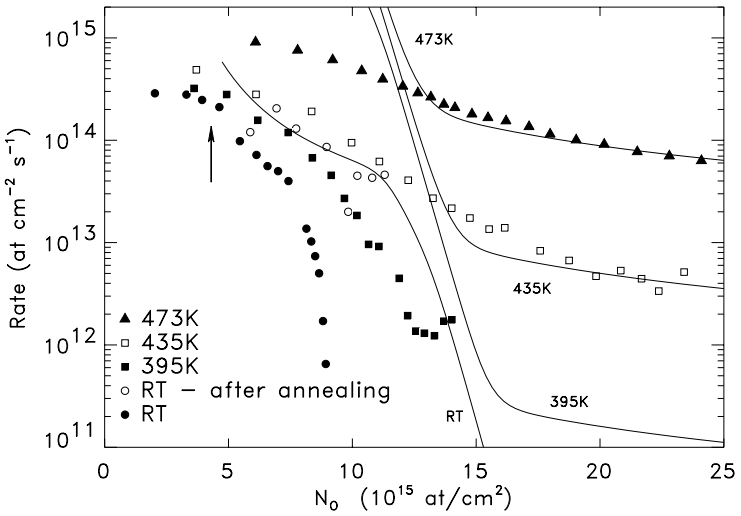

FIGURE 5.2: Oxygen incorporation rate vs. oxygen coverage. Solid circles: Fe(100), RT. The arrow indicates the formation of the second Fe^{3+} containing layer. Solid lines: FC-model (explained in the text).

5.3 The Influence of Fe^{3+}

In chapter 4, we investigated the oxidation state of iron atoms in the oxide layer. We deduced from the results that a two-layer system is formed, with a first layer containing Fe^{2+} only, and a top layer containing both Fe^{3+} and Fe^{2+}. The growth of the second layer starts at an oxygen coverage of 4.0×10^{15} O atoms/cm^2 and consists of $Fe_{0.77}O$ (which is probably a mixture of FeO and γ-Fe_2O_3). At higher oxidation temperatures, the relative fraction of Fe^{3+} in the formed oxide decreases. The oxide layer formed in O_2 at 473K consists of Fe^{2+} only.

In figure 5.2, the rate of oxygen incorporation at room temperature is plotted as a function of N_O (solid circles). At N_O=4.5×10^{15} O atoms/cm^2, when the formation of the Fe^{3+} containing second layer has just commenced, the rate decreases drastically (indicated with the arrow in figure 5.2). So, the decrease of the oxidation rate coincides with the formation of an oxide layer containing Fe^{3+}.

Let us hypothesize that, at RT, the Fe^{3+}-containing layer forms a barrier

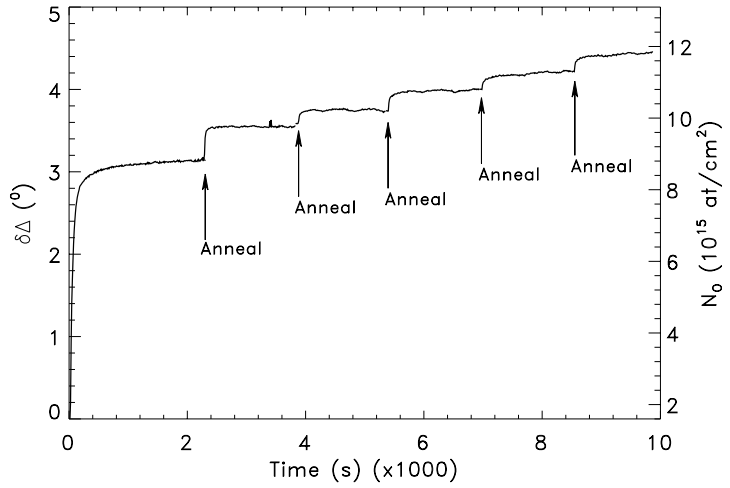

FIGURE 5.3: $\delta\Delta$ vs. oxidation time for RT oxidation of Fe(100). 15 minutes 475K anneal periods are indicated with arrows.

for further oxidation. To test this hypothesis, a comparison must be made with the oxidation rate at RT of a sample with an equally thick oxide layer, containing Fe^{2+} only. This can be achieved by annealing the sample after oxidation for 15 minutes in vacuum as is described in section 4.2. After this treatment, a layer consisting of Fe^{2+} only is present. In section 4.2, we concluded that part of the iron atoms, displaced during oxidation, is in the Fe^0 state. Upon annealing, Fe^{3+} is reduced to Fe^{2+}, while the displaced Fe^0 is oxidized to Fe^{2+}.

Figure 5.3 shows the RT growth curves of Fe(100) in 10^{-6} mbar O_2. After saturation, the sample is annealed as described in section 4.2.2, and, after cooling down to RT, exposed to oxygen. The annealing causes the oxygen incorporation rate to increase by a factor of $\sim$500. Then, the oxidation rate decreases again to near saturation (incorporation rate $\sim 10^{11}$ O atoms $cm^{-2}s^{-1}$). XPS measurements confirmed that this saturation of the oxidation always coincides with the presence of Fe^{3+}. Thus, removal of Fe^{3+} by annealing results in a drastic increase of the oxidation rate. We conclude that the presence of Fe^{3+} effectively hinders the oxidation.

This annealing and subsequent exposure to oxygen could be repeated

many times (figure 5.3). The total oxide thickness increased much beyond the 'initial' saturation thickness (which was in fact checked with a separate ERD measurement).

The oxidation rates directly after the subsequent annealing treatments (and for some separate experiments, where we measured the oxidation rate after the annealing treatment for oxygen coverage lower than the saturation coverage) are plotted in figure 5.2 (open circles). The RT oxidation rates measured directly after the annealing treatments mark the oxygen incorporation rate for a system with a homogeneous Fe^{2+} containing oxide layer. These data may therefore be compared with the data from high temperature oxidation (where the layer grown consists of FeO) and with the Fromhold-Cook model.

5.4 Application of the Fromhold-Cook Model

Before applying the Fromhold-Cook model (FC) to this system in section 5.4.2, let us summarize it and give the most important equations and parameters governing the oxidation rate.

5.4.1 The Fromhold-Cook Model

The Fromhold-Cook model [1,72,73,84] may be used to describe the oxidation of a metal if the following conditions are met:

1. The oxide layer thickens homogeneously.
2. Cations are the moving species across the layer (the reaction takes place at the surface of the growing oxide).
3. Only one type of oxide is involved.

Coupled-currents Condition

For the adsorbed oxygen ions to be ionized, electrons have to be transported from the metal to the surface of the growing oxide. So, both cation and electron transport is needed. Furthermore, for the formation of a charge neutral oxide layer, the net transport of charge must be zero. This is called the *coupled-currents condition* and is expressed mathematically as:

$$q_i J_i + q_e J_e = 0 \tag{5.1}$$

where q_i and q_e are the charges of the cation and the electron, respectively, J_i is the cation current density and J_e is the electron current density.

The potential V_K across the film necessary to satisfy the coupled-currents condition is termed the *kinetic potential*. Both the electron current and the cation diffusion current depend on the thickness of the oxide layer, the temperature and the magnitude and sign of the electric field in the oxide, as can be seen from the expressions given below. Therefore, also the kinetic potential is a function of oxidation temperature, oxide layer thickness and the different parameters determining the ion current and the electron current, which can be calculated using equation (5.1) and the expressions for cation diffusion and electron transport. The oxidation rate is then given by:

$$\frac{\mathrm{d}L(t)}{\mathrm{d}t} = R_i J_i(L) \tag{5.2}$$

where L is the oxide thickness and R_i represents the increase in volume of the oxide per cation arriving at the surface.

Cation Diffusion Current

The diffusion of the cations is considered as a thermally activated hopping process [1,92,93] (see figure 5.4). In the steady-state approximation and in the absence of space-charge effects, the ionic diffusion current density is given by [1,72,73,94]:

$$\begin{aligned} J_i &= 4a\nu_i \exp(-W_i/k_BT)\sinh(Z_i eE_0 a/k_BT) \\ &\quad \times \left[\frac{C_L - C_0\exp(Z_i eE_0 L(t)/k_BT)}{1-\exp(Z_i eE_0 L(t)/k_BT)}\right] \end{aligned} \tag{5.3}$$

where $2a$ is the ionic jump distance, ν is the ionic jump frequency, W is the energy barrier for ionic motion, k_B is the Boltzmann constant, T is the temperature, Z_i is the effective charge of the iron cation during transport through the lattice (expressed in units of e, the elementary charge), L is the thickness of the oxide layer and C_0 and C_L are the defect concentrations of the diffusing cations at the metal-oxide interface ($x = 0$) and the oxide-oxygen interface ($x = L$), respectively. E_0 is the surface-charge field strength in the film. If current equilibrium is reached, the value of E_0 is equal to $V_K/L(t)$.

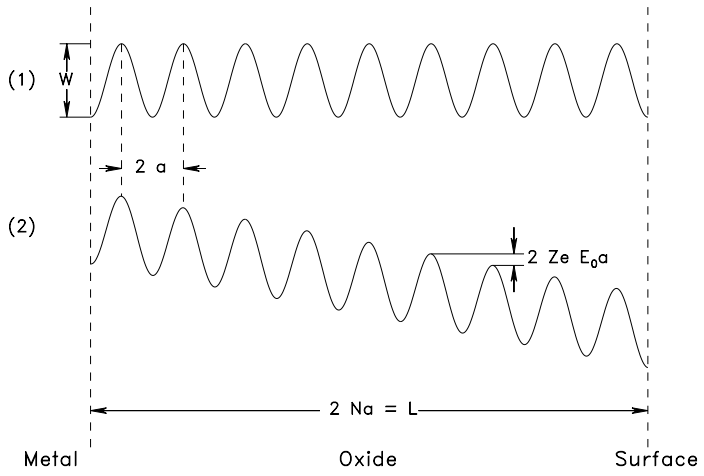

FIGURE 5.4: Potential-energy diagram for diffusion of charged particles in a discrete lattice. **(1)** No electrostatic field. **(2)** Electrostatic field enhancing the cation flux.

Electron Current due to Tunneling

Figure 5.5 gives a schematic energy-level diagram for the metal/oxide/oxygen system. For this system, at $T = 0$K, the electron flux due to tunneling through the potential barrier is given by [1,72]:

$$J_e = \frac{1}{8\pi^2\hbar L^2}[(2\chi_0 - eV_K)\exp(-\frac{L}{L_0}) - (2\chi_L + eV_K)\exp(-\frac{L}{L_L})] \quad (5.4)$$

with

$$L_0 = \hbar[m(2\chi_0 - eV_K)]^{-1/2} \quad (5.5)$$

and

$$L_L = \hbar[m(2\chi_L + eV_K)]^{-1/2} \quad (5.6)$$

The first term between brackets in equation (5.4) is the forward tunnel current from the Fermi level of the metal to the O^- level of adsorbed oxygen, while the second term represents the reverse tunnel current. In equations (5.4), (5.5) and (5.6), $\hbar = h/2\pi$, h being Planck's constant, m is the mass of the electron, χ_0 is the metal-oxide work function and χ_L is the

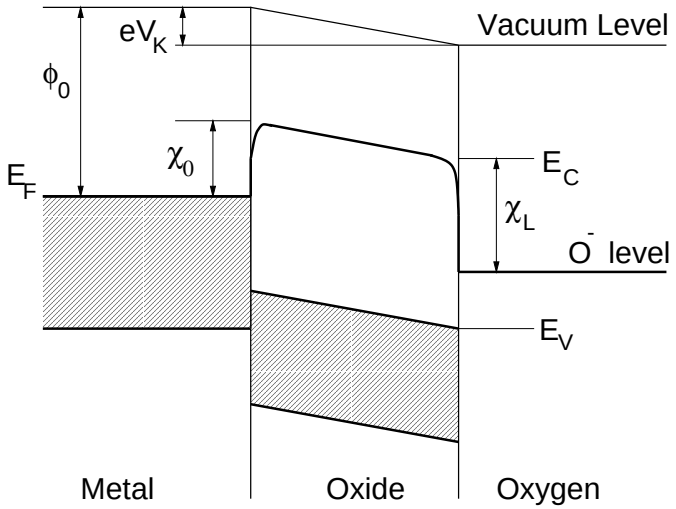

FIGURE 5.5: Energy-level diagram for the metal/oxide/oxygen system. E_F designates the Fermi energy in the metal. ϕ_0 designates the metal work function. E_V and E_C are the energies associated with respectively the top of the valence band and the bottom of the conduction band in the oxide. Important parameters for electron tunneling and thermionic emission are the metal-oxide work function χ_0 and the energy difference between the oxide conduction band and the O^- level in the adsorbed oxygen χ_L. At the oxide-oxygen interface a kinetic potential V_K is built up (which is positive if electron transport is rate-limiting and negative if Fe cation transport is rate-limiting) to ensure the current balance in the system.

oxide-oxygen work function (see figure 5.5). If $\chi_0 < \chi_L$, which is mostly the case, the first term in equation (5.4) dominates and the maximum tunnel current decreases almost exponentially with increasing thickness.

The temperature dependence of the tunnel current is given (in first order approximation) by [1,72]:

$$J_e(T)/J_e(0) = \pi\beta k_B T/\sin(\pi\beta k_B T) \tag{5.7}$$

where β is given by:

$$\beta = \frac{\sqrt{2m/\chi_0}}{\hbar} L \tag{5.8}$$

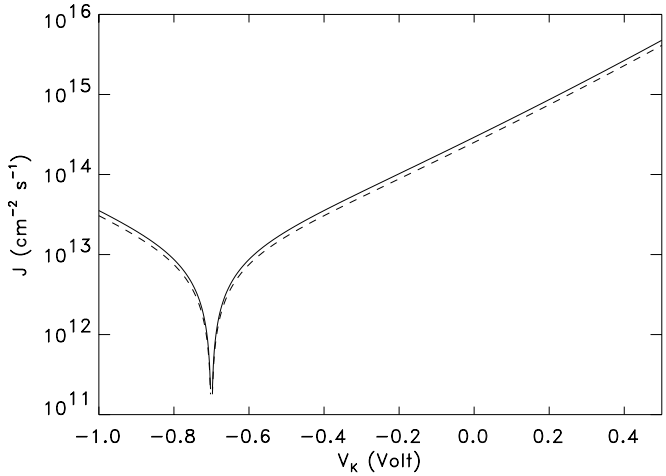

FIGURE 5.6: Electron tunnel current density versus electrostatic potential for 300K (solid curve) and for 0K (dashed curve). The values of the parameters are $\chi_0 = 1.26$ eV and $L = 2.5$ nm.

Figure 5.6 shows the electron tunnel current versus electrostatic potential for 0K and 300K through a 2.5 nm film. The difference between the two curves is very small. For the situation of figure 5.6, we have $J_e(300\text{K})/J_e(0\text{K}) = 1.16$. For thinner oxide layers, this ratio decreases towards unity. The small temperature dependence depicted in figure 5.6 implies that the saturation thickness for the low-temperature oxidation ($T \leq 420$K) is, according to the FC theory, almost independent of temperature.

Electron Current due to Thermionic Emission

For larger oxide thicknesses ($L > 3$ nm) and higher temperatures ($T > 420$K), the dominant electron transport process is thermionic emission. The electron current due to thermionic emission is given by [1,73]:

$$J_e = A_R T^2 \exp(-Q_m^{(f)}/k_B T) - n_{\text{O}^-}\nu_e \exp(-Q_m^{(r)}/k_B T) \qquad (5.9)$$

where A_R is Richardson's constant ($= 4\pi m k_B^2/h^3$) and ν_e is the electron jump frequency. If the cation current is rate-limiting, the density of filled

O^- levels n_{O^-} is given by: $E_0 = en_{O^-}/\epsilon$, where ϵ is the dielectric constant of the oxide film and E_0 is the (positive) surface-charge field. For the case of negative surface-charge fields (electron current is rate-limiting), n_{O^-} is zero. $Q_m^{(f)}$ and $Q_m^{(r)}$ are the forward and reverse barrier heights, respectively. Due to image charges, the forward barrier height is not equal to χ_0 but slightly lower (as can be seen from figure 5.5). The same applies for the reverse barrier height. These barrier heights can be calculated with [1,73]:

$$\begin{aligned} Q^{(f)}(x) &= \chi_0 + eE_0x - (e^2/4\epsilon x) - [2\pi e^2\gamma\sigma/(\epsilon+\epsilon_0)^2](L-x)^{-2} \\ Q^{(r)}(x) &= \chi_L - (e^2/4\epsilon x) - eE_0(L-x) - [2\pi e^2\gamma\sigma/(\epsilon+\epsilon_0)^2](L-x)^{-2} \end{aligned} \tag{5.10}$$

where γ is the molecular polarizability for oxygen and σ the density of adsorbed molecules. The terms involving ϵ are due to image charges in the oxide layer. The position of the barrier maximum at $x = x_m$ is given by $\mathrm{d}Q^{(f)}/\mathrm{d}x = \mathrm{d}Q^{(r)}/\mathrm{d}x = 0$ and the maximum barrier heights in equation (5.9) are given by $Q_m^{(f)} = Q^{(f)}(x_m)$ and $Q_m^{(r)} = Q^{(r)}(x_m)$.

5.4.2 The Oxidation of Fe(100)

We now apply the FC model to our RT data of the homogeneous oxide, *i.e.* taken after annealing (open circles in figure 5.2). For χ_0 we take $\chi_0 = 1.26$ eV, obtained by Leibbrandt for the same oxide on Fe(100) by fitting the oxidation curves at $T > 420$K to a FC model taking into account only thermionic emission for the electron transport [6]. Also, the ratio C_0/C_L and the value for Z_i are taken from [6]. The remaining parameters needed to fit the RT data to the FC model with electron tunneling are χ_L, W and C_0. The RT data for $N_O < 12{\times}10^{15}$ O atoms/cm^2 could be fitted well using the FC formalism. The resulting parameter values for $Z_i = 1e$ are given in table 5.1 and the calculated dependence of the oxidation rate on the oxygen coverage plotted in figure 5.2. In fact, a range of parameters could fit the measurements. For example, the ionic diffusion coefficient D at RT could be taken between $2{\times}10^{-16}$ cm^2/s and $5{\times}10^{-13}$ cm^2/s, the effective charge Z_i of the diffusing cations between $1e$ and $3e$, and, in the same time, the ionic defect concentration at the metal-oxide interface C_0 between 10^{18} cm^{-3} and $5{\times}10^{19}$ cm^{-3}. For all possible values of the parameters, the cation diffusion is rate-limiting up to an oxygen coverage of about $12{\times}10^{15}$ atoms/cm^2. At this coverage, the

Parameter	Value	Comments
χ_0 (eV)	1.26	Metal-oxide work function [6]
χ_L (eV)	1.94	O^--oxide work function
W_i (eV)	0.64	Thermal activation energy for ionic motion
$2a$ (nm)	0.32	Ionic jump distance [92]
ν_i (s^{-1})	1.0×10^{13}	Ionic vibration frequency
Z_i (e)	1	Effective charge of the iron cation [92]
D_i (cm^2/s)	4.2×10^{-13}	RT ionic diffusion coefficient $(= 4a^2\nu^2 \exp(-\frac{W_i}{kT}))$ [92]
C_0 (cm^{-3})	10^{18}	Ionic-defect concentration at metal-oxide interface [92]
C_L (cm^{-3})	10^{15}	Ionic-defect concentration at oxide-oxygen interface [6,92]
R_i (nm^3)	0.21	Oxide volume increase per transported ionic defect (value for FeO)
ϵ	5.8	Relative dielectric constant (section 4.3)
$\gamma\sigma$ (cm)	1.6×10^{-9}	product of molecular polarizability and density of adsorbed molecules [95]

TABLE 5.1: Parameters and values for the FC model, obtained from a fit to the oxidation curves. References are given where values from the literature are used.

electron tunnel current decreases rapidly. It becomes rate-limiting and, at a slightly larger coverage (15×10^{15} atoms/cm^2), the oxide growth rate becomes lower than 10^{11} atoms cm^{-2} s^{-1}. This saturation coverage could not be determined from the RT only oxidation data, because there it is the formation of Fe^{3+} which determines the saturation.

Unfortunately, the true RT oxidation rates for oxygen coverages larger than 15×10^{15} O atoms/cm^2 turned out to be not experimentally accessible. Both the electron tunneling current and the thermionic emission current are well below 10^{10} $cm^{-2}s^{-1}$ for all reasonable parameter values. Nevertheless, we found that the oxygen coverage still increases rapidly during the exposure to oxygen at RT (after an anneal at $T = 473$K) even much beyond 15×10^{15} O atoms/cm^2. However, our ellipsometry data indicate that the number of additional oxygen atoms does not exceed one monolayer (1×10^{15} O atoms/cm^2) at these oxygen coverages. This leads to the following explanation: During the 475K anneal, electrons and cations are transported to the surface of the sample. The Fe^{3+} present near the surface is reduced

to Fe^{2+}. During the RT oxidation following the anneal, the Fe^{2+} in the surface monolayer is oxidized to Fe^{3+}, a process for which cation transport or electron transport across the oxide layer is not necessary.

To complete the picture, also the high temperature oxidation curves are calculated with the FC scheme using the range of parameter values which applied to the RT data. Figure 5.2 shows the oxygen incorporation rate vs. thickness plots obtained from the oxidation curves at $T = 395K$, 435K and 473K shown in figure 5.1. The lines in this figure indicate the calculated oxygen incorporation rates using the same parameter set for all curves, which is the same as used for the RT oxidation (see table 5.1). For thicknesses larger than $\sim 15 \times 10^{15}$ O atoms/cm^2, where the rate is dominantly determined by thermionic emission, the agreement between model and experiment is excellent at $T = 435$K and $T = 473$K. For lower thicknesses the oxidation rates are determined by the arrival rate of oxygen from the gas phase. For the oxidation at $T = 395$K, where we determined the Fe^{3+} fraction to be $\sim 15\%$ (see figure 4.5), the oxidation rate is much lower than follows from the calculation. So, even at this temperature the oxidation rate and final oxide thickness seem influenced by the presence of Fe^{3+}.

5.5 Discussion

Summarizing, one set of parameters was used to describe the oxidation rate over a wide range of temperatures and thicknesses. This means that a consistent picture of oxidation appears. For higher temperatures and larger oxide thicknesses, the thermionic emission of electrons is rate-limiting. For lower temperatures and smaller oxide thicknesses the presence of Fe^{3+} drastically decreases the oxidation rate. If we remove the Fe^{3+} by annealing and measure the oxidation rate after this anneal step, the RT results are consistently described by the FC model with the same parameters as for higher temperatures. At RT, for most of the oxidation trajectory, the transport of iron cations is rate-limiting.

Within the framework of the FC theory, there are two possible causes for the passivation occurring when Fe^{3+} forms: **(1)** The cation diffusion in the passivating Fe^{3+} layer is much slower than in the defect-rich Fe^{2+} containing layer (due to either a larger value of W or a drastic decrease of C_0). **(2)** The electron tunnel current through the passivating layer is much lower than through the Fe^{2+} layer, due to a larger value of χ_0. If we

assume the second explanation, the saturation at 10×10^{15} O atoms/cm^2 would result in a value for χ_0 amounting to ~5.5 eV. The work function ϕ_0 of Fe amounts to 4.7 eV [95]. As can be seen from figure 5.5, χ_0 cannot be larger than the work function. We therefore conclude that it must be the hampered cation diffusion in a Fe^{3+} containing oxide which impedes the growth.

We could not assess whether the passivation due to the formation of Fe^{3+} is caused by a larger value of W or by a lower value of C_0. In any case, the result is a decrease of the cation current as soon as Fe^{3+} starts to form. The formation of Fe^{3+} may be due to some restructuration in the film (relaxation of stresses). As soon as this happens, the presence of Fe^{3+} leads to a decrease of the cation current. Possibly, this decrease of the cation current is compensated for (by the system) with the formation of more Fe^{3+} containing oxide (lower Fe/O ratio, so less Fe transport is needed), leading to a further decrease. This (self-amplifying) process stops when there is enough Fe^{3+} to cause saturation around 8.5×10^{15} atoms/cm^2.

A different explanation is that Fe^{3+} is formed (after 4×10^{15} O atoms cm^{-2}) at all temperatures. The reduction rate of Fe^{3+} to Fe^{2+} increases with increasing temperature. At lower temperatures the low reduction rate leads to the formation of a Fe^{3+} containing passivating top layer.

5.6 Conclusions

In conclusion, by a combination of surface and thin film techniques we have been able to identify the thin Fe^{3+} containing layer as the effective barrier against oxidation of Fe(100) in O_2. By reducing the Fe^{3+} to Fe^{2+} during an anneal step we could study the formation and growth of a homogeneous oxide layer on Fe(100). At low oxidation temperatures, the oxidation rate is much slower than expected due to the formation of Fe^{3+}, while at the higher temperatures, where Fe^{3+} is not formed, the thermionic emission current dominates the electron transport. This conclusion and those of the previously performed studies of the thermionic regime [6,58] provide us with a complete picture of the thin layer oxide growth on Fe single crystals.

Chapter 6

The Room Temperature Oxidation of Fe in H_2O and H_2O/O_2 Mixtures

6.1 Introduction

A more detailed understanding of the importance of the different reaction steps in the oxidation of iron is obtained by measurement and comparison of the oxidation of iron in O_2 and H_2O. The adsorption-desorption and dissociation behavior of H_2O molecules differs largely from that of oxygen molecules [9]. Moreover, the presence of hydrogen near the surface of the oxidizing sample may influence the electronic properties of the formed oxide layer, thus influencing one of the candidate rate-limiting steps of oxidation: the transport of electrons from the substrate to the surface.

Some experimental studies have been published about the oxidation of iron in water. Early studies already indicated that H_2O chemisorbs dissociatively on Fe(100) [96,97]. Adsorbed hydroxyl (OH_a) seems to be the stablest surface species. Dwyer and co-workers [96] used AES and LEED to show that the oxidation of Fe(100) does not proceed as efficiently in water vapor as in oxygen, which was explained with passivation of the surface towards the formation of a three-dimensional oxide by hydroxyl groups. They proposed the existence of a precursor state, which can either desorb or dissociate irreversibly. The existence of this precursor state has been confirmed by the work of Hung *et al* [98], who used Temperature Programmed Desorption (TPD) and Electron Elastic Loss Spectroscopy (EELS) to in-

vestigate the interaction of H_2O with clean and oxygen pre-dosed Fe(100). The molecularly adsorbed H_2O precursor desorbs at ∼200K. At ∼310K, hydrogen desorption was found, which is evidence for the dissociation of H_2O. In contrast, Dwyer *et al* [99] found OH_a after exposing Fe(110) to water vapor at 225K. They found evidence for O_a after heating to 315K, but they did not observe hydrogen desorption below 360K. To explain this, they proposed the following reaction: $2OH_a \rightarrow O_a + H_2O\uparrow$. In conclusion, below 225K, OH_a is the stablest adsorbate. Above this temperature, also O_a seems to be present for all reaction mechanisms proposed. On both iron surfaces, a passivating layer is formed [96,99]. However, the nature of this passivating layer (coverage, composition) has never been analyzed quantitatively.

Studies on the interaction between iron oxides and water vapor reveal that the adsorption and dissociation behavior is very sensitive to the surface structure. Changing the surface of α-Fe_2O_3 by Ar bombardment facilitates the dissociation of water [100,101]. On this surface, Hendewerk *et al* [100] found H_2 desorption at ∼350K. In contrast, Murray and coworkers [101] did not find evidence for H_2 formation on the same surface. On α-Fe_2O_3, water desorption from the recombination of hydroxyl species was seen at 350K or at 405K, depending on the nature of the surface reconstruction [102].

Furthermore, the exposure of Fe(100) and Fe(110) to H_2O vapor may lead to the formation of oxides with a stoichiometry and surface structure which is different from the much studied Fe_2O_3. Known bulk oxides are also, for example, Fe_3O_4, FeOOH, or Fe_xO (with x between 0.9 and 0.95) [3]. Finally, the properties of thin oxide layers may differ largely from those of bulk oxides, the oxide layer formed may be crystalline or amorphous, and several surface orientations and reconstructions are possible.

The aim of the investigations described in this chapter was to investigate the initial oxidation of Fe(100) and Fe(110) at room temperature, in water vapor and water/oxygen mixtures. Using ellipsometry we continuously monitored the thickness of the oxide layer during the oxidation. After oxidation, the amounts of oxygen and hydrogen on the sample were determined quantitatively using heavy ion Elastic Recoil Detection (ERD). By oxidizing in D_2O, possible isotope effects in the oxidation kinetics and structure of the oxide layer formed were investigated. Using this combination of knowledge about the oxidation kinetics and the composition of

the oxide layer, a possible oxidation mechanism is identified. In chapter 7, we will discuss the temperature dependence of the oxidation and propose a quantitative kinetic model for the oxide growth based on our results.

6.2 Hydrogen and Oxygen Content of the Oxide Layer Grown

The oxygen content of the oxide layers grown in 10^{-5} mbar H_2O vapor was measured with ERD, using a 35 MeV Cl^{6+} beam. Figure 6.1 shows an example of the ERD spectrum of Fe(100) oxidized at room temperature. In this example, the oxygen coverage amounted to 3.5×10^{15} atoms/cm^2.

From the peak integrals the areal densities of H and O are determined, although an accurate determination of the H content is difficult in this case due to the low signal/background ratio. To obtain a better accuracy in the determination of the hydrogen content of the surface region, we carried out ERD with 28 MeV Ag^{6+} and with 2.135 MeV He^{+}. A typical ERD spectrum obtained with a 28 MeV Ag^{6+} beam is shown in figure 6.2. The signal to background ratio is substantially better than when the 35 MeV Cl beam is used. The origin of the background under the hydrogen peak is not known. It is, however, proportional to the projectile fluence and could be easily subtracted to obtain the true hydrogen yield. In some cases corrections had to be made for degradation of the sample, or, for lower hydrogen coverages, the increase of the hydrogen signal intensity during the measurement, which was due to the relatively poor vacuum in the beam line. In principle, all hydrogen in the surface region is determined with ERD, including adsorbed hydrogen atoms at the surface of the sample. However, we expect the adsorbed H which is possibly present immediately after H_2O exposure to desorb within the first second after exposure to the high energy ion beam: the hydrogen detected with ERD is probably incorporated in the oxide layer (for example in the form of OH-termination at defects and at the surface).

Figure 6.3 shows the amount of hydrogen in the surface region as a function of the oxygen coverage. Because the 28 MeV Ag and 2.135 MeV He ERD spectra did not contain a peak due to recoiled oxygen, we determined the oxygen coverage from the ellipsometry parameter $\delta\Delta$, using the calibration obtained in section 6.3. There is quite a bit of scatter in the data, which is possibly due to a very strong dependence of the amount of

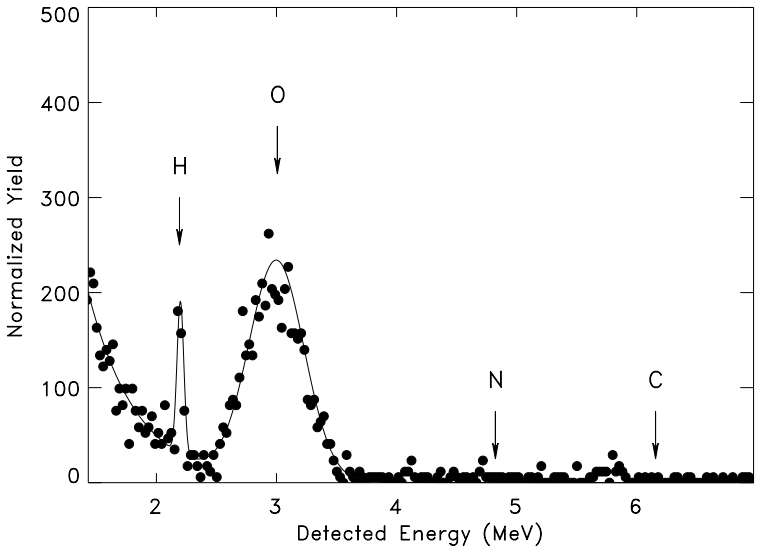

FIGURE 6.1: 35 MeV Cl^{6+} ERD spectrum of Fe(100) exposed to 4.2×10^4 L of water vapor (10^{-5} mbar). The value of $\delta\Delta$ was 1.21°.

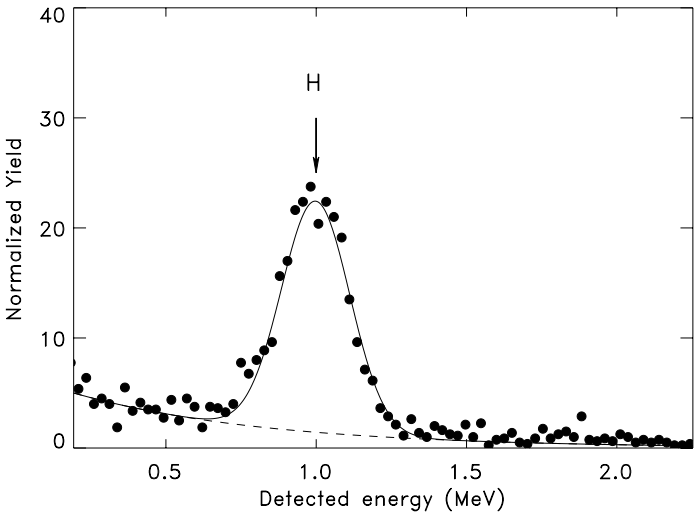

FIGURE 6.2: 28 MeV Ag^{6+} ERD spectrum of Fe(100) exposed to 1.0×10^4 L of water vapor (10^{-5} mbar). The value of $\delta\Delta$ was 0.56°. The background subtracted is indicated with a dashed line.

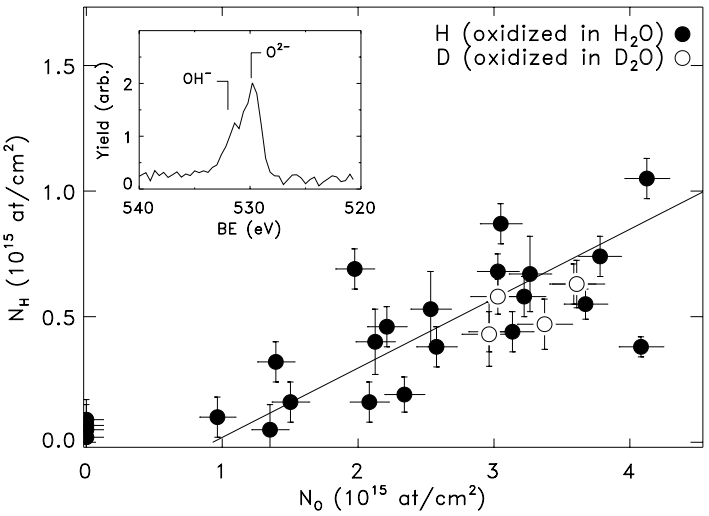

FIGURE 6.3: Hydrogen content versus oxygen content of the oxide layer formed in H_2O at RT. The solid line indicates a H/O= 0.26 after completion of the first 10^{15} atoms/cm^2. Closed circles: H content of samples oxidized in H_2O. Open circles: D content of samples oxidized in D_2O. Inset: O(1s) XPS spectrum of Fe(100) oxidized to $\delta\Delta$=1.6 in 4×10^4 L 10^{-6} mbar H_2O. O^{2-} and OH^- line positions are indicated.

hydrogen incorporated on the oxidation temperature, in combination with slight temperature variations (between 300K and 310K) from experiment to experiment. Nevertheless, the general trend is clear: hydrogen is incorporated in the oxide layer, and the average H/O ratio in the oxide is 0.28±0.02 after the first 10^{15} atoms/cm^2 (solid line in figure 6.3). Thus, the growth of FeOOH (H/O=0.5) can be ruled out. To rule out the possibility that the hydrogen incorporated was due to background vapor, we also determined the amount of D in the surface region of Fe(100) oxidized in D_2O (open circles in figure 6.3). This amount does not differ significantly from the amount of H taken up during the oxidation in H_2O.

The XPS O(1s) peaks of the samples (shown in the inset of figure 6.3) show a slight broadening towards the high binding energy side, indicating the presence of OH^- groups in the oxide layer, in agreement with previous results of Gimzewski *et al* [39].

We reconstructed the Fe(2p) parts of the XPS spectra with reference spectra of Fe, FeO, and Fe_2O_3, using the method by Graat *et al* [29–31], based on expressions derived by Hansen and Tougaard [49] (see appendix A.4). For oxygen coverages larger than 2.5×10^{15} O atoms/cm^2, the relative amount of Fe^{2+} in the oxide layer did not depend on the thickness of the oxide layer and amounted to (on average) 0.66±0.08. For thinner layers, the Fe(2p) part of the XPS spectrum is dominated by the substrate Fe^0 signal and we could not distinguish between Fe^{2+} and Fe^{3+}. If we assume that the layer consists of a mixture of FeOOH (Fe^{3+}) and FeO (Fe^{2+}), the H/O ratio calculated for the relative amount of Fe^{3+} amounts to 0.25±0.04, close to the average value obtained from our ERD data.

For the oxidation of Fe(110), however, the average value of $C_{Fe^{2+}}$ used for the reconstruction was 0.94±0.07, while the H/O ratio found with ERD amounted to 0.31±0.03 for oxygen coverages above 1×10^{15} atoms/cm^2. Possibly, in the layer formed on Fe(110), OH groups are bound to Fe^{2+} as in $Fe(OH)_2$, so the oxide consists of a mixture of FeO-like and $Fe(OH)_2$-like oxide, with a small amount of Fe^{3+}.

6.3 Calibration of the Ellipsometer

To obtain a calibration for the ellipsometry parameter $\delta\Delta$, we measured the oxygen content with ERD (using a 35 MeV Cl^{6+} beam) at various values of $\delta\Delta$ for oxide layers prepared at temperatures between room temperature and 473K, at a H_2O pressure of 1.0×10^{-5} mbar.

Figure 6.4 shows the calibration curve obtained. The parameter $\delta\Delta$ is linearly proportional to the oxygen coverage for the thickness range used in this study. The offset at the horizontal axis amounts to $(8.6\pm1.5)\times10^{14}$ atoms/cm^2, so ellipsometry is not sensitive to part of the first monolayer. The value of F_Δ found by fitting is $F_\Delta = (0.453\pm0.015)\times10^{-15}$ °cm^2/atom.

From the measured values of $\delta\Psi$, we determined F_Ψ to be $F_\Psi = (-1.3\pm 0.4)\times10^{-17}$ °cm^2/atom, which is equal to the value obtained in section 4.3 for the oxidation of Fe(100) in O_2, for oxygen coverages larger than 4×10^{15} O atoms/cm^2, where a Fe^{3+} containing layer grows.

Using the flat-layer model described in section 2.5 and assuming an oxygen density of $\rho_O = 4.75\times10^{22}$ atoms/cm^3 (bulk FeO), we obtain $N_1 = (2.96 \pm 0.13) + i(0.77 \pm 0.11)$ for the optical constant of the oxide layer grown on Fe(100) and Fe(110) in H_2O.

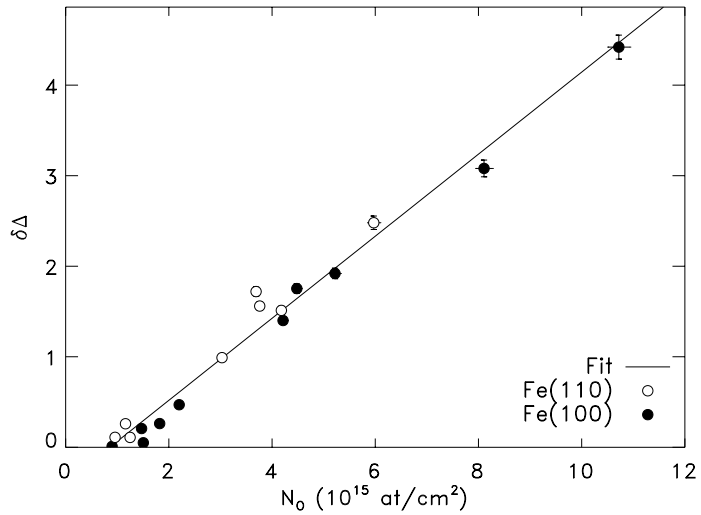

FIGURE 6.4: $\delta\Delta$ vs. oxygen coverage determined with ERD (calibration curve for the ellipsometer). Open circles: oxidation of Fe(110). Closed circles: oxidation of Fe(100). Solid line: fit to the data (see text).

For the oxidation of Fe(100) in O_2 at RT, we found $N_1 = (2.4 \pm 0.3) + i(0.6 \pm 0.2)$ for $N_O < 4{\times}10^{15}$ atoms/cm^2 (see sections 4.3 and 4.3.2). This is significantly different from the value obtained here for the oxidation in H_2O. There are two possible explanations for the difference: **(1)** A different oxide, with different optical properties, is formed. **(2)** Roughness or growth of oxide islands may cause a change in the (apparent) index of refraction [13,80]. However, a lower index of refraction is expected for the rougher oxide layer or, at equal oxygen coverages, the layer with the thickest islands. In chapter 7 we conclude that the oxidation of Fe(100) in H_2O proceeds via a nucleation and growth mechanism which implies the presence of oxide islands. In chapter 4 we also found indications of the presence of oxide islands at low oxygen coverages ($<4{\times}10^{15}$ O atoms/cm^2) for the oxidation of Fe(100) in O_2. Furthermore, the different hydrogen content of the oxide layer formed implies that the oxide structure is different: we conclude that the first explanation is more probable.

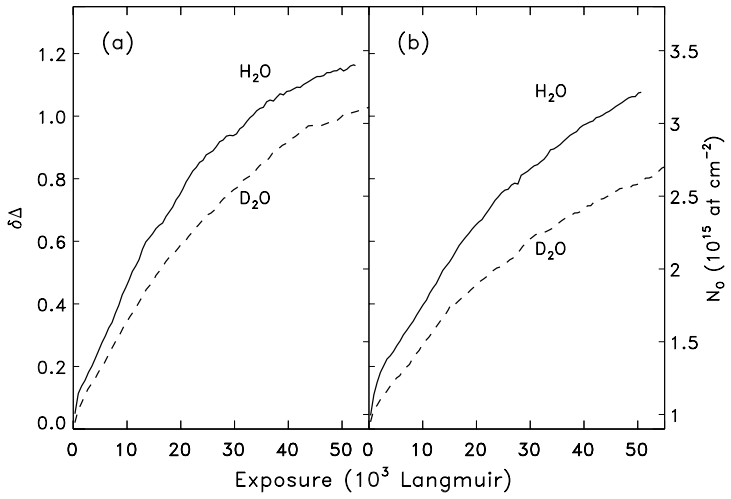

FIGURE 6.5: **(a)** Ellipsometry curve for Fe(100) at RT in 10^{-5} mbar H_2O (solid line) and D_2O (dashed line). **(b)** Ellipsometry curve for Fe(110) at RT in 10^{-5} mbar H_2O (solid line) and D_2O (dashed line).

6.4 RT Oxidation in H_2O and D_2O

The ellipsometry curve, $\delta\Delta$ vs. exposure of Fe(100) oxidized at RT in H_2O, is shown in figure 6.5 **(a)**. After a rapid initial increase to $\delta\Delta$=0.1°, the increase of $\delta\Delta$ proceeds approximately linearly in time until a value of $\delta\Delta$=0.7° is reached. From this point, the oxidation rate decreases continuously with increasing layer thickness. A similar, but slightly slower oxidation is observed for Fe(110) (figure 6.5 **(b)**).

Figure 6.5 also shows the oxidation curves for the oxidation in D_2O. From the oxidation curves in figure 6.5, we determined the oxidation rate (using the calibration for the ellipsometer given section 6.2). The oxidation rate in H_2O was then divided by the oxidation rate in D_2O (at the corresponding oxygen coverage) to obtain the ratio R_{D_2O}/R_{H_2O}, which is plotted in figure 6.6 for both Fe(100) (open symbols) and Fe(110) (closed symbols).

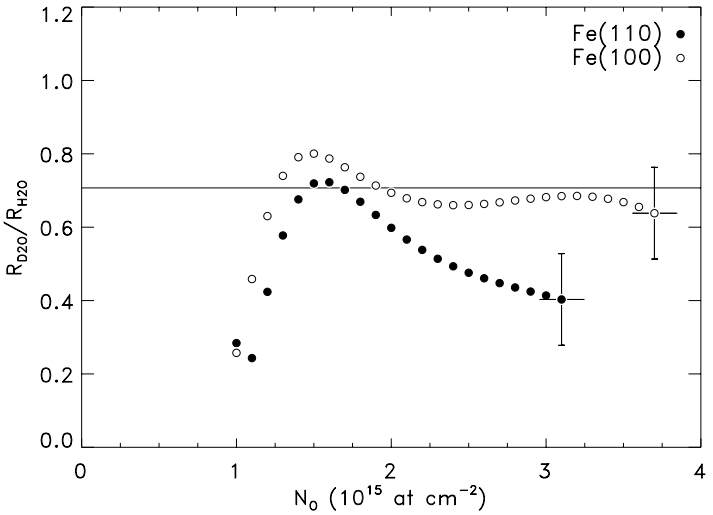

FIGURE 6.6: The ratio of the oxidation rates in D_2O and H_2O vs. oxygen coverage. The error bars indicated are valid for all points in the figure. Horizontal line: $R_{D_2O}/R_{H_2O} = 1/\sqrt{2}$, the ratio expected if the attempt frequency for the dissociation of H_2O (or OH) determines the oxidation rate (see section 6.7).

6.5 Oxidation in H_2O followed by Oxidation in O_2: the Rate-Limiting Step

To distinguish between an oxidation rate determined by properties of the oxide layer formed versus a rate determined by slow dissociation of water molecules at the oxide surface, we oxidized a Fe(100) sample in 10^{-5} mbar water vapor to a value of $\delta\Delta$=1.3°. After the water vapor has been pumped away, we exposed the sample to O_2. The oxidation rate increased with a factor of 80 (see the dashed oxidation trajectory in figure 6.7). However, the oxidation rate in oxygen was still a factor of 30 slower than that of a layer of the same thickness but grown completely in O_2 as indicated by the solid line in figure 6.7.

We also carried out this experiment for different pre-oxidation H_2O doses on Fe(100) and Fe(110). The initial oxidation rate, just after introduction of O_2, is plotted in figure 6.8 as a function of the oxygen coverage.

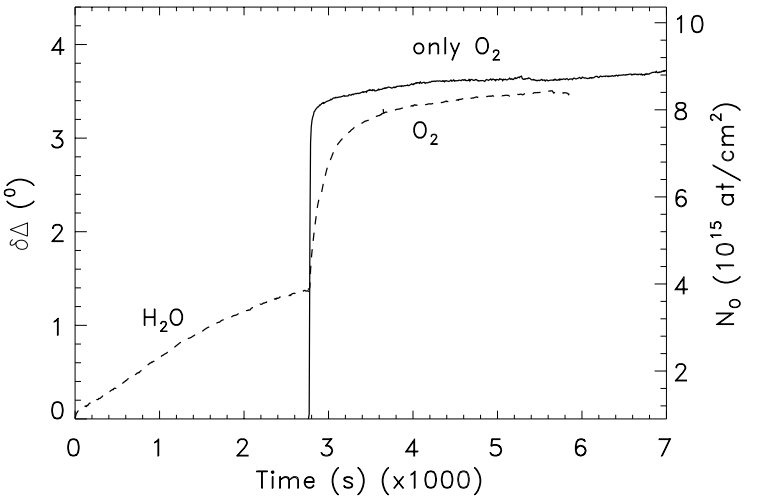

FIGURE 6.7: Ellipsometry curve for Fe(100) at RT, exposed to H_2O to $\delta\Delta$=1.3, and then oxidized in O_2, compared with oxidation in oxygen only.

This figure also contains the rate vs. coverage plots for the oxidation in 10^{-5} mbar H_2O and 10^{-5} mbar O_2 (no pre-oxidation). Again, we see that the initial rates in O_2 are orders of magnitude larger than the rates in H_2O at the same thickness, but they are still considerably lower than the rates in a non pre-oxidized sample.

These results indicate that the rate-limiting step for the oxidation of Fe in H_2O is at the surface of the growing oxide. The lower O_2 oxidation rates after pre-oxidation in H_2O (compared with oxidation in O_2 only) suggest that transport properties of the oxide layer formed in H_2O are different than those of the layer formed in pure O_2. The oxide layer formed on Fe(100) in H_2O differs from that formed in O_2 in two ways: hydrogen is incorporated and the layer contains Fe^{3+}. To test whether the lower oxidation rate after pre-oxidation in H_2O is due to the Fe^{3+} or the presence of hydrogen, we oxidized a Fe(100) sample in H_2O vapor until N_O=4.3×10^{15} atoms/cm^2 (determined with ellipsometry). Then, we annealed the sample for 15 minutes at 473K in vacuum. Combined XPS and ERD measurements revealed that during this anneal step, Fe^{3+} reduced to Fe^{2+} and the hydrogen content decreased from 7.4×10^{14} atoms/cm^2 to 2.4×10^{14} atoms/cm^2.

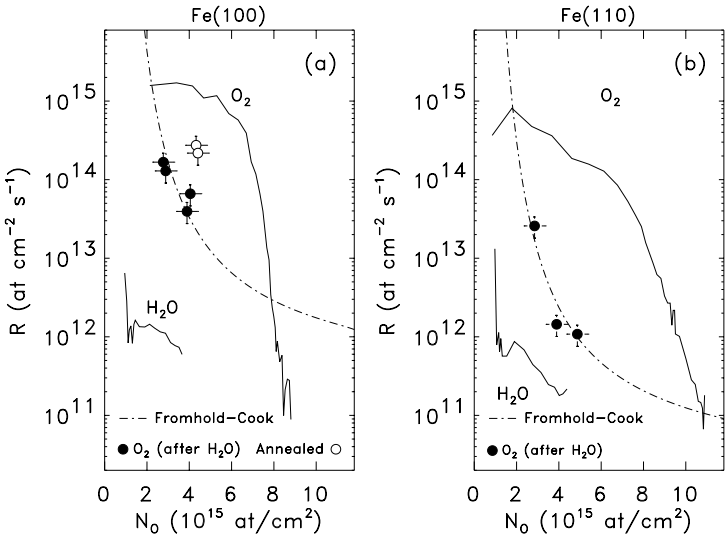

FIGURE 6.8: Oxidation rate vs. oxygen coverage for oxidation in H_2O and O_2 (solid lines). The circles indicate the initial oxidation rate vs. oxygen coverage for O_2 oxidation after pre-oxidation in H_2O. Open circles: after anneal cycle. Dash-dotted line: Fromhold-Cook oxidation mechanism. **(a)** Oxidation of Fe(100). **(b)** Oxidation of Fe(110).

The oxidation rate immediately after exposure to O_2 of the thus prepared sample is plotted in figure 6.8 **(a)** (open circles). This oxidation rate is still significantly lower than that of an equally thick oxide layer without hydrogen, grown in O_2. Therefore, we conclude that the presence of hydrogen in the oxide layer does hinder the cation transport. This is discussed further in section 6.7.3.

The dash-dotted lines in figure 6.8 are explained in section 6.7.3

6.6 Oxidation in H_2O/O_2 Mixtures

In order to gain more insight in the reactions at the surface and/or the transport properties of the oxide layer, we performed oxidation experiments on Fe(100) in O_2/H_2O mixtures (total pressure 2.0×10^{-6} mbar). Figure 6.9 shows the oxygen coverage versus time determined with ellipsometry for these experiments and figure 6.10 shows the oxidation rate versus oxygen

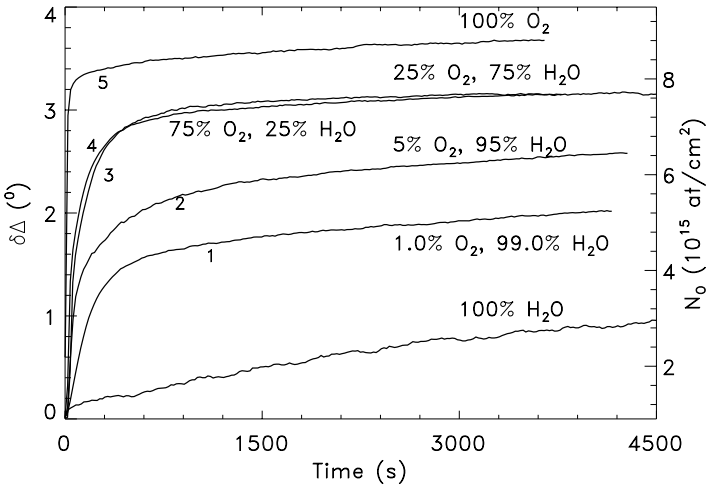

FIGURE 6.9: Ellipsometry curve for Fe(100) at RT in 2×10^{-6} mbar total pressure H_2O/O_2 mixtures. The numbers correspond to the numbers in table 6.1.

coverage obtained from the ellipsometry curves in figure 6.9. In the gas mixtures, the initial oxidation rate (at N_O=1.3×10^{15} atoms/cm^2), as calculated from these curves is directly proportional to the oxygen partial pressure, corresponding to a O_2 sticking probability of 1.0 (indicated with the horizontal lines in figure 6.10). This indicates again the importance of surface processes for the initial oxidation rate. The presence of H_2O vapor in the gas mixture does not influence the oxidation rate at low oxygen coverages.

After approximately 3×10^{15} O atoms/cm^2, the oxidation rate in the mixtures starts to decrease, until saturation is reached. This saturation coverage decreases with increasing H_2O partial pressure. Most probably, the oxidation rate after 3×10^{15} O atoms/cm^2 in the mixtures is limited by the transport of Fe cations through the layer, just as for oxidation in pure O_2 (see chapter 5). To determine the origin of the different oxidation rates and saturation coverages in the different gas mixtures, which may be due to both different H contents and different Fe^{3+} contents, we used XPS and ERD to determine the H content and Fe oxidation state in

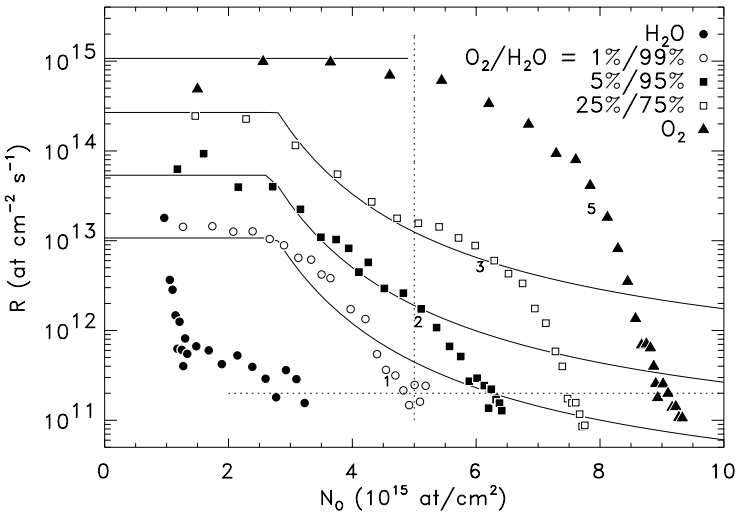

FIGURE 6.10: Oxidation rate vs. oxygen coverages in H_2O/O_2 mixtures. Symbols: experimental data. The solid lines are fits to the Fromhold-Cook oxidation model discussed in the discussion section. The numbers correspond to the numbers in table 6.1. Dotted lines indicate the oxygen coverage and oxidation rate at which XPS (Fe oxidation state) and ERD (H content) measurements were performed.

the oxide layers grown at near saturation ($R = 2 \times 10^{15}$ atoms cm^{-2} s^{-1}) and at N_O=5×10^{15} atoms/cm^2 (indicated in figure 6.10). For all gas mixtures and oxygen coverages measured, the hydrogen content amounted to $N_H = (1.8 \pm 0.2)\times10^{14}$ atoms/cm^2. For the measurements at N_O=5×10^{15} atoms/cm^2, the fraction Fe^{2+} in the layer ($C_{Fe^{2+}}$) decreased with decreasing oxidation rate (and increasing H_2O partial pressure). At near saturation, the highest fraction of Fe^{2+} ($C_{Fe^{2+}}$=0.77) was measured for oxidation in 5% O_2/95%H_2O (curve 2 in figures 6.9 and 6.10). For all experiments, however, the oxidation rate is a monotonously decreasing function of the total amount of Fe^{3+} (in atoms/cm^2, assuming that the Fe^{3+} is distributed homogeneously through the oxide layer). Apparently, the decrease in oxidation rate in O_2/H_2O mixtures is due to the presence of Fe^{3+} in the layer.

Reference measurements with equal O_2 pressures, but no H_2O, revealed

that the saturation coverage is 9×10^{15} O atoms/cm^2, independent of the O_2 pressure. The initial oxidation rates were equal to those obtained in the O_2/H_2O mixtures with the same O_2 partial pressure.

The solid curves in figure 6.10 are fits to the Fromhold-Cook model, which will be discussed in section 6.7.

6.7 Discussion

The aim of this work was to identify a possible oxidation mechanism for the initial room temperature oxidation of Fe(100) in water vapor. It was anticipated that the presence of hydrogen might influence the oxidation kinetics. Summarizing the results, we found that:

1. The oxidation in water vapor proceeds much slower than in oxygen.

2. The oxidation in D_2O is a factor 1.45 ± 0.15 slower than in H_2O on Fe(100). On Fe(110) this factor depends on the coverage, and varies between 1.45 and 2.5 ($N_O > 1.5\times10^{15}$ atoms/cm^2).

3. The oxide layer grown contains hydrogen, which is incorporated after the growth of a first monolayer of oxide. Measurements of the hydrogen content with ERD indicate an average H/O ratio of 0.28 for $N_O > 1.1\times10^{15}$. On Fe(100), XPS measurements revealed the possibility that most of the H present in the sample is linked to the Fe^{3+} in FeOOH. On Fe(110), however, no Fe^{3+} has been found in the oxide, while the H/O ratio does not differ significantly from that measured on Fe(100). This suggests the H incorporation via $Fe(OH)_2$.

4. The oxide formed in H_2O is more passive towards further oxidation in O_2 than an equally thick oxide layer formed in O_2. This is ascribed to the presence of hydrogen and Fe^{3+}.

5. In oxygen/water mixtures, both the initial oxidation rate and the saturation level increase with increasing oxygen partial pressure. The initial oxidation rate is determined by the supply of O_2 molecules. The saturation oxygen coverage is determined by transport properties of the oxide, which are influenced by the presence of Fe^{3+}.

6.7.1 The Composition of the Oxide Layer

Apparently, the oxide layer grown contains OH^- groups, but less than Goethite FeOOH does. The water molecules have to decompose to grow an oxide layer. It is therefore reasonable to assume the presence of adsorbed H and OH at the surface during oxidation. A certain amount of these hydrogen containing groups seems to be incorporated in the oxide during oxidation. This incorporation takes place most probably in the form of OH groups in the oxide, because H atoms are not stable in the oxide. The large irreproducibility of the hydrogen content of different samples may be due to OH being preferentially adsorbed at lattice defects (*e.g.* dislocations) [101] or to a very strong temperature effect.

6.7.2 The Rate-Limiting Step

This irreproducibility in the H-content of the oxide layer contrasts with the good reproducibility of the oxidation rate of Fe(100) at room temperature in H_2O, which suggest that the oxidation rate is not determined by the properties of the oxide layer. Further evidence for the importance of surface processes for the oxidation rate are: **(1)** The oxidation rate in O_2 (after pre-oxidation in H_2O) is much higher than the oxidation rate in H_2O at the same oxygen coverage. **(2)** In the O_2/H_2O mixtures, the initial oxidation rate is determined by the supply of O from O_2 molecules. **(3)** The oxidation rate in D_2O is lower than the oxidation rate in H_2O, although the hydrogen content (OD) and Fe oxidation state are the same. This indicates that H or D are involved in the rate-limiting step, which is presumably the complete dissociation of water at the surface. Debnath *et al* [8] calculated the height of the energy barrier for complete dissociation of H_2O. They found a (theoretical) value of 1.1 eV at FeO and 0.41 eV at clean Fe, which would make dissociation of water molecules at room temperature slow enough to limit the oxidation rate, if pre-exponential factors between 10^{12} and 10^{15} s^{-1} are assumed. Moreover, the process of oxide formation after dissociation has to compete with recombination and desorption.

The lower oxidation rate in D_2O is then due to a lower overall rate constant for the surface processes. Assuming Arrhenius behavior ($k = \nu \exp(-E_{\mathrm{act}}/kT)$) for this rate constant, this may be caused by either a different pre-exponential factor ν or a different activation energy E_{act} or a combination of both. For Fe(100), the ratio plotted in figure 6.6 is close

to $1/\sqrt{2}$ (after the initial fast oxidation where it is difficult to accurately determine this ratio). The factor of $1/\sqrt{2}$ is (in a first order approximation) equal to the ratio of the vibration frequencies for the D and H atoms bound to an oxygen atom (*e.g.* in D_2O/H_2O or OD/OH). This suggests that the difference in oxidation rate is caused by a different pre-factor. On Fe(110), however, the oxidation in D_2O proceeds slower than expected from this simple approximation (resulting in a lower value for the ratio plotted in figure 6.6). Therefore, it is not possible to assign the isotope effect to a different pre-factor solely. In chapter 7, we determine the temperature dependence of the oxidation rate in H_2O and D_2O, which gives more information on the nature of the isotope effect.

The importance of surface processes for the oxidaiton in H_2O contrasts with the oxidation of Fe(100) in O_2, for which we have found in chapter 5 that the initial oxidation of Fe(100) in O_2 can be accurately described with the Fromhold-Cook model, where the transport of electrons and ion cations through the oxide layer determines the oxidation rate. Apparently, the supply of Fe cations and electrons through the oxide layer proceeds faster than the supply of atomic oxygen or OH from the water vapor.

6.7.3 Transport Properties of the Oxide Layer

We will now discuss the transport properties of the oxide layers grown in H_2O and H_2O/O_2 mixtures. Let us first recall that in the case of oxidation in O_2, the oxygen supply from the gas phase is rate-limiting for coverages lower than 4×10^{15} O atoms/cm^2. The presence of hydrogen (OH groups), however, seems to coincide with a decrease of the oxidation rate (figure 6.8 **(a)**). Possible explanations for this are: **(1)** The passivation of lattice defects by hydrogen, resulting in the decrease of the electron current. **(2)** The growth of a more defect free oxide, which has a lower diffusion coefficient for Fe cations. **(3)** Blocking of surface sites by OH groups. As for the first explanation, we know from the calculations in chapter 5 that for layers containing 4×10^{15} O atoms/cm^2, the maximum possible electron current through the oxide layer (without hydrogen) is in the order of 10^{23} cm^{-2}s^{-1}, *i.e.* eight orders of magnitude higher than the oxidation rate observed, ruling out this option. The results in figure 6.8 show a clear dependence of the oxidation rate (in oxygen) on the thickness of the oxide layer pre-grown in water, which contradicts the third possible explanation. In chapter 7, we will show that the OH coverage of the sample during oxidation is low.

Therefore, we suggest the second explanation: for oxidation in O_2 through an oxide layer formed in H_2O, the cation transport is rate-limiting and the decrease of the cation current is (also) due to the presence of hydrogen (oxide containing OH groups). In chapter 5, however, we have shown that the presence of Fe^{3+} also decreases the oxidation rate in oxygen. This was attributed to a decrease of the diffusion coefficient for Fe cations in the oxide. In figure 6.8 **(a)**, we plotted the oxidation curve calculated with the Fromhold-Cook model. For the parameter values we took the ones obtained by fitting the model to oxidation curves in O_2 in chapter 5. To account for the decrease of the diffusion coefficient, we changed the value of W, the thermal activation energy for ionic motion, until agreement with the data was obtained. The resulting value of W amounted to 0.73 eV for Fe(100). The same was done in figure 6.8 **(b)**. The value obtained for W amounted to 0.80 eV on Fe(110). It should be noted that the other parameters for the Fromhold-Cook model were obtained by fitting the oxidation in O_2 of Fe(100). If we change at least the value of χ_0 to the value determined by Leibbrandt *et al* [5,58] ($\chi_0 = 1.32$ eV), the resulting value for W, giving a curve through the data points, amounts to 0.79 eV. In summary, a decrease in the diffusion constant of Fe cations in the oxide coinciding with the presence of hydrogen (OH), modeled by varying the energy barrier for diffusion W in the Fromhold-Cook model, is in agreement with the data in figure 6.10: the hydrogen containing iron oxide forms a passivating layer.

The results for the water/oxygen mixtures are in agreement with the proposed mechanism. For thin oxide layers, the oxidation rate is completely dominated by the oxygen supply from O_2. Apparently, the surface coverage with adsorbed H_2O and dissociation products is low and does not block adsorption and dissociation sites for O_2. Furthermore, the dissociation of adsorbed H_2O molecules proceeds much slower than the dissociation of O_2. For larger H_2O partial pressures and oxygen coverages, the decrease in the oxidation rate is due to the increase of the Fe^{3+} content of the oxide layer.

Since our results on the oxidation in H_2O followed by oxidation in O_2 suggested that the decrease in oxidation rate is due to a lower diffusion coefficient, we tried to fit the FC-model to the data in figure 6.10. We took the parameter values for the oxidation in pure O_2 and varied only W, the thermal activation energy for ionic motion. Furthermore, we assumed the sticking (and dissociation) probability of oxygen molecules to be 1 for all oxygen partial pressures. This sticking probability determines the oxida-

nr	P_{O_2} (mbar)	P_{H_2O} (mbar)	W (eV)	χ_0 (eV)
1	2×10^{-8}	2×10^{-6}	0.82	12.25
2	10^{-7}	1.9×10^{-6}	0.78	8.25
3	5×10^{-7}	1.5×10^{-6}	0.73	5.46
4	1.5×10^{-6}	5×10^{-7}	0.73	5.46
5	10^{-6}-10^{-5}	0	0.64	1.26

TABLE 6.1: Values of the fit parameters for the fits to the FC model (solid lines in figure 6.10)

tion rate for low oxygen coverages. The resulting best fits are plotted in figure 6.10 (solid lines). The fitted values of W are given in table 6.1.

For large oxygen coverages, the calculations yield higher oxidation rates than actually observed. The steep descent, may be due to a decrease in the electron current or a further decrease in the cation current. To discriminate between these, we also varied the parameters χ_0 and χ_L (Metal-oxide work function and oxide-oxygen work function, respectively), keeping $\Delta\chi = \chi_0 - \chi_L$ constant. In the Fromhold-Cook scheme, this means that the electron tunnel current through the layer decreases, keeping the maximum cation current constant. The resulting parameter values are summarized in table 6.1. The fitted values for χ_0 are much higher than the value for oxidation in pure O_2. Already for curve number 3 in table 6.1 and figure 6.10 (where the steep decrease at 7×10^{15} O atoms/cm^2 is undeniable), the fitted value for χ_0 amounts to 5.46 eV. However, the work function of Fe is 4.7 eV [95]. Therefore, we must conclude that the values for χ_0 obtained are unphysical: the decrease of the oxidation rate cannot be explained by a decrease in the electron tunnel current and it is likely that, just as for the oxidation in pure O_2 in chapter 5, also this further decrease of the oxidation is due to the formation of Fe^{3+}.

6.8 Conclusions

In this study, we have obtained the following results:

1. The oxide layer formed at room temperature in water vapor contains hydrogen. The H/O ratio amounts to 0.28±0.02. This hydrogen is

present in the form of OH^-.

2. Oxidation in water vapor proceeds slower than in O_2, probably due to the relatively slow dissociation of water molecules.

3. The hydrogen containing oxide layer formed at room temperature effectively hinders further oxidation in O_2, compared with a hydrogen-free layer containing the same amount of oxygen. This is probably due to less efficient Fe cation transport through the oxide layer grown in water vapor.

4. Annealing the oxide layer formed in H_2O at 473K in vacuum leads to a reduction of Fe^{3+} to Fe^{2+} and a decrease in the hydrogen content. The remaining 2×10^{14} H atoms/cm^2 still decreases the oxidation rate in O_2.

5. The oxidation in O_2/H_2O mixtures could be described with the FC-model. The presence of water vapor in the oxidizing gas leads to the growth of an oxide layer with a lower diffusion constant for Fe cation diffusion, due to the formation of Fe^{3+}.

To obtain more information about the details of the surface processes limiting the oxidation rate of Fe(100) in H_2O, we have performed experiments on the temperature dependence of the oxidation rate. In chapter 7, we will present the results and give a quantitative kinetic model explaining the observed oxidation rates.

Chapter 7

The Temperature and Pressure Dependence of the Oxidation of Fe(100) in H_2O

7.1 Introduction

Knowledge of the H_2O-Fe system is of fundamental importance for the understanding of various aspects of oxidation and corrosion. In the previous chapter, we have shown that the rate of initial oxidation of Fe(100) in H_2O vapor is determined by surface processes. These processes are adsorption, dissociation and ionization within the physisorbed and chemisorbed layer. Furthermore, adsorbed species and dissociation products may recombine and desorb. Finally, it is known that the dissociation of H_2O molecules is facilitated by the presence of steps and edges on the surface [9]. Therefore, the presence of islands of growing oxide may enhance the oxidation rate, leading to a nucleation and growth type of oxidation kinetics.

Most studies on the interaction between H_2O and Fe(100) [96,97,103], Fe(110) and poly-Fe [99,104] have been performed at room temperature or for low exposures. However, a number of important phenomena have been reported to occur in the interaction between H_2O and iron oxides between 300K and 450K, which make a study of the oxidation in this temperature region especially worthwhile: Murray *et al* [101] report an extended H_2O desorption tail up to 600K. Henderson *et al* [102] report water desorption from the recombination of hydroxyl species at 350K or 405K, depending on the nature of the surface reconstruction of α-Fe_2O_3. Hendewerk *et al* [100]

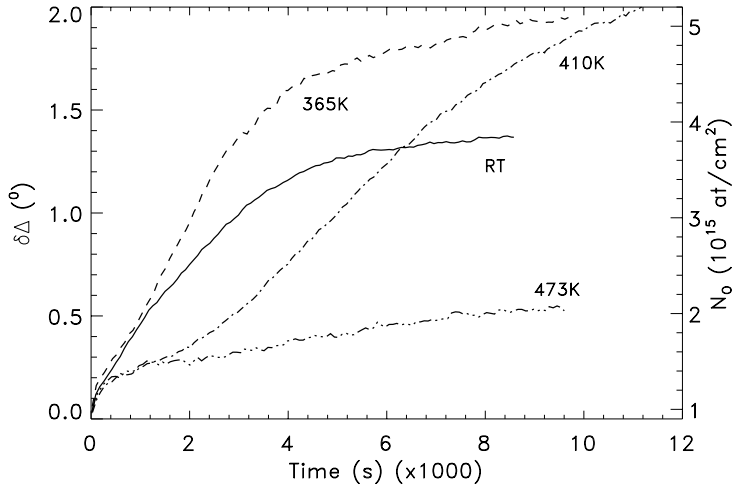

FIGURE 7.1: Ellipsometry curves for Fe(100) exposed to 10^{-5} mbar H_2O at different substrate temperatures.

found H_2 desorption at ∼360K.

Therefore, the study of the temperature dependence of the initial oxidation (rate) in H_2O vapor forms a key ingredient to the identification and quantification of the processes involved. We measured the oxidation rate of Fe(100) in H_2O and D_2O as a function of time, pressure and oxygen coverage using a combination of ellipsometry and ERD. Using a combination of XPS, ERD and ellipsometry, the influence of adsorbed N on the oxidation is determined. Finally, all results are interpreted in terms of a quantitative kinetic model involving the nucleation and growth of oxide islands.

7.2 Temperature Dependence

The oxidation curves ($\delta\Delta$ vs. time) for the oxidation of Fe(100) in 10^{-5} mbar H_2O were measured at temperatures between RT and 473K. The results are shown in figure 7.1. The oxygen coverage was calculated from the measured value of $\delta\Delta$ using the calibration obtained in section 6.3. We found no difference in the calibration curve between oxide layers grown at room temperature and 365K.

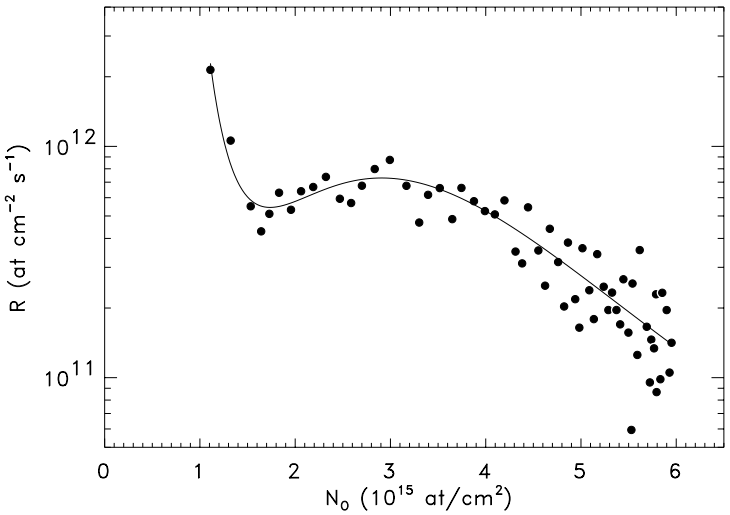

FIGURE 7.2: Oxidation rate vs. oxygen coverage for Fe(100) exposed to 10^{-5} mbar H_2O at 410K. Solid circles: raw data. Solid line: polynomial fit to $\log(R)$ as a function of $\log(N_O)$.

Figure 7.1 shows the oxidation curves at four temperatures. For reasons of clarity, the oxidation curves measured at other temperatures (between RT and 473K) are not shown. All oxidation curves measured follow a general trend. Within 250 s after the start of the H_2O exposure, a change in $\delta\Delta$ is measured, corresponding to the completion of the first monolayer of oxygen ($N_O \simeq 1.3\times10^{15}$ atoms/cm^2). Between 1.3×10^{15} atoms/cm^2 and $\simeq4\times10^{15}$ atoms/cm^2, the oxidation rate first increases with increasing temperature, but decreases again for temperatures exceeding $\sim$350K. At 473K, the oxidation rate for $N_O > 1.3\times10^{15}$ atoms/cm^2 rapidly decreases below 10^{11} atoms cm^{-2} s^{-1}. For $T \leq 410$K, we notice that the saturation coverage (defined as the coverage where the oxygen incorporation rate is lower than 10^{11} atoms cm^{-2} s^{-1}) increases with increasing temperature.

Figure 7.2 shows the oxidation rate vs. oxygen coverage for the oxidation of Fe(100) in H_2O at 410K. The data were obtained by differentiation of the curve in figure 7.1. The line through the data points was obtained by fitting a fourth order polynomial to the logarithm of R as a function of the logarithm of N_O. Similarly, figure 7.3 shows this fitted oxidation rate vs.

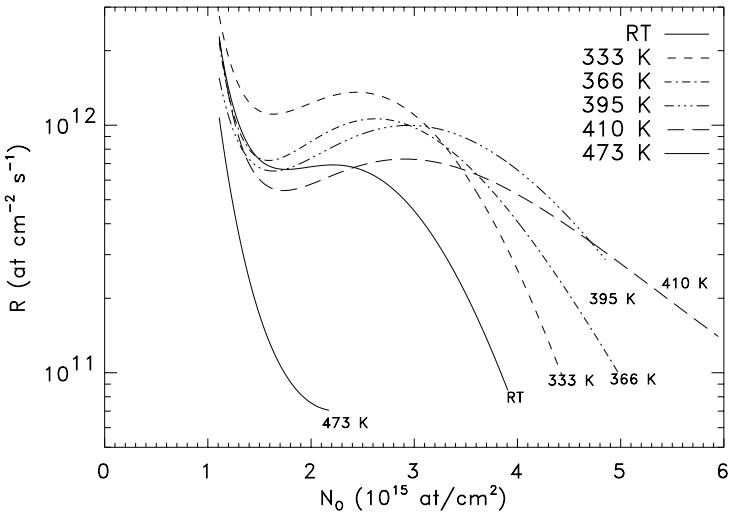

FIGURE 7.3: Oxidation rate vs. oxygen coverage for Fe(100) exposed to 10^{-5} mbar H_2O at different substrate temperatures. The lines shown are fits to the raw data, as described in the text.

oxygen coverage for the oxidation of Fe(100) in H_2O at different temperatures. For $N_O > 1.3\times10^{15}$ atoms/cm^2, the oxidation rate first increases until a maximum is reached, after which the oxidation rate quickly decreases. Also in the oxidation curves in figure 7.1 this is apparent, especially in that at 410K (*S*-shaped curve). *S*-shaped curves (and rate-thickness plots where the oxidation rate does not decrease monotonously) are usually interpreted as indications of a nucleation and growth process.

From the raw data as given in figure 7.2, we determined $R_{\max}$, the maximum oxidation rate (for $N_O > 1.5\times10^{15}$ atoms/cm^2), which is plotted in figure 7.4 **(a)**.

Figure 7.4 **(a)** suggests the presence of two temperature regimes: For low temperatures, the maximum oxidation rate increases with increasing temperature. For temperatures above a transition temperature T_{trans}, $R_{\max}$ decreases with increasing T. A possible explanation for this is that the oxidation rate is determined, among others, by the surface coverage of adsorbed H_2O (or, possibly, OH). At low temperatures, a maximum coverage of H_2O or OH is reached and the increase in oxidation rate is due to a

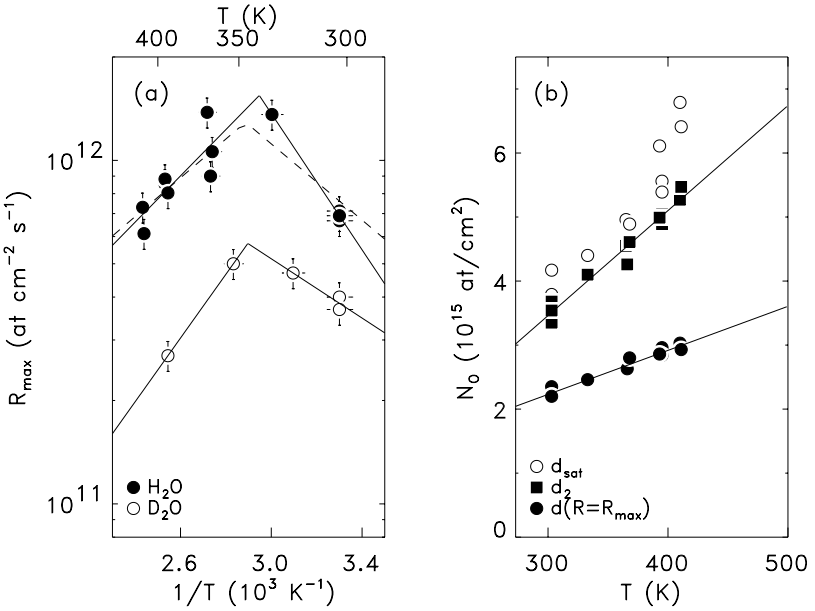

FIGURE 7.4: **(a)** Arrhenius plot of the maximum oxidation rate (for $N_O > 1.5\times10^{15}$ atoms/cm^2) for the oxidation of Fe(100) in 10^{-5} mbar H_2O (closed symbols) and D_2O (open symbols). The solid lines indicate Arrhenius behavior (table 7.1). Dashed line: calculation using the rate equations model described in section 7.5.2, using the parameter values of table 7.4. **(b)** d_{max} (solid circles), saturation coverage d_{sat} (open circles) and d_2 (solid squares, $R = 2 \times 10^{11}$ atoms cm^{-2} s^{-1}) vs. temperature. The solid lines are linear fits through the data points.

pre-exponential factor (at cm^{-2} s^{-1})	apparent activation energy (eV)	Regime
(1.3±0.2)×10^{15}	0.20±0.04	$T < T_{trans}$
(2±3)×10^{10}	-0.13±0.04	$T > T_{trans}$

TABLE 7.1: Apparent Arrhenius parameters for Fe(100) in H_2O, obtained from figure 7.4 **(a)**

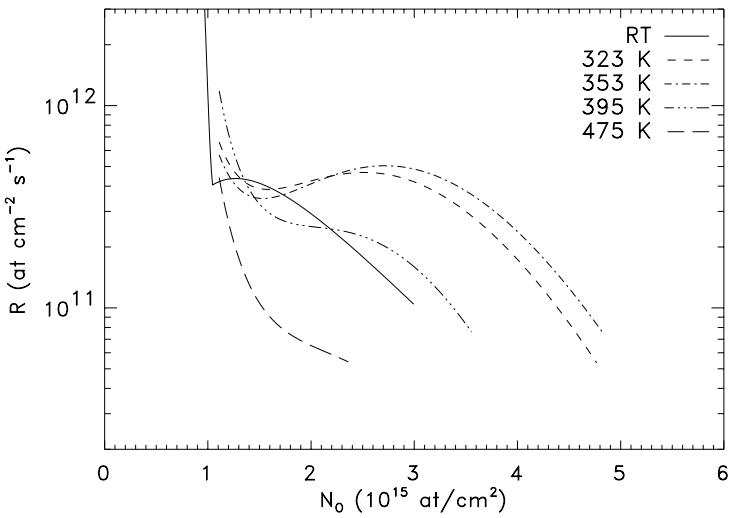

FIGURE 7.5: Oxidation rate vs. oxygen coverage for Fe(100) exposed to 10^{-5} mbar D_2O at different substrate temperatures. The lines shown are fits to the raw data, as described in the text.

faster dissociation and/or surface diffusion with increasing T. A different explanation involves the H_2 desorption rate which rapidly increases at T_{trans} and determines the oxidation rate at lower T. Above T_{trans}, the coverage of adsorbed species rapidly decreases due to recombination and desorption, leading to a decrease of R_{max}. This will be discussed further in section 7.5.1. All possible rate limiting steps (desorption, dissociation, formation of nuclei, recombination) can be described in first approximation with Arrhenius behavior [105–108]. Therefore, from the Arrhenius plot in figure 7.4 **(a)**, apparent Arrhenius parameters are obtained by fitting straight lines through the data points. The results are summarized in table 7.1. The value of the transition temperature T_{trans} is (340±6)K.

Figure 7.4 **(a)** also shows the maximum oxidation rate of Fe(100) in D_2O for different temperatures. For these experiments, the oxidation rate vs. oxygen coverage is plotted in figure 7.5. The maximum oxidation rate in D_2O shows roughly the same behavior as in H_2O. The oxidation rates in D_2O are lower, while the transition is found at T_{trans}=345K. The apparent activation energies differ from those found in the temperature dependence

of the oxidation in H_2O.

From the data as given in figure 7.2 for the oxidation of Fe(100) in H_2O, we also determined the oxygen coverage $d_{\max}$ at which the maximum oxidation rate is reached, and the coverages d_{sat} and d_2 at which the oxidation rate equals 10^{11} atoms cm^{-2} s^{-1} and 2×10^{11} atoms cm^{-2} s^{-1}, respectively. The values for $d_{\max}$, d_{sat} and d_2 for the oxidation in H_2O, plotted in figure 7.4 **(b)**, increase with increasing temperature. For the measurement at 473K, there was no value for $d_{\max}$, so we did not use this measurement. Linear fits through the data (solid lines in the figure) intersect at $T = 171$K and N_O=1.34×10^{15} atoms/cm^2. This oxygen coverage is in the range of one monolayer (and partly invisible with ellipsometry), suggesting that for $T < 170$K the nucleation and growth process does not start and only a first monolayer of oxygen forms. Above this temperature, oxidation after the first monolayer proceeds via the nucleation and growth of oxide islands. The average island thickness (as probed by the saturation coverage) increases with increasing temperature.

To obtain a better understanding of the processes and activation energies involved, a quantitative model should be fitted to the oxidation rate vs. oxygen coverage and its temperature dependence. This is done in section 7.5.

7.3 The Influence of N on the Initial Oxidation of Fe(100) in H_2O

In chapter 4, a nitrogen marker layer was used to determine the moving species during the oxidation of Fe(110) in O_2. For that purpose, it was established that first the N marker layer (nitrogen coverage about 1 ML) does not influence the oxidation rate. Then, by measuring the evolution of the N(1s) XPS peak as a function of oxygen coverage, the position of N in the surface region of the sample was determined.

The aim of this section is similar. By measuring the influence of preadsorbed N on the oxidation rate and the position of the N in the surface region of the sample, information is obtained about the moving species during oxidation and the oxidation mechanism. To obtain measurable attenuation of the N(1s) XPS signal, the oxygen coverage of the layer grown must be larger than 2×10^{15} O atoms/cm^2 and the N peak has to be measured over a considerable range of oxygen coverages. Therefore, these experiments are

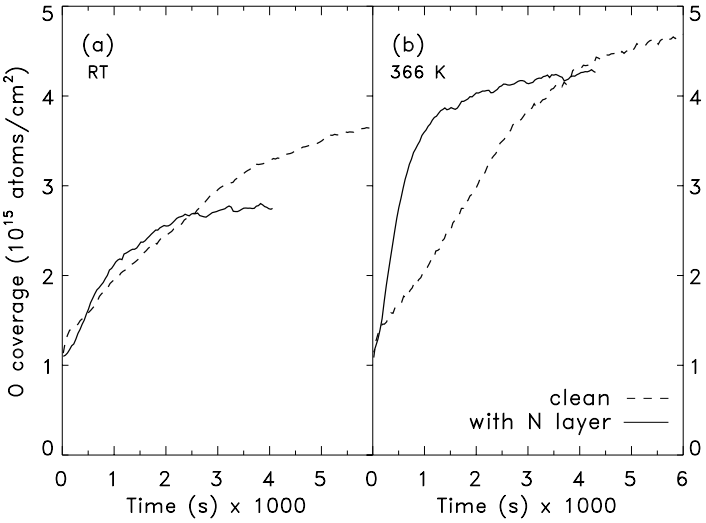

FIGURE 7.6: Ellipsometry measurements of oxidation in 10^{-5} mbar H_2O at room temperature and at 365K of clean Fe(100) and Fe(100) covered with 1 ML nitrogen.

carried out at 365K.

The deposition of the N layer was done as described in section 4.4.1.

7.3.1 The Influence of N on the Initial Oxidation

Figure 7.6 shows the oxidation curves measured with ellipsometry for both clean Fe(100) and Fe(100) covered with nitrogen. The values for N_O on the vertical axis of figure 7.6 were calculated with the calibration curve for $\delta\Delta$ obtained in section 6.3. We found no significant differences between the values of N_O measured with ERD and those calculated from the value of $\delta\Delta$. In contrast with the observations for the initial oxidation of iron in O_2 (section 4.4), there is a remarkable difference in the oxidation kinetics between clean and N pre-covered Fe(100), indicating that processes at the surface play a much more important role here than in the oxidation in O_2 (see section 4.4.2).

Figure 7.7 shows the oxygen incorporation rate vs. oxygen coverage obtained from the ellipsometry curves in figure 7.6. For the N pre-adsorbed

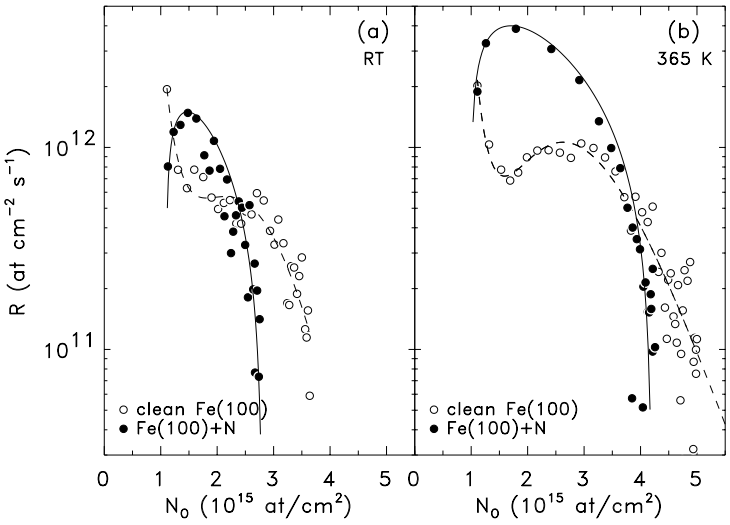

FIGURE 7.7: Oxidation rate vs. oxygen coverage obtained from the ellipsometry curves in figure 7.6. Solid circles: Fe(100) with pre-adsorbed N. Open circles: clean Fe(100). The lines are drawn to guide the eye. **(a)** Room temperature. **(b)** T=365K.

Fe(100), these curves still show a nucleation and growth type of oxidation mechanism (the oxidation rate increases with increasing coverage, reaches a maximum and then starts to decrease again). The initial fast regime for $N_O < 1.3\times10^{15}$ atoms/cm^2, which is always present for the oxidation of clean Fe(100) in H_2O, is not present for the oxidation of N pre-covered Fe(100). Furthermore, the maximum oxidation rate is a factor of 2.6 (RT) to 4.0 (365K) higher than in the case of clean Fe(100). Finally, the oxidation rate starts to decrease at smaller oxygen coverages and the final oxide thickness reached is lower in the case of the N pre-covered Fe(100).

7.3.2 The Depth of the N Layer

To measure the position of the deposited N after oxidation, oxide layers of different thicknesses were prepared by oxidizing N pre-covered Fe(100) at 365K in 10^{-5} mbar H_2O. After the oxidation, the N(1s) XPS spectrum was taken and the coverages of N and O were measured with ERD, using a

N_O (10^{15}atoms/cm^2)	N_N (10^{15}atoms/cm^2)	Y_{N1s} (a.u.)
0.71±0.05	1.07±0.06	161±9
2.15±0.08	0.88±0.05	125±9
4.50±0.11	0.75±0.05	95±9

TABLE 7.2: Oxygen and nitrogen coverages determined with ERD and N(1s) yields measured with XPS for Fe(100) oxidized at 365K in 10^{-5} mbar H_2O.

35 MeV Cl beam. The N(1s) yield was determined from the XPS spectrum as described in section 4.4.3. The data thus obtained are summarized in table 7.2

The nitrogen coverage, which was about 1 ML initially, decreased as the oxidation proceeded. During the oxidation of iron in O_2 at room temperature, the nitrogen coverage remained constant. To check whether N also disappears in O_2 at 365K, reference measurements were done. During the oxidation of Fe(100) in O_2, the amount of nitrogen decreased from $(1.48\pm0.07)\times10^{15}$ atoms/cm^2 before oxidation to $(0.80\pm0.05)\times10^{15}$ atoms/cm^2 (at 11.6×10^{15} O atoms/cm^2). So, nitrogen also disappears upon exposure to oxygen at elevated temperatures. Possible explanations for this are:

1. The formation of gases like N_2, N_2O, NO or NO_2 from co-adsorbed N and O. From a thermodynamical point of view, the formation of molecular nitrogen gas is most likely to occur. For the reaction between O_2 and γ'-Fe_4N_{1-x}, it was found experimentally, however, that the reaction products are ϵ-Fe_2N_{1-y} and Fe_3O_4 [109]. In section 4.4.3 of this thesis we mentioned the possibility that nitride clusters are formed during the annealing step before oxidation. Although the kinetic pathway for the formation of the above-mentioned gases is probably blocked after the formation of at least 1 ML of oxide, the formation of nitrogen containing gases is still possible if nitride clusters are present.

2. Diffusion of N into the bulk of the sample. During annealing at 700K, the remaining monolayer of N did not diffuse into the bulk (see section 4.4.1). The formation of oxide may sufficiently lower the

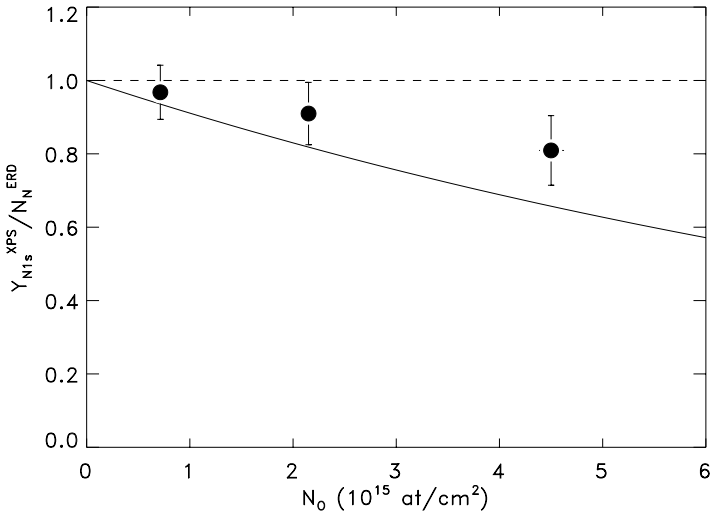

FIGURE 7.8: Relative XPS yield (XPS yield divided by the amount of N determined with ERD) vs. oxygen coverage for Fe(100) oxidized in H_2O at T=365K. Dashed line: N remains at surface. Solid line: N remains at the iron/oxide interface under a flat oxide layer.

kinetic barrier preventing the remaining monolayer of N to diffuse into the bulk.

A careful theoretical and experimental analysis is needed to decide between the alternatives.

Figure 7.8 shows the N(1s) yield divided by the N coverage determined with ERD. The oxygen coverages on the horizontal axis were also determined with ERD. The XPS O(1s) and Fe(2p) yields were within the accuracy equal to the expected values (using the values of the AL determined in chapter 3). Figure 7.8 shows that after correction for the N loss during the oxidation, the N(1s) yield decreases more slowly than expected when N is at the oxide/metal interface.

We attempted to fit the data points in figure 7.8 with simple models for the attenuation of the N signal if the sample is covered with oxide clusters. Using equation (B.20) in appendix B, we were able calculate the relative island coverage and thus the expected N(1s) XPS signal, for two- and three-dimensional growth and intermediate cases, assuming Fe as the

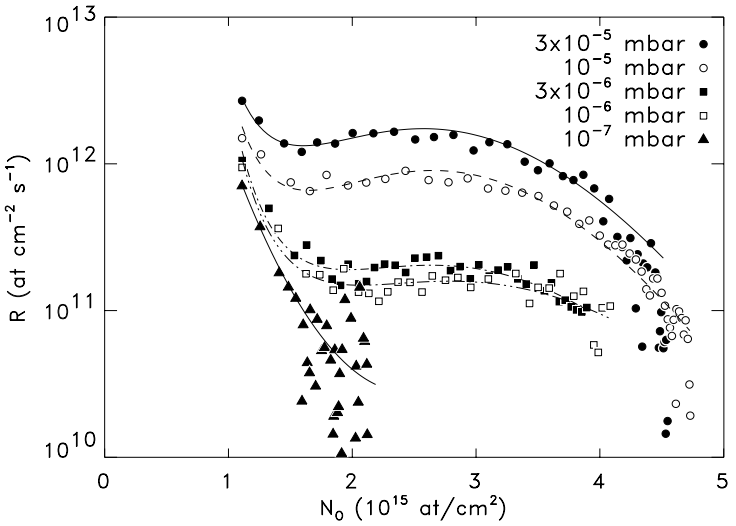

FIGURE 7.9: Oxidation rate vs. oxygen coverage for Fe(100)+H_2O at 365K, for different H_2O pressures.

moving species. With realistic parameter values, we could not fit the data in figure 7.8. Therefore, we conclude that the deviation from the solid line in figure 7.8 is due to (apparent) mobility of oxygen during the oxidation process. Just as in section 4.4.3, this may be due to the formation of nitrogen clusters or to the nucleation and growth process leading to an apparent O mobility.

7.4 Pressure Dependence

Figure 7.9 shows the oxidation rate of Fe(100) exposed to H_2O as a function of oxygen coverage, obtained from the oxidation curves measured with ellipsometry, for the oxidation of Fe(100) at 365K in H_2O, for pressures ranging from 10^{-7} mbar to 3×10^{-5} mbar. The maximum oxygen incorporation rate (after completion of the first monolayer) increases with increasing pressure. The oxygen coverage at which $R_{\max}$ is reached is approximately constant over the whole pressure range. For p=10^{-7} mbar, the oxidation proceeded so slowly that this coverage was not reached during the experiment and we could not determine $R_{\max}$ at this pressure. In the same way, the pressure

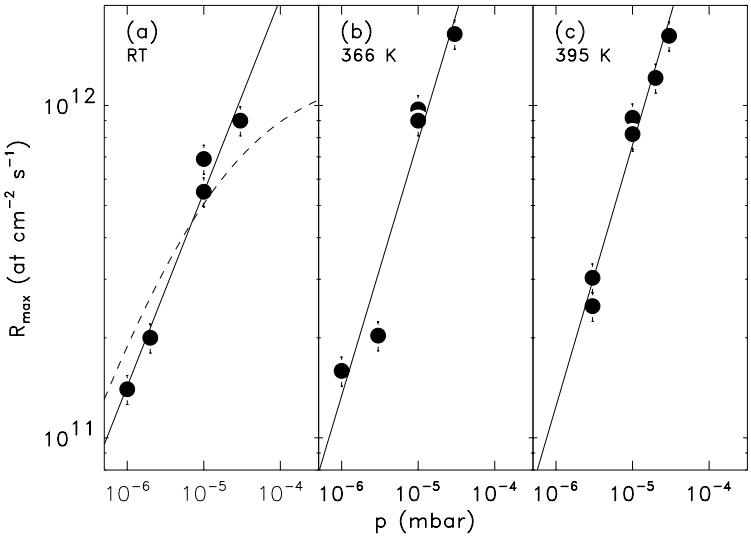

FIGURE 7.10: Maximum oxidation rate vs. H_2O pressure at **(a)** RT, **(b)** 365K and **(c)** 395K. The solid lines are fits to equation (7.1). The dashed line in **(a)** is described in section 7.5.2.

dependence at room temperature and 395K was measured. Also at these temperatures, the shape of the curves (oxidation rate vs. oxygen coverage) remains roughly the same, indicating that the oxidation mechanism does not change as the pressure changes.

In figure 7.10, $R_{\max}$ is plotted against the H_2O pressure. A power law dependence is fitted to the data, according to:

$$R_{\max} = Ap^{\gamma} \tag{7.1}$$

with γ and A constant. At 365K and 395K, γ amounted to 0.77±0.06. At room temperature, γ amounted to 0.57±0.08.

7.5 Discussion

7.5.1 Surface Processes

In chapter 6 we have shown that the oxidation rate of Fe(100) in H_2O is governed by the rates of surface reactions. In the previous sections of

this chapter, we have observed a reaction probability which increases with increasing oxygen coverage, and then decreases again: we have attributed this to the growth and coalescence of oxide clusters. These processes start after the formation of the first monolayer of chemisorbed oxygen.

The formation of the first monolayer of oxygen proceeds very fast and with our ellipsometry measurements, we are only sensitive in the region of completion of the first monolayer. Therefore, in our discussion we will focus on the oxidation process after the first monolayer and consider only processes at an oxide (or oxygen covered) surface. In our discussion, we assume that there is no difference in the adsorption/desorption and dissociation behavior between the oxide surface (*i.e.* on the islands) and the monolayer of (chemisorbed) oxygen (between the islands).

For the oxidation reaction observed, the H_2O molecules have to dissociate completely, probably at the edges of oxide islands. For this complete dissociation, there are two possible mechanisms: **(1)** H_2O molecules arriving at the surface dissociate easily into OH and H and the nucleation and growth behavior is governed by the rate of dissociation of OH. **(2)** H_2O molecules only dissociate completely at island edges. In order to distinguish between these two we have to consider that the desorption temperature of H_2O is between 160K and 260K on α-Fe_2O_3, depending on the surface orientation, reconstruction and H_2O dose [100–102]. This implies that at the temperatures of our measurements, the desorption of H_2O molecules is fast and the maximum coverage of adsorbed H_2O at the surface (assuming equilibrium between adsorption and desorption and no other reaction channels) should depend linearly on the H_2O pressure. Furthermore, the presence of OH at the surface of Fe_2O_3 exposed to H_2O at 225K [102] and at oxygen deficient Fe_2O_3 up to 320K [100] shows that even at low temperatures H_2O adsorbs dissociatively. Also on clean iron, H_2O molecules adsorb dissociatively, with dissociation products OH and H [96,97]. Therefore, we conclude that the growth of oxide islands proceeds by the dissociation of hydroxyl species (OH) at the edges of oxide islands.

In figure 7.4 **(a)**, we found a change in the apparent activation energy of the maximum oxidation rate at T=340K. Again, we may consider two underlying reactions which can explain this transition, *i.e.* H_2 formation followed by desorption or recombination of H+OH followed by H_2O desorption. At approximately 340K, hydrogen recombination followed by desorption ($2H_a \rightarrow H_2 \uparrow$) occurs as found by Hendewerk *et al* [100] on

α-Fe_2O_3 and by Rezaie-Serej and Outlaw [110] on stainless steel (which is covered with a thin iron oxide layer). But also H_2O desorption was found at similar temperatures, due to the recombination of OH and H (dissociation products of H_2O) [101,102]. We believe that the transition is due to H_2 desorption, as follows from the following reasoning:

If the transition in apparent activation energy at T_{trans} were due to the recombination of adsorbed H and OH, the pressure independent saturation coverages of H and OH would be reached below the transition temperature, assuming that H_2O completely dissociates and the oxidation rate does not influence the balance of adsorbed species at the surface, which is reasonable regarding the low oxidation rates of about 10^{-3} monolayers/s. Then we would have $\gamma = 0$ for the pressure dependence at temperatures below the transition. Furthermore, hydrogen desorption must be possible for the oxidation to proceed (otherwise the oxidation would stop after the formation of less than one monolayer), so if hydrogen desorption is slow at low temperatures it limits the oxidation rate. Above T_{trans}, the temperature dependence is determined by a combination of the adsorption/desorption equilibrium of H_2O and the desorption of H_2, and influenced by diffusion and dissociation of OH. Therefore, we conclude that the transition at $T = 340$K is probably due to the desorption of H_2, in agreement with the results of Hendewerk *et al* [100] on Fe_2O_3.

7.5.2 Nucleation and Growth Model

Assumptions, Reactions and Parameters

By a more detailed evaluation of the different possible surface reactions and rate constants and comparison with the data, the relative importance of the different steps can be deduced. Summarizing the previous section, the following surface reactions occur if an iron oxide or clean iron surface is exposed to H_2O vapor:

$$H_2O_a \rightleftharpoons H_2O_g \tag{7.2}$$

$$H_2O_a \rightleftharpoons OH_a + H_a \tag{7.3}$$

$$2H_a \rightarrow H_2 \uparrow \tag{7.4}$$

Reaction (7.2) represents the adsorption and desorption of gas molecules. The adsorption rate is proportional to the H_2O vapor flux, which is proportional to the H_2O pressure according to $\Phi M = p_{H_2O}/\sqrt{2\pi m k_B T_{\text{vapor}}}$,

assuming a sticking coefficient of 1. Here, Φ is the arrival rate in monolayers per second, M is the oxygen coverage corresponding to one monolayer ($M \approx 1.3\times10^{15}$ O atoms/cm^2), m is the mass of the H_2O molecules and k_B is the Boltzmann constant. The desorption rate is characterized by its rate constant k_1.

Reaction (7.3) represents the dissociation of H_2O molecules (with rate constant k_2) and the recombination of adsorbed OH and H forming H_2O (rate constant k_2'). Finally, the formation and subsequent desorption of H_2 molecules from adsorbed H atoms is represented by reaction (7.4) with rate constant k_3.

In the absence of oxidation, these reactions determine the balance of the surface species H, OH and H_2O. In our case, there is oxidation (by the dissociation of OH), so we have to take into account the oxide forming reactions.

If adsorbed hydroxyl (OH) dissociates, atomic oxygen is formed. In chapter 6, we have shown that the reaction between O_2 and Fe is limited entirely by the arrival rate of oxygen. Therefore, we assume that dissociation of OH leads to instantaneous oxide formation. The nucleation and growth kinetics observed indicate that edges of oxide islands play an important role in the dissociation of OH. We propose the following reactions:

$$\mathrm{OH}_a + \mathrm{Fe} + \mathrm{edge} \rightarrow \mathrm{FeO} + \mathrm{H}_a + \mathrm{edge} \tag{7.5}$$

$$2\mathrm{OH}_a + \mathrm{Fe} \rightarrow \mathrm{FeO} + \mathrm{edge} + \mathrm{H_2O}_a \tag{7.6}$$

Reaction (7.5) represents the growth of an existing oxide island by dissociation of OH at an edge site. Reaction (7.6) represents the formation of a new oxide nucleus. Similar reactions are proposed in the literature [98–102]. Rate constants for these reactions (7.5) and (7.6) are k_4 and k_5, respectively. The value of k_4 depends on the density of edge sites, the arrival rate of OH at an edge site and the probability of dissociation when OH arrives at the edge site. Therefore, k_4 is a function of the surface diffusion constant D and the cross section for island growth σ_g. Similarly, k_5 depends on D and σ_n, the cross section for dissociation if two OH groups arrive at neighboring sites (nucleation cross section). A summary of the proposed reactions and rate equations is given in table 7.3.

All processes are assumed to be thermally activated, so we used Arrhenius descriptions for the rate constants. The rate constants k_1, k_2, k_2'

Reaction	rate constant	comment
Adsorption of H_2O_a (7.2)	Φ	arrival rate from gas
Desorption of H_2O_a (7.2)	k_1	
H_2O dissociation (7.3)	k_2	
H_2O recombination (7.3)	k_2'	reverse reaction
H_2 desorption (7.4)	k_3	
OH dissociation at edge (7.5)	k_4	depends on edge site density
Nucleation (7.6)	k_5	

TABLE 7.3: Reactions and rate constants for the surface reactions considered.

and k_3 are given by $k_i = \nu_i \exp(-E_i/k_BT)$ with ν_i the pre-exponential factor ('attempt frequency') and E_i the activation energy for the reaction. The diffusion constant D is given by $D = \nu_d a^2 \exp(-E_d/k_BT)$ with a the lattice constant, which is related to the monolayer coverage M via $a^2 = 1/M$. The cross sections for nucleation and growth are given by $\sigma_n = \sigma_{n,0} \exp(-E_n/k_BT)$ and $\sigma_g = \sigma_{g,0} \exp(-E_g/k_BT)$, respectively.

Using these rate constants, rate equations for the presumed chemical reactions taking place at the surface are solved (or approximated solutions obtained in quasi-equilibrium). In this way, the surface coverages of H_2O, OH and H and the oxidation rate are obtained. The calculations can be found in appendix B. For the rate equations describing the nucleation and growth of oxide islands, the approach by Venables [111–114] is used. The assumptions made for the derivation of the nucleation and growth curves and the calculation of the pressure dependence of the oxidation rate are:

1. The incorporation of H in the oxide is not considered as a channel for loss of adsorbed H atoms. Also hydrogen disappearing into the bulk of the sample is not accounted for. This may influence the coverage of adsorbed H or OH (if the hydrogen incorporation proceeds via H or OH, respectively) and lead to deviations from the predicted oxidation rate ignoring the incorporation of hydrogen.

2. Direct desorption of OH is not taken into account. This desorption of OH has never been observed experimentally, which is in agreement with the expected high binding energy of OH at the surface.

3. The direct reaction between H_2O and Fe (H_2O+Fe $\rightarrow$ FeO+H_2 in one step) is not taken into account (see the discussion in section 7.5.1).

4. H, OH and H_2O adsorb at separate lattices. H_2O is physisorbed, and the mean distance from the sample is larger than that of the chemisorbed H and OH. Adsorbed OH acts as a Lewis acid and prefers to stay at anionic sites [9]. Following the same line of reasoning, we expect adsorbed H to be an electron donor which prefers the cationic sites. Because it turns out that the coverages with H_2O, OH and H are very low, a different assumption on the nature of the adsorption sites would lead to approximately the same oxidation rate and pressure dependence.

5. We assume steady-state behavior *i.e.* the (quasi-)equilibrium coverages of H_2O, OH and H have been reached on a time scale much shorter than that of oxidation.

6. The dissociation of OH takes place at the edge sites of oxide islands, or by the formation of a new nucleus by $2OH + Fe \rightarrow FeO + H_2O$.

7. The formation of new nuclei is only possible between existing islands.

8. We assume the oxide islands to be circular and randomly placed.

9. We consider only one "mean" island size, instead of a more realistic size distribution.

Important parameters in the description are the total areal density of oxygen contained in the islands V, the value of V at saturation $V_{\max}$, the fractional island coverage θ and the island density N. The island shape is described by the dimensionless parameters α and β. The value of α determines the growth mode, which can vary from two-dimensional growth of islands with a constant thickness ($\alpha = 0$) to three-dimensional growth of islands with a constant shape ($\alpha = 1/2$) and intermediate cases. The different symbols are listed in table B.1 in appendix B.

Temperature Dependence

In figure 7.4 **(a)**, we determined the apparent activation energies for the maximum oxidation rate, which are given in table 7.1. From expressions (B.23) and (B.26) in appendix B, it follows that this apparent activation

energy can be expressed in terms of the activation energies of the underlying processes as collected in table 7.4. For E_{A1} (low temperature, equation (B.23)) and E_{A2} (high temperature, equation (B.26)) we find:

$$\begin{aligned} E_{A1} &= \frac{2}{3}E_g + \frac{1}{3}E_n + E_d + \frac{1}{3}E_V + \frac{2}{3}E_2 - \frac{2}{3}E_2' - \frac{2}{3}E_1 \\ E_{A2} &= \frac{2}{5}E_g + \frac{1}{5}E_n + \frac{3}{5}E_d + \frac{1}{5}E_V + \frac{4}{5}E_2 - \frac{4}{5}E_2' - \frac{4}{5}E_1 + \frac{2}{5}E_3 \end{aligned} \tag{7.7}$$

Here, E_V is the apparent activation energy for the increase of $V_{\max}$ with temperature. Although we concluded in section 7.2 that d_{sat} (and, consequently, $V_{\max}$) increases linearly with temperature, a fit to Arrhenius behavior gave reasonable results which can be used to calculate the apparent activation energies. E_V then amounted to 0.064 eV.

Noting that both equations in (7.7) are linear combinations of $(E_2 - E_2' - E_1)$, $(2E_g + E_n + 3E_d + E_V)$ and E_3, we have a system of two equations and three independent parameters. Hendewerk *et al* [102] report a broad H_2 desorption TPD peak at $T = 360$K on α-$Fe_2O_3(100)$. Assuming a pre-exponential factor of 10^{13} s^{-1}, this gives $E_3 = 0.93$ eV. Now, we can solve equations (7.7). With $E_{A1} = 0.2$ eV and $E_{A2} = -0.13$ eV from table 7.1, we obtain:

$$\begin{aligned} 2E_g + E_n + 3E_d &= 3.65 \text{ eV} \\ E_2 - E_2' - E_1 &= -1.56 \text{ eV} \end{aligned}$$

From the H_2O desorption peak at $T = 180$K observed on α-$Fe_2O_3(100)$ [100] and at $T = 175$K on an iron oxide surface containing both Fe^{2+} and Fe^{3+} [101], we deduce that the value of E_1 lies between 0.4 eV and 0.6 eV. This is close to the sublimation energy of ice (0.53 eV). Therefore, we will take this value for E_1. We then obtain $E_2 - E_2' = -1.03$ eV. Typical values for the hopping barrier for surface diffusion (E_d) are around 0.1 eV. Taking this, we obtain: $2E_g + E_n = 3.35$ eV. For surface processes, activation energies are typically in the range 0-2 eV, so our values are reasonable.

To obtain further agreement between the measurements and the model, we also need to predict the maximum oxidation rates observed and the transition temperature. These are determined by the values of the rate constants, the diffusion constant and the cross sections for nucleation and growth. If we assume that the pre-exponential factors are in the range between 10^{11} s^{-1} and 10^{19} s^{-1} [106], we have to take slightly different

Parameter	Value	Comment
$\sigma_{n,0}$	1	pre-exponential factor for nucleation cross section
$\sigma_{g,0}$	1	pre-exponential factor for growth cross section
E_n (eV)	1.08	Activation energy for nucleation
E_g (eV)	0.85	Activation energy for growth of oxide island
ν_1 (s^{-1})	10^{17}	Attempt frequency for k_1
E_1 (eV)	0.53	Activation energy for k_1 ($k_1 = \nu_1 \exp[-E_1/k_BT]$)
ν_2 (s^{-1})	10^{12}	Attempt frequency for k_2
E_2 (eV)	0.4	Activation energy for k_2
ν_2' (s^{-1})	3.5×10^{17}	Attempt frequency for k_2'
E_2' (eV)	1.245	Activation energy for k_2'
ν_3 (s^{-1})	4×10^{12}	Attempt frequency for k_3
E_3 (eV)	0.93	Activation energy for k_3
ν_d (s^{-1})	10^{13}	Attempt frequency for diffusion of OH
E_d (eV)	0.1	Activation energy for diffusion
M ($/cm^2$)	1.3×10^{15}	Monolayer coverage
Φ (ML/s)	2.38	H_2O arrival rate ($p = 10^{-5}$ mbar, sticking=1)
N_i ($/cm^2$)	0	Island density at $\theta = 0$

TABLE 7.4: Parameter values used for the calculation of the curves in figures 7.4 **(a)** and B.2. The rate constants k_i are given by $k_i = \nu_i \exp(-E_i/k_BT)$ and the diffusion constant D is given by $D = \nu_d a^2 \exp(-E_d/k_BT)$ with $a^2 = 1/M$. The cross sections for nucleation and growth are given by $\sigma_n = \sigma_{n,0} \exp(-E_n/k_BT)$ and $\sigma_g = \sigma_{g,0} \exp(-E_g/k_BT)$, respectively.

values for the activation energies than mentioned above. For the parameter values summarized in table 7.4, the calculated maximum oxidation rate is plotted in figure 7.4 **(a)** (dashed line). As can be seen from the figure, the agreement between model and measurement is good. Also, the OH and H coverages calculated (with the approximations (B.12) and (B.15)) are well below 1 at the appropriate temperatures. The relatively high values for the attempt frequencies ν_2' and ν_1 are associated with a high entropy of the transition state (high ratio of the total partition functions of the activated complex and adsorbed particles) [106,115]. The parameter values of table 7.4 are chosen such that they correspond to a H_2O desorption TPD peak at 157K, a H_2 desorption peak at 370K and a desorption peak due to the recombination of OH and H and subsequent H_2O desorption at 360K, *i.e.* they are in agreement with values from TPD experiments on

iron oxides exposed to H_2O vapor [100–102]. Dissociation of H_2O into H and OH is possible for temperatures above 170K. This is in agreement with the value of $T = 171$K in section 7.2 obtained from the extrapolation of the temperature dependence of $d_{\max}$ and d_2. The maximum island density calculated with this parameter set varies between 10^{11} cm^{-2} (400K) and $4{\times}10^{12}$ cm^{-2} (308K) for all values of α.

In this discussion, we have assumed that N_i, the density of nuclei at $\theta = 0$, equaled zero in our experiments. The possible presence of nucleation sites and its temperature dependence can also influence the oxidation rate and the apparent activation energy. To influence the oxidation rate, the values of N_i must be in the order of the maximum island density calculated if $N_i = 0$ is assumed (10^{11} cm^{-2} to $4{\times}10^{12}$ cm^{-2} for the parameter values of table 7.4). These defect densities are realistic. However, we do not need a non-zero N_i to successfully describe the observations. Direct measurement of the island densities (using microscopic methods such as *in-situ* STM or *in-situ* AFM) is necessary to obtain information about defect densities and a more accurate determination of the different activation energies.

Pressure Dependence

The solutions of the rate equations (given in appendix B for the assumptions given above) can be used to calculate the pressure dependence of the maximum oxidation rate (experimental results in section 7.4). There are several possible (limiting) cases in which one or several reaction steps can be ignored. Furthermore, depending on the island density, the oxide formation may be dominated by either the formation of new islands ('nucleation') or the growth of existing islands ('growth'). For the parameter values given above (and other parameter values where $\sigma_n \leq \sigma_g$), the oxidation rate is already dominated by growth at very low coverages. For this situation, the pressure dependence expected (γ in equation (7.1)) is given for several limiting cases in table 7.5. See appendix B for the derivations.

At temperatures lower than T_{trans}, where the desorption of H_2 is slow, we find, just as in our qualitative argumentation given above, $\gamma = 0$ if the formation of H_2O from co-adsorbed H and OH is not possible. Clearly, this is not the case in our experiments. Allowing this reaction channel in our experiments, the experimentally found value of $\gamma = 0.57$ at room temperature is only about one standard deviation lower than the predicted value of 0.67. This difference may be caused by deviations due to the simplifications

Situation	Temperature	γ	Recombination H+OH?
No hydrogen desorption	$T < T_{\text{trans}}$	0	no recombination
		2/3	recombination
Hydrogen desorption	$T > T_{\text{trans}}$	1	slower than oxidation
		4/5	faster than oxidation

TABLE 7.5: Possible simplifications in the rate-equations of appendix B.3, temperature region where the approximation is valid and pressure dependence coefficient γ in equation (7.1) obtained. It is assumed that the nucleation rate is low and oxide growth is dominated by the growth of existing islands.

and approximations made. If, for example, at this temperature the typical time scale for the recombination and subsequent desorption of H_2O is only slightly shorter than the time scale of the experiment (10^4 s), γ will have a lower value (because the OH surface concentration will reach the saturation value). Also the presence of surface defects serving as nucleation sites may increase N_i in equation (B.22) and thereby decrease γ.

With the parameter set of table 7.4 we calculated the expected pressure dependence of the maximum oxidation rate at room temperature, with equation (B.12) for the OH coverage (dashed line in figure 7.10 **(a)**). The agreement with the experimental results is reasonable, so we conclude that the first explanation is valid: the room temperature oxidation is an intermediate case where the typical time scale for the recombination and subsequent desorption of H_2O is on the time scale of the experiment. For pressures exceeding 10^{-5} mbar, the OH surface coverage starts to saturate. For the correspondence between model and experiment, we do not need to take into account the presence of surface defects.

At temperatures above T_{trans}, we again find two possible limits (see table 7.5). If the rate constant for recombination of H_2O is much higher than the rate constant for oxide formation ($k_2'/k_4 \gg 1$, see section B.3.3), the surface coverages of H and OH depend only slightly on the oxidation rate and $\gamma = 4/5 = 0.8$ is found. This is within the error equal to the experimental value ($\gamma = 0.77 \pm 0.06$). In the opposite limit ($k_2'/k_4 \ll 1$) we would have $\gamma = 1$, which is not in agreement with the experimental value. Indeed, with the parameter values of table 7.4, k_2'/k_4 varies between $2{\times}10^{17}$ (350K) and 10^{19} (450K).

The Influence of a Nitrogen Monolayer

Comparing the oxidation curves in figure 7.7, we see that the nucleation process completes at lower oxygen coverages (lower value of $V_{\max}$) and $R_{\max}$ is higher for the N-covered Fe(100) surfaces at both RT and 365K. In the rate equations model of appendix B, this occurs if the presence of nitrogen increases the average island density $\overline{N}$ (except in the case of pure two-dimensional growth – $\alpha = 0$ – where this leads to an increase in $R_{\max}$, but not to a decrease of $V_{\max}$). An increase of the island density N (and thus also of $\overline{N}$) can be achieved in the model by increasing the cross section for nucleation (σ_n) or by increasing N_i, the density of nuclei (defects) at $\theta = 0$. The simplest explanation is that the nitrogen surface atoms serve as extra nucleation (OH dissociation) sites (increasing N_i). An increase of σ_n seems unlikely.

From equation (B.20) we derive the following relation:

$$V_{\max} = \beta M^{1+\alpha} \overline{N}^{-\alpha} \tag{7.8}$$

Because β determines the area-height ratio of the oxide islands, we assume β to be constant at constant temperature. Thus, if we increase the average island density $\overline{N}$, the oxygen coverage at coalescence decreases. The maximum oxidation rate increases with increasing $\overline{N}$. This is in agreement with the results in figure 7.7. So, assuming that for the oxidation without the nitrogen deposition the islands have fully coalesced at $V = V_{\max,1}$ and the maximum oxidation rate is $R_{\max,1}$ while in the same manner we have $V_{\max,2}$ and $R_{\max,2}$ for the oxidation of nitrogen pre-covered Fe(100), we can calculate α and the ratio of island densities $\overline{N_2}/\overline{N_1}$. For the curves in figure 7.7 **(a)**, we have $R \propto \sqrt{N}$ according to equation (B.23). For the curves in figure 7.7 **(b)**, we have $R \propto N^{1/3}$ according to equation (B.26). The results of these calculations are presented in table 7.6. For the determination of $V_{\max}$, we assumed that nucleation and growth started at $N_O = 1.3{\times}10^{15}$ atoms/cm^2 and we take only the additional oxygen to be included in $V_{\max}$. As can be seen from the table, at RT we have something between two- and three-dimensional growth (islands becoming flatter as the coverage increases), while at 365K the growth is almost completely two-dimensional (flat oxide islands which grow only in the lateral directions).

If we take the maximum island densities, calculated with the values of α determined here and the parameter values of table 7.4, as values for $\overline{N_1}$, we obtain $\overline{N_2} \sim 10^{13}$ cm^{-2} at both temperatures. This is less than 10% of

Temperature	$V_{\max,1}/V_{\max,2}$	$R_{\max,1}/R_{\max,2}$	$\overline{N_2}/\overline{N_1}$	α
(a) RT	1.45	0.385	6.8	0.20
(b) 365K	1.22	0.25	64	0.05

TABLE 7.6: Measured and calculated parameters for the comparison of the curves in figure 7.7 with the rate equations model for nucleation and growth.

the nitrogen areal density, which is a further indication that the nitrogen forms clusters at the surface.

Oxidation Curves

In figure 7.11, the measured oxidation curve at 365K is compared with calculations in the rate equations model, using the parameter values of table 7.4. We slightly varied the values of the pre-exponential factors to obtain a best fit for this single measurement. At other temperatures, equally good fits could be obtained. At all temperatures, the rate equations model deviates from the measurements after $\theta \approx 0.3$ ($N_O > 2.8{\times}10^{15}$ atoms/cm^2). This deviation after $\theta \approx 0.3$ is also observed by Brune [114], who compares the results of a rate equations model using the same coalescence term (second term in equation (B.18)) with Kinetic Monte Carlo simulations of nucleation and growth. Apparently, the coalescence term is only an approximately correct description for low island coverages. As the island coverage and the number of islands which have coalesced increase, the average island shape will deviate from the circular shape assumed and the coalescence term will not be applicable. Application of more (empirical) terms, to obtain the experimentally observed passivation, will not change the temperature and pressure dependence of the maximum oxidation rate dramatically, so we can still conclude that the rate equations model describes the experimental observations with a realistic parameter set.

If we change the model and assume that only OH groups which are *between* the islands contribute to the growth, oxidation curves are obtained where the oxidation rate always equals zero at $V = V_{\max}$ (due to an extra term $(1-\theta)$ in the equation for the oxidation rate). This extra condition would indicate that there is a difference between OH adsorbed on the oxide islands and OH adsorbed on the first monolayer of oxygen between the islands. However, we cannot falsify the model given above on this ground,

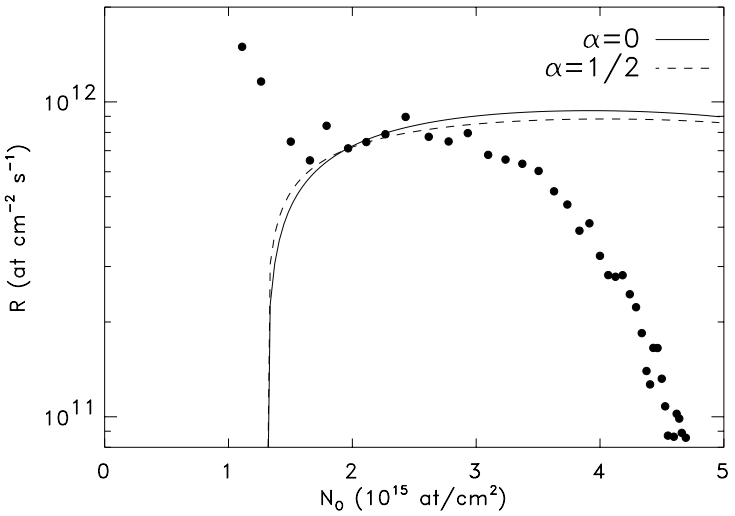

FIGURE 7.11: Oxidation rate vs. oxygen coverage at 365K. Solid symbols: measurement. Lines: rate equations model with the parameters from table 7.4.

because it is known that the coalescence term used is not applicable for $\theta > 0.3$.

7.6 Conclusions

In summary, we have shown that:

1. After the growth of the first monolayer, the oxidation curves of Fe(100) in H_2O vapor show a typical *S*-shape. This *S*-shape is an indication of nucleation and growth kinetics. The maximum oxidation rate shows two temperature regimes. Below the transition temperature $T_{\text{trans}} = (340 \pm 6)$K, we have $R_{\max} \propto p^{0.57\pm0.08}$ and $R_{\max}$ increases with increasing temperature. Above T_{trans}, we have $R_{\max} \propto p^{0.77\pm0.06}$ and $R_{\max}$ decreases with increasing temperature.

2. We propose a nucleation and growth model based on rate equations for the OH, H and H_2O coverages. The oxidation proceeds by dissociation of adsorbed OH at the edges of oxide islands. In this model,

the transition at $T = 340$K is due to the formation and desorption of H_2 which is slow below T_{trans} and fast above T_{trans}. The decrease in the oxidation rate is due to the recombination of OH and H and the subsequent desorption of H_2O. Furthermore, we assumed that the formation of new nuclei is only possible between existing islands. We assumed that the oxidation rate is directly proportional to the density of edge sites of circular oxide islands. We assumed that the shape of the islands was independent of the island density.

3. With this nucleation and growth model, we could predict the temperature and pressure dependence of R_{max} with a realistic and consistent set of parameters: the activation energies for the H_2O desorption, H_2O dissociation, H_2 desorption and recombination of H and OH are in agreement with TPD results on iron oxides in the literature. We did not need to take into account the presence of defects (nucleation sites) before the start of the oxidation.

4. The oxidation curves predicted by the model deviate from the experimental data after $\theta \approx 0.3$: the model fails to predict the experimentally observed passivation by coalescence of the islands. This is due to the mathematical expression taken for the coalescence of islands (which assumes circular and randomly placed islands, a condition which is met only before and in the early phases of coalescence). Both calculations for three-dimensional growth and calculations for two-dimensional growth showed good agreement with the experimental data.

5. Also the oxidation in H_2O of Fe(100) covered with N can be described with the nucleation and growth model. The maximum oxidation rates are higher than those of clean Fe(100) both at RT and 365K, while the saturation coverages are lower: the nitrogen facilitates the nucleation and growth of iron oxide islands. By applying the model, we could assess that at room temperature, the average island thickness increases approximately with the square root of the average island diameter. At 365K, we found two-dimensional growth: the average island thickness remains constant during the oxidation.

6. The depth of deposited nitrogen after oxidation is in agreement with the assumed nucleation and growth of oxide islands.

Appendix A

Quantitative XPS

A.1 Quantitative XPS

Usually, quantification methods for XPS involve correction for the spectrometer work function and transmission function (described in sections 2.7.2 and 2.7.3), followed by subtraction of the background due to inelastically scattered electrons. Usually the background is a linear or Shirley type [47,48]. Following background subtraction, Gaussian or Lorentzian functions, representing contributions from different (chemical) species, are fitted to the resulting spectrum. From the peak intensities, layer thicknesses are calculated. Sometimes, sensitivity factors [36] are used to calculate stoichiometries from peak intensities.

However, the errors introduced by incorrect background subtraction, the use of sensitivity factors and fitting can amount to about 30% [36]. The most correct way to analyze the spectra seems to be to use the formalism of Tougaard to subtract backgrounds, and to relate the intensities of the resulting spectrum to those of reference spectra of bulk samples measured with the same instrument, under the same conditions, as described in section A.2. Tougaard has developed a general formalism to subtract backgrounds from XPS spectra in a physically meaningful way [27,28]. Based on this formalism, expressions were derived by Hansen and Tougaard [49] for the background function in case the depth profile of the different atoms in the analyzed part of the sample is known. Based on these expressions, a method has been developed by Graat *et al* [29–31] to reconstruct the measured spectrum from reference spectra of Fe, FeO and Fe_2O_3, measured in the same instrument. In this way the use of sensitivity factors, which can differ from instrument to instrument, is avoided. Also the fitting of several more or less arbitrary Gaussian or Lorentzian functions to a residual spectrum is avoided. The Tougaard formalism and the fitting procedure are described in sections A.3 and A.4, respectively.

A.2 Photoelectron Peak Intensities

In general, the XPS yield of a peak at kinetic energy E_X from an electron level of element X with atomic density $N_X(x)$, as a function of depth in the sample x, is, using the exponential depth distribution (DDF), given by [35]:

$$Y_X = IF\sigma_X(h\nu)\int_0^\infty N_X(x)\exp(\frac{-x}{\lambda(E_X)\cos\theta})\mathrm{d}x \tag{A.1}$$

Here $\sigma_X(h\nu)$ is the cross-section for emission of a photoelectron in the direction of the analyzer from the relevant inner shell per atom of X by a photon of energy $h\nu$. I is the flux of the used X-ray line per unit area at the sample and F is a spectrometer dependent function containing the detection efficiency. The depth distribution function DDF is characterized by the inelastic mean free path (IMFP) $\lambda(E)$ of the photoelectrons (if the effect of elastic scattering is ignored [50–52]). Cumpson and Seah [57] have proposed to use the attenuation length AL in an exponential description of the Depth Distribution Function (DDF), rather than the IMFP, to account for the effect of elastic scattering. Although this is essentially not correct [59], the results given by this approximation are accurate if the detection angle β is close to the so-called 'magic angle' of 54°, where the effect of elastic scattering is small. This is the case in our experiments. For reasons of consistency, however, we will refer to the AL if we mean the characteristic length λ for the exponential DDF.

For bulk samples, the photoelectron yield is given by:

$$Y_X^\infty = N_X\lambda(E_X)\cos\theta IF\sigma_X(h\nu) \tag{A.2}$$

To obtain the intensities of Fe(2p) photoelectron peaks, a background has to be subtracted from the spectrum. This background is obtained by reconstructing the measured Fe(2p) spectrum as described in sections A.3 and A.4. The reduced thickness $\delta = d_{\mathrm{ovl}}/\lambda(E_X)$ of the oxide layer is obtained by fitting the parameters δ and the fractions of the two oxidation states of oxidized iron (Fe^{2+} and Fe^{3+}).

Following this, $J_{\mathrm{sub}}(E)$, the substrate part of the reconstructed spectrum, is subtracted from the measured spectrum $J(E)$. This is depicted in figure A.1. The result is the oxide part of the Fe(2p) spectrum $J_{\mathrm{ox}}(E)$, including background. The photoelectrons in this part of the spectrum originate from the overlayer only. According to Tougaard's formalism a background for thin overlayers can be subtracted from J_{ox} to obtain the background corrected spectrum $F_{\mathrm{ox}}(E)$ [27]. (This spectrum is not to be confused with the intrinsic spectrum $j(E)$ from equation (A.8), which is essentially the photoelectron emission spectrum of one atom.)

We can now determine yields needed for quantitative XPS, which are given by (A.1). The ratio of the substrate contribution to the yield of clean iron is

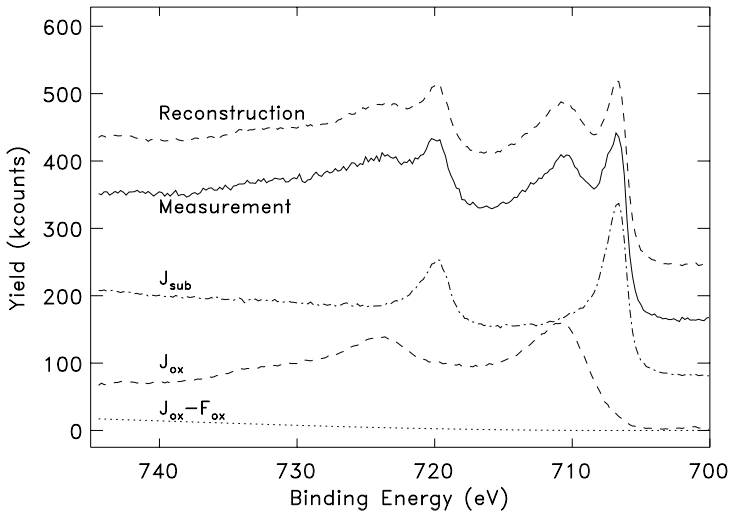

FIGURE A.1: Fe 2p spectra of a Fe(100) substrate, oxidized at room temperature for 60 minutes at an oxygen pressure of 2.0×10^{-6} mbar. The different contributions are explained in the text. Solid line: raw XPS data. Dash-dotted line: substrate contribution. Dashed line: oxide contribution. Dotted line: Tougaard background. The substrate contribution and the background are calculated with expression (A.13). The thickness of the oxide layer, obtained from the reconstruction shown, amounted to $1.05\times\lambda$. Other parameters for the reconstruction were 53% Fe^{2+} and 47% Fe^{3+} in the oxide layer.

calculated with:

$$\frac{Y_{\mathrm{sub}}}{Y^0_{\mathrm{sub}}} = \exp(\frac{-\delta}{\cos\theta}) \tag{A.3}$$

The yield of the oxide part of the Fe(2p) spectrum Y_{ox} is given by:

$$Y_{\mathrm{ox}} = \int_{E_1}^{E_2} F_{\mathrm{ox}}(E)\mathrm{d}E \tag{A.4}$$

where the interval (E_1,E_2) contains the peak. Then, the following relation holds:

$$Y_{\mathrm{ox}} = Y^{\infty}_{\mathrm{ox}}[1 - \exp(\frac{-d_{\mathrm{ovl}}}{\lambda_{\mathrm{ox}}\cos\theta})] \tag{A.5}$$

Equations (A.3) and (A.5) are independent of the interval chosen if there is no overlap with other photoelectron peaks. In this work E_1=705 eV and E_2=715 eV are used. In this region the ratio of the background to the XPS yield is very small, which minimizes the error due to a not entirely correct calculation of the background. (See sections A.3 and A.4 for this calculation.)

For the quantitative analysis of the O(1s) region, again a background is subtracted according to Tougaard's general formalism. We use 'Tougaard's general expression', as given in equation (A.12), rather than the more correct equation for the background of photoelectrons originating from a thin overlayer, calculated with equation (A.8), because for this equation one needs to know the value of δ. It is exactly this value of δ which we are trying to determine. Thus a small error is introduced here, because the oxygen signal originates from the overlayer only, and we slightly overestimate the background contribution to the spectrum. But because (in contrast with the Fe(2p) region) the background contains only about 4% of the total yield, the error introduced is estimated to be ∼1%.

For the resulting O(1s) yield Y_{O1s}, the number of counts between 525 and 535 eV is taken. In analogy with equation (A.5), the following relation holds:

$$Y_{\mathrm{O1s}} = Y^{\infty}_{\mathrm{O1s}}[1 - \exp(\frac{-d_{\mathrm{ovl}}}{\lambda_{\mathrm{O1s}} \cos\theta})] \tag{A.6}$$

A.3 Background Subtraction: The Tougaard Method

Figure A.2 shows the region around two XPS peaks ($\mathrm{Cu(2p_{1/2})}$ and $\mathrm{Cu(2p_{3/2})}$). On the low kinetic energy side the intensity is at a higher level compared to the high energy side. There are two reasons for this [116]:

- Due to electrostatic screening of the core hole created in the photo-excitation process the peak is asymmetric with features on the low energy side corresponding to the excitation of intrinsic plasmons. These electrons are part of the primary excitation spectrum.
- On their way out of the solid, the photoelectrons may suffer inelastic scattering events and as a result end up with a lower energy in the spectrum.

Before quantitative analysis can be done, the contribution of inelastically scattered electrons to the spectrum should be known.

The problem of the calculation of the inelastic background has been addressed by a number of authors [117–119]. Shirley [117] first noticed that the background intensity was proportional to the integrated peak intensity at higher energy. If the background varies slowly in the vicinity of the peak and no plasmon peaks are visible, a more simplified procedure is often applied, which is called the straight-line method [36]. Both the Shirley method and the straight line approximation

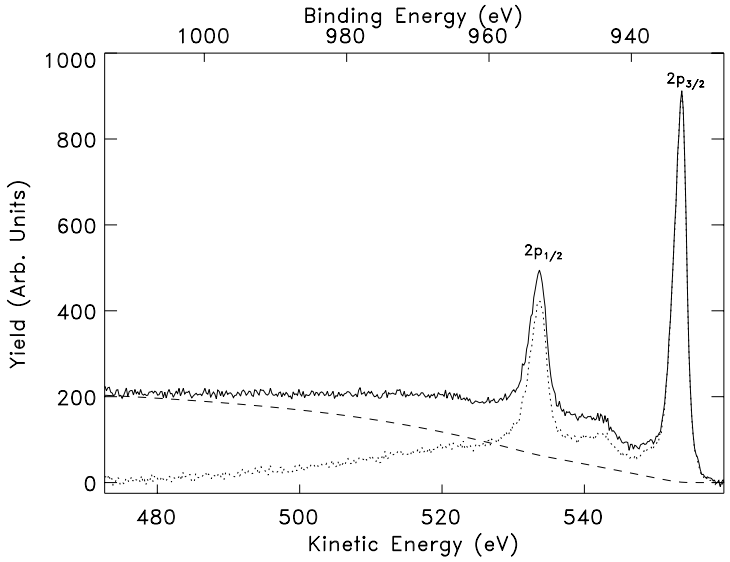

FIGURE A.2: The Cu($2p_{1/2}$,$2p_{3/2}$) XPS peaks of a clean Cu sample. Solid line: measurement (corrected for the transmission function). Dotted line: spectrum after Tougaard background subtraction. Dashed line: background.

are most often found in commercial data handling systems. Later, Tougaard and co-workers [27,28,116] proposed a deconvolution formula using a realistic model for the energy loss process.

The Tougaard method was tested and compared with the results obtained by the approach of Shirley and the straight line method [7,36,118]. It was found that for peaks at similar energy in one sample the deviations of experimentally determined peak intensity ratios from those calculated theoretically was about 30% in the case of both the Shirley and straight line methods and only about 3% in case of the Tougaard method. Clearly, the Tougaard method is superior, both with respect to the consistency and the validity compared with theory.

Tougaard's method to remove the contribution of this background [27,28] and obtain the primary excitation spectrum considers the cross-section for inelastic electron scattering $K(E,T)$, representing the probability that an electron with kinetic energy E loses an amount of energy T (per unit energy and per unit distance traveled in the specimen). Tougaard and co-workers showed that for many solids, the cross-section $K(E,T)$ is approximated by a 'universal' cross-section, which is

given by [120,121]:

$$K(E,T) = \frac{1}{\lambda_{\mathrm{i}}(E)} \frac{BT}{(C+T^2)^2} \tag{A.7}$$

where B and C are parameters which can be adjusted for a specific material and $\lambda_{\mathrm{i}}(E)$ is the IMFP of electrons with kinetic energy E in the sample. According to Hansen and Tougaard [49], the intrinsic photoelectron spectrum $j_X(E,\Omega)$ – the number of electrons, emitted with energy E per atom of element X in the direction Ω, per second, per unit energy – is obtained from the measured spectrum $J_X(E,\Omega)$ – the number of electrons detected in direction Ω, per unit energy, per second – with the following equation [49,122]:

$$j_X(E,\Omega) = \frac{1}{P_1}\{J_X(E,\Omega) - \frac{1}{2\pi}\int_E^\infty \mathrm{d}E' J_X(E',\Omega) \int_{-\infty}^{\infty} \mathrm{d}s \exp(-is(E-E'))[1-\frac{P_1}{P(s)}]\} \tag{A.8}$$

with:

$$P(s) = \int_0^\infty N_X(x) \exp(-\frac{x}{\cos\theta}\Sigma(s))\mathrm{d}x \tag{A.9}$$

$$P_1 = \int_0^\infty N_X(x) \exp(-\frac{x}{\lambda(E)\cos\theta})\mathrm{d}x \tag{A.10}$$

where $N_X(x)$ is the atomic density of element X as a function of depth in the sample x and θ is the detection angle relative to the surface normal. The function $\Sigma(s)$ is given by:

$$\Sigma(s) = \frac{1}{\lambda(E)} - \int_0^\infty K(T) \exp(-isT)\mathrm{d}T \tag{A.11}$$

As is recognized from the equations, the DDF used is exponential, so the AL of the photoelectrons is a better approximation for $\lambda(E)$ in the equations than the IMFP $\lambda_{\mathrm{i}}(E)$.

In the case of a bulk sample, N_X does not depend on x, and equation (A.8) reduces to:

$$j_X(E,\Omega) = \frac{1}{N_X\lambda(E)\cos\theta}\{J_X(E,\Omega) - \int_E^\infty \mathrm{d}E' J_X(E',\Omega)\lambda(E)K(E,E'-E)\} \tag{A.12}$$

The term between the brackets is known as *Tougaard's general expression* for the removal of the background due to inelastically scattered electrons. Despite its name, however, the expression is extremely limited and the genuinely general expression (A.8) should be used. Equation (A.12) is frequently encountered in the

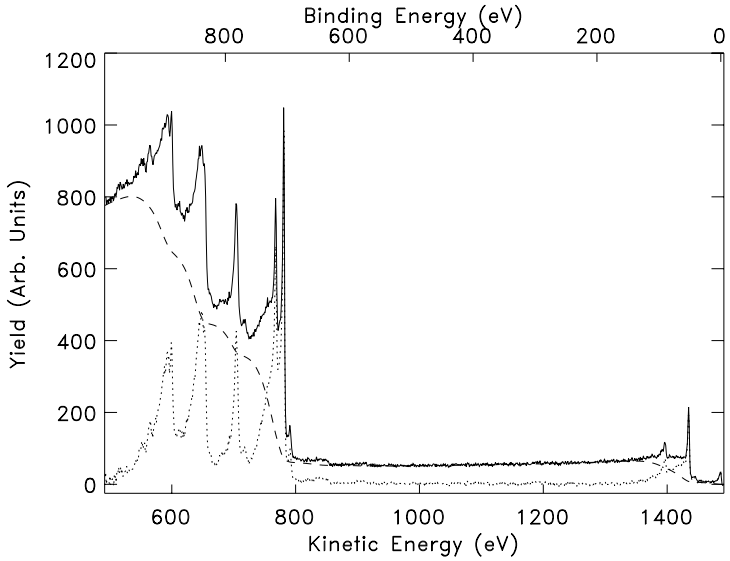

FIGURE A.3: The XPS spectrum of Fe. Solid line: measurement (corrected for the transmission function). Dotted line: spectrum after Tougaard background subtraction. Dashed line: background.

literature as a convenient way to subtract the background from XPS spectra from all sorts of samples. The advantage of using equation (A.12) instead of a linear of Shirley type background is that it has a clear physical basis [120,123] and, as mentioned above, it yields reliable results for bulk metals and compounds. The dashed line in figure A.2 shows the background calculated with equation (A.12) for the Cu(2p) spectrum of a homogeneous copper sample.

Still, the use of this expression is risky for two reasons: First, if the depth distribution of the different elements is not uniform, equation (A.8) will yield a different background than the 'general expression'. If the depth distribution is known (which is not generally the case), equation (A.8) is preferred. If the depth distribution is not known, the most correct way to proceed is to assume a certain depth distribution, then calculate the depth distribution from the spectrum (or, preferably, several spectra taken with different values of θ) using equation (A.8), and then iterate. Second, incorrect choices for the values of B and C lead to large errors and care has to be taken to avoid these. The value of B should be chosen in such a way that the intrinsic spectrum has zero yield in parts of the spectrum without peaks, as is shown in figure A.3 for the XPS spectrum (corrected for the transmission function) of figure 2.9. Here, the large featureless energy range between 900 eV and 1300 eV enables us to find the correct value of

B ($B = 3218$ eV^2). A determination of B from the Fe(2p) part of the spectrum would have resulted in an incorrect value for B and thus unreliable results.

Tougaard and co-workers have determined the cross-section for inelastic electron scattering for a number of materials from optical data, and fitted the 'universal' cross section (A.7) to these functions. The value for C obtained in this way was $C = 1643$ eV^2, which we will use in this work.

A.4 Reconstruction of the Fe(2p) Spectrum

A.4.1 Outline

In case of the oxidation of iron at $T < 475$K, it is known that a flat oxide layer grows on top of the substrate, with a sharp interface. The iron in the oxide can be in two oxidation states: Fe^{2+} and Fe^{3+}. Because the peak positions of Fe^{2+} and Fe^{3+} are separated by only about 1 eV, it is not easy to determine the Fe^{2+}/Fe^{3+} ratio in the oxide layer by a qualitative analysis of the spectrum. However, Graat and Somers were the first to recognize that the XPS spectrum, including correct backgrounds, can be easily calculated from the intrinsic spectra of bulk Fe^{2+} and Fe^{3+} containing compounds (FeO and Fe_2O_3, respectively) and clean iron, using equation (A.8) [29–31]. Input for this calculation is the Fe^{2+}/Fe^{3+} ratio and the thickness of the oxide layer (with respect to the AL).

Equation (A.8) can be written in the following way [30]:

$$J_X(E,\Omega) = P_1 \cdot j_X(E,\Omega) + \frac{1}{2\pi} \int_E^\infty \mathrm{d}E' J_X(E',\Omega) \int_{-\infty}^{\infty} \mathrm{d}s \exp(-is(E-E'))[1-\frac{P_1}{P(s)}]\} \tag{A.13}$$

Now $J_X(E,\Omega)$ is calculated by evaluating equation (A.13) in a stepwise manner, starting at the high kinetic energy side, using equations (A.9) and (A.10) with the assumed depth distribution of X to calculate $P(s)$ and P_1. The total reconstructed spectrum is then given by summing the contributions from different elements or oxidation states.

In order to determine the oxidation state and thickness of thin iron oxide films on pure iron, Fe(2p) spectra were analyzed with this method: The measured sample was reconstructed using reference spectra for Fe^0, Fe^{2+} and Fe^{3+}. For each of these reference spectra (after correction for the spectrometer transmission function), the background corrected intrinsic spectrum was calculated by subtracting the background according to Tougaard's formula for bulk samples (A.12). A spectrum for a substrate/overlayer structure was then constructed by combining the Fe, FeO and Fe_2O_3 background corrected spectra and adding corresponding backgrounds according to equation (A.13). We took $B_{\mathrm{sub}} = 3218$ eV^2, $B_{\mathrm{ox}} = 3550$ eV^2 and $C = 1643$ eV^2 as the parameters for Tougaard's 'universal cross-section' (A.7).

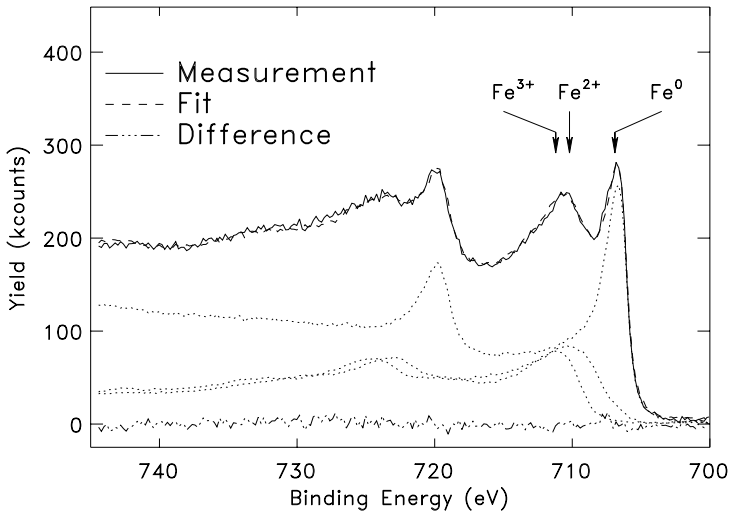

FIGURE A.4: Reconstruction of the Fe(2p) spectrum of a Fe(100) substrate, oxidized at room temperature for 60 minutes at an oxygen pressure of 2.0×10^{-6} mbar. The fitted values were $d_{\mathrm{ovl}}=1.05\times\lambda$, $C_{\mathrm{Fe^{2+}}}=0.53$ and $C_{\mathrm{Fe^{3+}}}=0.47$. Solid line: measurement. Dashed line: reconstruction. Dotted lines: contributions of Fe^0, Fe^{2+} and Fe^{3+}, calculated from the reference spectra. Dash-dotted line: difference between measurement and fit.

The values of B were obtained from the total XPS spectrum of the reference samples by adjusting the value of B to assure that the corrected spectrum is zero at energies far away from the peak. The value of C was taken from the literature [27]. For a substrate of iron metal, the expression describing the background of a bulk sample buried under a homogeneous layer with thickness $\delta = d_{\mathrm{ovl}}/\lambda$ was used, where d_{ovl} is the oxide layer thickness and λ is the AL in the oxide. For the FeO and Fe_2O_3 spectra, the expression for the background of a thin overlayer was used. The reconstructed spectrum was compared to the measured spectrum, which was corrected for the transmission function. The reduced thickness δ of the oxide layer was then obtained by fitting the parameters δ and the fractions of Fe^{2+} and Fe^{3+} in the oxide layer.

A.4.2 The Reconstruction

Figure A.4 shows a typical spectrum which was reconstructed using equation (A.13) with the reference spectra given in figure 2.11. For the reconstruction the film thickness δ (relative to the Attenuation Length AL) and the intensities of Fe^{2+} and Fe^{3+} ($I_{Fe^{2+}}$ resp. $I_{Fe^{3+}}$) were used as fit parameters. In this particular case (RT oxidation for 60 minutes in 2.0×10^{-6} mbar O_2), the fit results were $d_{ovl}=1.05\times\lambda$, $C_{Fe^{2+}}=0.53$ and $C_{Fe^{3+}}=0.47$. ($C_{Fe^{n+}} = I_{Fe^{n+}}/(I_{Fe^{2+}} + I_{Fe^{3+}})$) With λ we denote the AL of the oxide layer. In Chapter 4 of this thesis, we determine λ to be 9.3×10^{15} O atoms/cm^2 at E_K=776 eV, using a combination of XPS and ERD. This corresponds to an oxide thickness of about 2 nm.

The agreement between the reconstruction and the measured spectrum is very good; it is very sensitive to the ratio $C_{Fe^{2+}}/C_{Fe^{3+}}$, yielding an absolute error in $C_{Fe^{2+}}$ of $\sim$5 %.

Appendix B

A Rate Equations Model for the Reaction between H_2O Vapor and Fe(100)

B.1 Introduction

This appendix provides the necessary chemical reactions and rate equations needed in the discussion of chapter 7. First, we will present the different relevant surface processes and reactions and determine the dependence of the coverages with adsorbed H_2O, OH and H on the H_2O vapor pressure by solving the rate equations. Then, we will give the equations describing the nucleation and growth of the oxide islands and give solutions for the relevant limiting cases.

B.2 The Processes at the Surface

On clean Fe or on iron oxide, the following reactions occur:

$$H_2O_a \rightleftharpoons H_2O_g \tag{B.1}$$

$$H_2O_a \rightleftharpoons OH_a + H_a \tag{B.2}$$

$$2H_a \rightarrow H_2 \uparrow \tag{B.3}$$

$$OH_a + Fe + \text{edge} \rightarrow FeO + H_a + \text{edge} \tag{B.4}$$

$$2OH_a + Fe \rightarrow FeO + \text{edge} + H_2O_a \tag{B.5}$$

These reactions are the same as reactions (7.2)-(7.6) given in chapter 7. Reaction (B.1) represents the adsorption and desorption of H_2O molecules. The

dissociation process of H_2O molecules is represented by reaction (B.2), with dissociation products OH and H. Adsorbed hydrogen atoms can form desorbing hydrogen molecules through reaction (B.3). The dissociation of OH at an oxide island edge site occurs via reaction (B.4). Two OH groups can also form a new oxide nucleus via reaction (B.5). Two reactions for the dissociation of OH are given in the literature, resembling reactions (B.4) and (B.5) [98–102]. In those reactions, the reaction product is O_a which on our sample – bulk iron under a 1 ML thin surface layer of oxygen – will almost instantaneously react with iron and the effective reactions are the ones given here. Therefore, the oxygen incorporation rate measured with ellipsometry must be equal to the summed reaction rate of both OH dissociation reactions. We denote the oxide formation product by "FeO"; with this we mean all kinds of oxides possibly present, including that with incorporated hydrogen. This incorporation of hydrogen, however, does not necessarily occur simultaneously with reaction (B.4) or (B.5). Because the reaction between oxide and hydrogen does not largely influence the balance of adsorbed species (as the rate of H_2 desorption is much larger than the rate of hydrogen uptake into the oxide, and, at room temperature, only about 25% of the H produced by reactions (B.4) and (B.5) is incorporated in the oxide), we will not take it into account. Also hydrogen disappearing into the bulk of the sample is not accounted for.

We did not write down expressions for direct desorption of OH or for the direct reaction of adsorbed H_2O with Fe giving oxide and hydrogen. Desorption of OH has never been observed, which is in agreement with the expected high value of the binding energy of OH at the surface. Regarding the direct reaction of H_2O with Fe, we observe the following: The desorption temperature of H_2O is between 160K and 260K on α-Fe_2O_3, depending on the surface orientation, reconstruction and H_2O dose [100–102]. This implies that at the temperatures of our measurements, the desorption of H_2O molecules is fast and the maximum coverage of adsorbed H_2O at the surface (assuming equilibrium between adsorption and desorption and no other reaction channels) is low and depends linearly on the H_2O pressure. Because the observed oxidation rates in chapter 7 show a less than linear pressure dependence, the direct reaction between H_2O_a and Fe is not taken into account.

It is not clear whether the desorption of H_2O above 300K observed in the literature is due to the reactions (B.2) and (B.1) or to reaction (B.5). However, if the reverse reaction (B.2) could not proceed, the surface would be completely covered with OH (and some H) independent of the H_2O pressure at the reaction rates (oxygen incorporation $\sim 10^{12}$ atoms cm^{-2} s^{-1}) measured and the oxidation rate would not depend on the H_2O pressure. Therefore, we have to take into account the recombination of H and OH followed by desorption of H_2O.

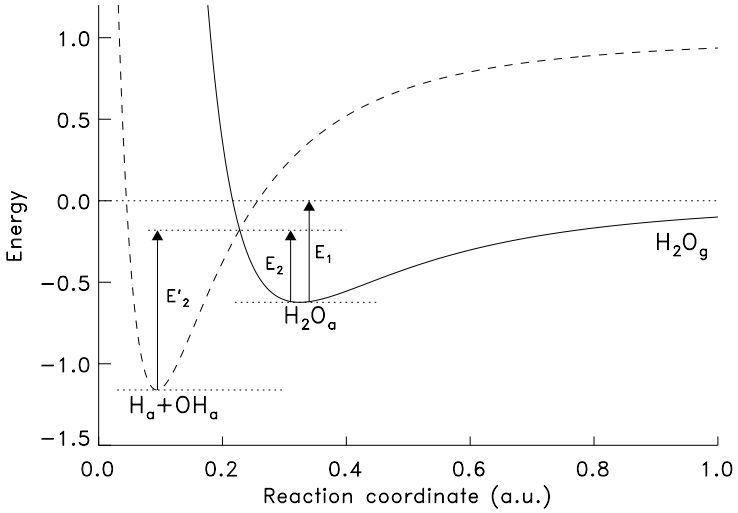

FIGURE B.1: One-dimensional Lennard-Jones potential for activated, dissociative adsorption [124].

B.3 Rate Equations

We will now write down the relevant rate equations for the reactions mentioned above. The rates of the reactions (B.1) to (B.5) are characterized by their rate constants k. Table 7.3 gives an overview of the rate constants used.

H_2O adsorbs at cationic sites on oxide surfaces [9]. As mentioned above, because of the low desorption temperature and the rapid dissociation of H_2O the coverage of adsorbed H_2O molecules at the surface is expected to be low. The dissociation products are OH and H. Adsorbed OH acts as a Lewis acid and prefers to stay at the anionic sites [9]. Following the same line of reasoning, we expect adsorbed H to be an electron donor which prefers the cationic sites. Finally, H_2O is physisorbed, and the mean distance from the sample is larger than that of the chemisorbed H and OH, as is shown in figure B.1, which gives the classical Lennard-Jones one-dimensional potential for activated, dissociative adsorption [124]. In this figure, also the energy barriers for H_2O desorption, dissociation and recombination (E_1, E_2 and E_2', respectively) are indicated. A similar potential can be drawn for "FeO"+H_2. In conclusion, H_2O, H and OH adsorb at separate lattices, which simplifies the rate equations.

For equations (B.1)-(B.5), the rate equations can be written down. For the equilibrium of adsorbed H_2O we obtain:

$$\frac{\mathrm{d}r}{\mathrm{d}t} = \Phi(1-r) - k_1 r - k_2 r(1-p)(1-q) + k_2' pq(1-r) + k_5 q^2(1-r) = 0 \quad \text{(B.6)}$$

where the fractional coverage of H is p, that of OH is q and that of adsorbed H_2O molecules is r. The first term is the arrival rate of gas molecules from the gas. The arrival rate Φ is proportional to the H_2O pressure according to $\Phi M = p_{H_2O}/\sqrt{2\pi m k_B T_{\mathrm{vapor}}}$, assuming a sticking coefficient of 1. Here, Φ is the arrival rate in monolayers per second, M is the oxygen coverage corresponding to one monolayer ($M \approx 1.3\times10^{15}$ O atoms/cm^2) and m is the mass of the H_2O molecules. We have assumed that the site density of the three separate lattices is equal. This is of course only an approximation, but we expect the site density to be at least of the same order of magnitude. The second term in equation (B.6) is the desorption rate of H_2O molecules with rate constant k_1. The third term is the decomposition rate of adsorbed H_2O molecules with rate constant k_2. Recombination of adsorbed OH and H is represented by the fourth term, where the rate constant is k_2' for reaction (B.2) in the reverse direction. Finally, the nucleation reaction (B.5) leads to the last term with rate constant k_5. Assuming steady-state conditions, we have put $\mathrm{d}r/\mathrm{d}t$ equal to zero.

In the same manner, we can write:

$$\frac{\mathrm{d}q}{\mathrm{d}t} = k_2 r(1-p)(1-q) - k_2' pq(1-r) - k_4 q(1-p) - 2k_5 q^2(1-r) \quad \text{(B.7)}$$

$$\frac{\mathrm{d}p}{\mathrm{d}t} = k_2 r(1-p)(1-q) - k_2' pq(1-r) - 2k_3 p^2 + k_4 q(1-p) \quad \text{(B.8)}$$

where k_4 is the rate constant for reaction (B.4). This rate constant depends on the number of island edge sites and thus on the island coverage. In section B.3.4 this dependence is given and the nucleation and growth kinetics are calculated.

By subtracting (B.7) from (B.8), we obtain:

$$2k_5 q^2(1-r) + 2k_4 q(1-p) = 2k_3 p^2 \quad \text{(B.9)}$$

In other words: oxidation can only proceed if the desorption of hydrogen is possible (*i.e.* $k_3 \neq 0$).

If the oxidation is slow compared to the rates of desorption, dissociation and recombination (k_4 and k_5 are small), the combination of equations (B.6) and (B.7) gives:

$$r = \frac{\Phi}{\Phi + k_1} \quad \text{(B.10)}$$

The analytical solution of the rate equations for p and q is lengthy. To gain insight, we shall give the simplified solutions in limiting cases.

B.3.1 Case 1: $k_3 = 0$

If $k_3 = 0$ (hydrogen desorption does not occur on the time scales of the experiment), we have:

$$q = 0 \quad p = 1 \tag{B.11}$$

Because the oxidation rate is proportional to $k_4 q(1-p)$ and $k_5 q^2(1-r)$, oxidation cannot continue to proceed in this case. Clearly, this is not the case in our experiments.

However, if we assume that k_4 and k_5 are sufficiently small and the balance of adsorbed species is – in approximation – determined by the dissociation and recombination of H_2O molecules only, we obtain:

$$p = q = \frac{k_2 r - \sqrt{k_2' k_2 r(1-r)}}{k_2 r - k_2'(1-r)} \tag{B.12}$$

If $k_2 r \ll k_2'(1-r)$, this reduces to $p = q = \sqrt{k_2 r / k_2'(1-r)} = \sqrt{k_2 \Phi / k_2' k_1}$. If $k_2 r \gg k_2'(1-r)$, we obtain $p = q = 1$.

B.3.2 Case 2: $k_4 = 0$ and $k_5 \neq 0$ (Nucleation)

Let us now consider the situation where the oxidation rate is dominated by nucleation of oxide islands via reaction (B.5). This situation occurs just after the completion of the first monolayer of oxide and the beginning of the nucleation and growth regime: the number of islands is low and the islands are small, so k_4 is small. In the limiting case where $k_4 = 0$, we have (in an approximation which is valid if $q \ll 1$ and $p \ll 1$):

$$\begin{aligned} q &\approx \left[\frac{k_2 \sqrt{2k_3}}{\sqrt{2k_5(1-r)}k_2' + \sqrt{8k_3}k_5} \frac{\Phi}{k_1} \right]^{1/2} \\ p &\approx \left[\frac{k_2 (1-r)}{\sqrt{2k_5(1-r)}k_2' + \sqrt{8k_3}k_5} \frac{\Phi}{k_1} \right]^{1/2} \end{aligned} \tag{B.13}$$

Again, the approximations are valid for temperatures much larger than the desorption temperature of H_2O, which is the case in all our experiments.

B.3.3 Case 3: $k_5 = 0$ (Growth of Islands)

As the oxide islands start to grow, the rate constant k_4 increases. When the islands start to coalesce, k_4 decreases again, but also the rate of formation of new nuclei decreases upon coalescence. So, after the initial stage with mainly nucleation, we have a stage where the growth of islands is the dominant oxidation mechanism.

symbol		unit
D	Surface diffusion constant	$cm^2\ s^{-1}$
M	monolayer coverage	cm^{-2}
N	island density	cm^{-2}
p	fractional H coverage	
q	fractional OH coverage	
r	fractional H_2O coverage	
V	oxygen areal density	cm^{-2}
V_{max}	oxygen areal density at saturation	cm^{-2}
α	coefficient for growth mode	
β	coefficient describing the island shape	
θ	island coverage	
Φ	H_2O arrival rate	$ML\ s^{-1}$
σ_n	cross section for nucleation	
σ_g	cross section for island growth	

TABLE B.1: Symbols used for the different variables and constants in the description of nucleation and growth.

The limiting case can be found by putting $k_5 = 0$. Assuming $p \ll 1$ and $q \ll 1$, we can distinguish two regimes. If $k_2'/k_4 \ll 1$, we obtain:

$$\begin{aligned} p &= \sqrt{\frac{k_2 r}{k_3}} \approx \sqrt{\frac{k_2 \Phi}{k_1 k_3}} \\ q &= \frac{k_2 r}{k_4 + k_2 r} \approx \frac{k_2 \Phi}{k_4 k_1} \end{aligned} \tag{B.14}$$

If $k_2'/k_4 \gg 1$, we obtain:

$$\begin{aligned} p &= \left[\frac{k_2 k_4 r}{k_2' k_3 (1-r)}\right]^{1/3} \approx \left[\frac{k_2 k_4 \Phi}{k_2' k_3 k_1}\right]^{1/3} \\ q &= \frac{k_3}{k_4}\frac{p^2}{1-p} \approx \left[\frac{k_3}{k_4}\right]^{1/3}\left[\frac{k_2 \Phi}{k_2' k_1}\right]^{2/3} \end{aligned} \tag{B.15}$$

B.3.4 Lateral Growth of Islands

For the lateral growth of the islands, we follow the approach by Venables [111–114]. This approach consists of writing down rate equations for the density of surface species q (adsorbed OH), density of islands (N) and fractional island coverage (θ). The symbols used in this approach are summarized in table B.1. The equations are so-called *mean-field equations*, *i.e.* the gradient in q near the edges

of islands is not accounted for: q is assumed to be constant over the entire surface. Furthermore, we solve the equations in the *steady-state*, *i.e.* the time derivative of q is assumed to be zero and q is, depending on the limiting case, approximated by one of the expressions given above [(B.12)-(B.15)] and, finally, we assumed that nucleation is only possible between existing islands (leading to the factor $(1-\theta)$ in expression (B.17) for k_5). Here, we explicitly assume that the densities of surface species present *on* the islands are equal to the corresponding densities in between. Because the surface between the islands consists of chemisorbed oxygen the coverages may differ from those on the oxide islands. In this case, our approach will lead to wrong parameter values. However, Li *et al* [113] have shown that changing the rate equations to account for different densities of species on the islands and in between leads to only slight changes in the oxidation curves.

Assuming perfect circular and equally sized islands, the density of edge sites o (cm^{-2}) is given by:

$$o = 2\pi\frac{r_{\mathrm{isl}}}{a}N = 2\pi\sqrt{\frac{\theta M}{\pi N}}N = 2\sqrt{\pi\theta MN} \tag{B.16}$$

where a is the lattice constant of the surface lattice, and r_{isl} is the average radius of the islands. Thus, the rate constants k_4 and k_5 are given by:

$$\begin{aligned} k_4 &= 2\sigma_g D\sqrt{\pi\theta MN} \\ k_5 &= M\sigma_n D(1-\theta) \end{aligned} \tag{B.17}$$

where σ_n and σ_g are cross sections for nucleation and growth, respectively, and D is the surface diffusion coefficient given by $D = a^2\nu_{\mathrm{diff}}\exp(-E_d/k_BT)$ for a square lattice.

The rate equations for nucleation and growth are then, based on the derivation by Venables *et al* [111,114]:

$$\frac{\mathrm{d}N}{\mathrm{d}t} = M^2\sigma_n D q^2(1-\theta) - 2N\frac{\mathrm{d}\theta}{\mathrm{d}t} \tag{B.18}$$

$$\frac{\mathrm{d}V}{\mathrm{d}t} = M^2\sigma_n D q^2(1-\theta) + 2M\sigma_g D\sqrt{\pi\theta MN}q \tag{B.19}$$

The second term in equation (B.18) accounts for the decrease in island density due to coalescence of islands [111,112,125]. Again, the islands are assumed to be circular. Furthermore, they are assumed to be randomly placed. These are of course simplifications. Comparison with Monte Carlo simulations have shown that for $\theta > 0.3$, the term $2N\mathrm{d}\theta/\mathrm{d}t$ fails and the island density (and, consequently, the oxidation rate) obtained in this approach is too large. In the equations, V is the oxygen areal density (without the chemisorbed first monolayer, so we have $V = N_{\mathrm{O}} - M$) and θ is the fractional coverage of the islands, which is related to V by:

$$V = \overline{N}^{-\alpha}\beta(\theta M)^{1+\alpha} = V_{\max}\theta^{1+\alpha} \tag{B.20}$$

with β a dimensionless constant and α between 0 (two-dimensional growth) and 1/2 (three-dimensional growth). $\overline{N}$ is the average island density (averaged for all values of θ). The use of this average value is of course a simplification, but it seems the best way to account for the change in the average island shape when the islands start to coalesce. For low coverages, where the oxidation rate is dominated by nucleation rather than the growth of existing islands, this use of $\overline{N}$ may lead to some deviations from equation (B.20).

In the initial regime, where the oxidation rate is determined by the nucleation of islands ('case 2' in the previous section), we have $q \propto \Phi^{1/2}$ and $\mathrm{d}V/\mathrm{d}t \propto \Phi$ which is not in agreement with our observations of the pressure dependence in section 7.4: Apparently, the maximum oxidation rate is dominated by the growth of existing islands. Therefore, we will not consider this case.

The expressions for the OH fractional coverage q derived above are proportional to some power of the H_2O flux Φ and k_4, the rate constant for reaction (B.4). For the growth regime, equations (B.18), (B.19) and (B.20) can be combined into an expression for $\mathrm{d}N/\mathrm{d}\theta$, and then, with the mathematical treatment of Li *et al* [113], it is straightforward to prove that if $q \propto \frac{\Phi^n}{k_4^m}$, with n and m positive real numbers, we find:

$$\frac{\mathrm{d}V}{\mathrm{d}t} \propto \Phi^{\frac{4n}{m+3}} \tag{B.21}$$

This coefficient $4n/(m+3)$ must be (within the uncertainty) equal to the coefficients determined in section 7.4 for the pressure dependence of the maximum oxidation rate. In the following, we will use the various expressions for q derived above to calculate the oxidation rate vs. coverage for the growth of islands.

B.3.5 Case 1: $k_3 = 0$

If the OH density q obeys equation (B.12), we have $n = 1/2$ and $m = 0$, so $\mathrm{d}V/\mathrm{d}t \propto \Phi^{2/3}$. In this case, the solution of the rate equations can be expressed as:

$$N(\theta,\alpha) = \left(N_i^{3/2} e^{-3} + \frac{3\sigma_n}{4\sigma_g} V_{\max}(1+\alpha)\sqrt{\frac{M}{\pi}} q I(\theta,\alpha) \right)^{2/3} \exp[2(1-\theta)] \tag{B.22}$$

$$\frac{\mathrm{d}V}{\mathrm{d}t} = 2\sigma_g D \sqrt{\pi\theta M N(\theta,\alpha)}\, q \tag{B.23}$$

where N_i is the density of nuclei at $\theta = 0$. The function $I(\theta,\alpha)$ is given by:

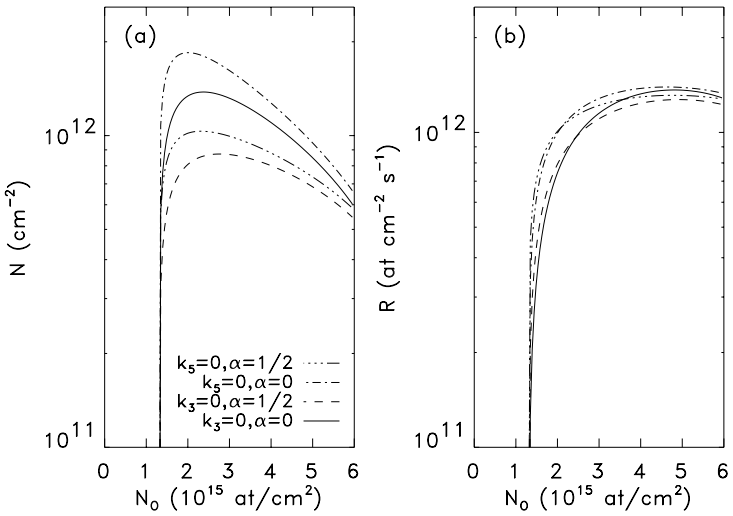

FIGURE B.2: Simulation of nucleation and growth according to the rate equations model. The parameters used are given in table 7.4, the temperature amounted to 345K and for $V_{\max}$ we took 4.5×10^{15} O atoms/cm^2. We assumed that the nucleation and growth started after the deposition of one monolayer of chemisorbed oxygen, so $V = N_O - M$. **(a)** Island density vs. oxygen coverage. **(b)** Oxidation rate vs. oxygen coverage.

$$\begin{aligned} I(\theta,\alpha) &= \int_0^\theta u^{\alpha-\frac{1}{2}}(1-u)\exp[-3(1-u)]\mathrm{d}u \\ &= -\frac{1}{e^3}\left[i(-1)^{-\alpha}3^{-\frac{3}{2}-\alpha}\left(3\Gamma(\frac{1}{2}+\alpha)+\Gamma(\frac{3}{2}+\alpha)\right.\right. \\ &\quad \left.\left.-3\Gamma(\frac{1}{2}+\alpha,-3\theta)-\Gamma(\frac{3}{2}+\alpha,-3\theta)\right)\right] \end{aligned} \tag{B.24}$$

where $\Gamma(x)$ is the Euler Γ function and $\Gamma(a,x)=\int_x^\infty t^{a-1}e^{-t}\mathrm{d}t$ is the incomplete Euler Γ function. In figure B.2, N and $\mathrm{d}V/\mathrm{d}t$ are plotted vs. N_O for $\alpha=0$ and $\alpha=1/2$. The other parameter values used in the calculations are taken from table 7.4.

B.3.6 Case 3: $k_5 = 0$

If the OH density obeys equation (B.14), we have $n = 1$ and $m = 1$ in equation (B.21), so $\mathrm{d}V/\mathrm{d}t \propto \Phi$. This is not in agreement with the experimental results, so we can rule out this limiting case.

If the OH density is close to the limiting case of equation (B.15), we have $n = 2/3$ and $m = 1/3$, so $\mathrm{d}V/\mathrm{d}t \propto \Phi^{4/5} = \Phi^{0.8}$, close to the observed value at high T (see section 7.4). In this case, the solution of the rate equations can be expressed as:

$$N(\theta,\alpha) = \left[N_i^{5/3} e^{-10/3} + \frac{5\sigma_n}{3(2\sigma_g)^{4/3}} V_{\max}(1+\alpha) \left(\frac{M}{\pi^2}\right)^{1/3} \left(\frac{k_3 k_2^2 \Phi^2}{D {k_2'}^2 k_1^2}\right)^{1/3} I(\theta,\alpha) \right]^{3/5} \times \exp[2(1-\theta)] \tag{B.25}$$

$$\frac{\mathrm{d}V}{\mathrm{d}t} = M(2\sigma_g D)^{2/3} \left(\pi\theta M N(\theta,\alpha)\right)^{1/3} \left(\frac{k_3 k_2^2 \Phi^2}{{k_2'}^2 k_1^2}\right)^{1/3} \tag{B.26}$$

where N_i is the density of nuclei at $\theta = 0$. The function $I(\theta,\alpha)$ is given by:

$$\begin{aligned} I(\theta,\alpha) &= \int_0^\theta u^{\alpha-\frac{2}{3}}(1-u)\exp[-10(1-u)/3]\mathrm{d}u \\ &= \frac{1}{10e^{10/3}(1+3\alpha)} \Big[(-1)^{\frac{2}{3}-2\alpha} 3^{\frac{1}{3}+\alpha} 10^{-\frac{5}{3}-2\alpha} \\ &\quad \times \Big(3\Big[(-10)^{\frac{1}{3}+\alpha}(-1)^{2/3} - (-1)^\alpha 10^{\frac{4}{3}+\alpha} + 3(-10)^{\frac{1}{3}+\alpha}(-1)^{2/3}\alpha \Big] \\ &\quad \times \Gamma(\frac{4}{3}+\alpha) + (1+3\alpha)\Big[(-1)^\alpha 10^{\frac{4}{3}+\alpha}\Gamma(\frac{1}{3}+\alpha, \frac{-10\theta}{3}) \\ &\quad - 3(-10)^{\frac{1}{3}+\alpha}(-1)^{2/3}\Gamma(\frac{4}{3}+\alpha, \frac{-10\theta}{3})\Big]\Big)\Big] \end{aligned} \tag{B.27}$$

where $\Gamma(x)$ is the Euler Γ function and $\Gamma(a,x)$ is the incomplete Euler Γ function. In figure B.2, N and $\mathrm{d}V/\mathrm{d}t$ are plotted vs. V for two values of α.

It should be noted that we used $k_5 = 0$ only to obtain the OH coverage in the steady-state approximation. We did not take $\sigma_n = 0$ (which would imply $k_5 = 0$) in equation (B.18).

Bibliography

[1] A. Fromhold, *Theory of metal oxidation* (North-Holland, Amsterdam, 1976).

[2] E. Fromm, *Kinetics of metal-gas interactions at low temperatures* (Springer, Berlin, 1998).

[3] R. Cornell and U. Schwertmann, *The Iron Oxides, Structure, Properties, Reactions, Occurence and Uses* (Weinheim, New York, 1996).

[4] K. Lawless, Rep. Prog. Phys. **37**, 237 (1974).

[5] G. Leibbrandt, Ph.D. thesis, Utrecht University, 1992.

[6] G. Leibbrandt, G. Hoogers, and F. Habraken, Phys. Rev. Lett. **68**, 1947 (1992).

[7] P. Görts, Ph.D. thesis, Debye Institute, Utrecht University, 1995.

[8] N. Debnath and A. Anderson, Surf. Sci. **128**, 61 (1983).

[9] P. Thiel, Surf. Sci. Rep. **7**, 211 (1987).

[10] P. Graat, M. Somers, A. Vredenberg, and E. Mittemeijer, J. Appl. Phys. **82**, 1416 (1997).

[11] R. Musket, W. McLean, C. Colmenares, D. Makowiecki, and W. Siekhaus, Appl. Surf. Sci. **10**, 143 (1982).

[12] R. Azzam and N. Bashara, *Ellipsometry and polarized light* (North-Holland, Amsterdam, 1996).

[13] P. Graat, M. Somers, and E. Mittemeijer, Thin Solid Films **340**, 87 (1999).

[14] J. Weaver, E. Colavita, D. Lynch, and R. Rosei, Phys. Rev. **B 19**, 3850 (1979).

[15] P. Johnson and R. Christy, Phys. Rev. **B 9**, 5056 (1974).

[16] T. Vink, J. der Kinderen, O. Gijzeman, J. Geus, and J. van Zoest, Appl. Surf. Sci. **26**, 357 (1984).

[17] H. den Daas, O. Gijzeman, and J. Geus, Surf. Sci. **285**, 15 (1993).

[18] F. Habraken, O. Gijzeman, and G. Bootsma, Surf. Sci. **96**, 482 (1980).
[19] F. Habraken and G. Bootsma, Acta Electronica **24**, 167 (1982).
[20] L. Feldman and J. Mayer, *Fundamentals of Surface and Thin Film Analysis* (North-Holland, New York, 1986).
[21] *Ion Beam Handbook for Material Analysis*, edited by J. Mayer and E. Rimini (Academic Press, New York, 1977).
[22] W. M. Arnoldbik and F. H. P. M. Habraken, Rep. Prog. Phys. **56**, 859 (1993).
[23] *Handbook of Modern Ion Beam Materials Analysis*, edited by J. Tesmer and M. Nastasi (Materials Research Society, Pittsburgh, 1995).
[24] J. van der Veen, Surf. Sci. Reports **5**, 199 (1985).
[25] B. Appleton and G. Foti, in *Ion Beam Handbook for Material Analysis*, edited by J. Mayer and E. Rimini (Academic Press, New York, 1977), Chap. 3, pp. 69–111.
[26] W.-K. Chu, *Backscattering Spectrometry* (Academic Press, New York, 1978).
[27] S. Tougaard and H. Hansen, Surf. Interface Anal. **14**, 730 (1989).
[28] S. Tougaard, Surf. Sci. **216**, 343 (1989).
[29] P. Graat and M. Somers, in *ECASIA 95, 6th European conference on applications of surface and Interface analysis* (Wiley, Montreux, 1995), pp. 611–614.
[30] P. Graat and M. Somers, Appl. Surf. Sci. **100/101**, 36 (1996).
[31] P. Graat, M. Somers, and A. Böttger, Surf. Interface Anal. **23**, 44 (1995).
[32] J. Rivière, in *Practical Surface Analysis*, 2nd ed., edited by D. Briggs and M. Seah (Wiley, New York, 1996), Vol. 1, Chap. 2, pp. 19–84.
[33] American Society for Testing and Materials, Surf. Interface Anal. **17**, 889 (1991).
[34] C. Powell, in *Proceedings of the Eighth International Conference on Quantitative Surface Analysis QSA-8* (National Physics Laboratory, England, 1995).
[35] *Practical Surface Analysis*, 2 ed., edited by D. Briggs and M. Seah (Wiley, New York, 1996), Vol. 1.
[36] M. Seah, in *Practical Surface Analysis*, 2nd ed., edited by D. Briggs and M. Seah (Wiley, New York, 1996), Vol. 1, Chap. 5, pp. 201–256.
[37] M. Seah, J. Electron. Spectrosc. Rel. Phen. **71**, 191 (1995).
[38] R. Lad and V. Henrich, Surf. Sci. **193**, 81 (1988).

[39] J. Gimzewski, B. Padalia, S. Affrossman, L. Watson, and D. Fabian, Surf. Sci. **62**, 386 (1977).
[40] C. Brundle, T. Chuang, and K. Wandelt, Surf. Sci. **68**, 459 (1977).
[41] N. S. McIntyre and D. Zetaruk, Anal. Chem. **49**, 1521 (1977).
[42] P. Bagus and C. Bauschlicher, J. Electron. Spectrosc. Rel. Phen. **20**, 183 (1980).
[43] G. Pirug, G. Brodén, and H. Bonzel, Surf. Sci. **94**, 323 (1980).
[44] V. Stambouli, C. Palacio, H. Mathieu, and D. Landolt, Appl. Surf. Sci. **70/71**, 240 (1993).
[45] A. Sault, Appl. Surf. Sci. **74**, 249 (1994).
[46] P. Lee, K. Stork, B. Maschhoff, K. Nebesny, and N. Armstrong, Surf. Interface Anal. **17**, 48 (1991).
[47] G. Kurbatov, E. Darque-Ceretti, and M. Aucouturier, Surf. Interface Anal. **20**, 402 (1993).
[48] T.-C. Lin, G. Seshadri, and J. Kelber, Appl. Surf. Sci. **119**, 83 (1997).
[49] S. Tougaard and H. Hansen, Surf. Interface Anal. **17**, 593 (1991).
[50] A. Jablonski and H. Ebel, Surf. Interface Anal. **11**, 627 (1988).
[51] A. Jablonski, Surf. Interface Anal. **23**, 29 (1995).
[52] W. Werner, I. Tilinin, H. Beilschmidt, and M. Hayek, Surf. Interface Anal. **21**, 537 (1994).
[53] M. Seah and W. Dench, Surf. Interface Anal. **1**, 2 (1979).
[54] S. Tanuma, C. Powell, and D. Penn, Surf. Interface Anal. **11**, 577 (1988).
[55] S. Tanuma, C. Powell, and D. Penn, Surf. Interface Anal. **17**, 911 (1991).
[56] S. Tanuma, C. Powell, and D. Penn, Surf. Interface Anal. **20**, 77 (1993).
[57] P. Cumpson and M. Seah, Surf. Interface Anal. **25**, 430 (1997).
[58] G. Leibbrandt, L. Spiekman, and F. Habraken, Surf. Sci. **287**, 250 (1992).
[59] I. Tilinin, A. Jablonski, and W. Werner, Prog. Surf. Sci. **52**, 193 (1996).
[60] I. McCarthy, C. Noble, B. Philips, and A. Turnbull, Phys. Rev. **A 15**, 2173 (1977).
[61] I. Tilinin, Sov. Phys. JETP **67**, 1570 (1988).
[62] I. Tilinin, Phys. Rev. **A 51**, 3058 (1991).
[63] A. Jablonski and S. Tougaard, Surf. Interface Anal. **26**, 17 (1998).

[64] M. Takahashi and J. Igarashi, Phys. Rev. **B54**, 13566 (1996).
[65] P. Sewell, D. Mitchell, and M. Cohen, Surf. Sci. **33**, 535 (1972).
[66] C. Leygraf and S. Ekelund, Surf. Sci. **40**, 609 (1973).
[67] K. Ueda and R. Shimizu, Surf. Sci. **43**, 77 (1974).
[68] G. Simmons and D. Dwyer, Surf. Sci. **48**, 373 (1975).
[69] Y. Sakisaka, T. Miyano, and M. Onchi, Phys. Rev. B **30**, 6849 (1984).
[70] B. Sinkovic, P. Johnson, N. Brookes, A. Clarke, and N. Smith, Phys. Rev. Lett. **65**, 1647 (1990).
[71] G. Leibbrandt, S. Deckers, M. Wiegel, and F. Habraken, Surf. Sci. **244**, L101 (1991).
[72] A. Fromhold and E. Cook, Phys. Rev. **158**, 600 (1967).
[73] A. Fromhold and E. Cook, Phys. Rev. **163**, 650 (1967).
[74] G. Leibbrandt, P. Görts, and F. Habraken, Surf. Sci. **251/252**, 535 (1991).
[75] C. Brucker and T. Rhodin, Surf. Sci. **57**, 523 (1976).
[76] T. Guo and M. DenBoer, Phys. Rev. B **38**, 3711 (1988).
[77] *The Oxide Handbook*, edited by G. Samsonov (IFI/Plenum, New York, 1973).
[78] L. Ward, in *The Optical Constants of Bulk Materials and Films* (IOP Publishing, Bristol, 1988), Chap. 7, pp. 187–213.
[79] J. Jackson, in *Classical electrodynamics*, 2 ed. (Wiley, New York, 1975), Chap. 7, pp. 269–333.
[80] L. Ward, in *The Optical Constants of Bulk Materials and Films* (IOP Publishing, Bristol, 1988), Chap. 8, pp. 214–239.
[81] A. Vredenberg, C. Pérez-Martin, J. Custers, D. Boerma, L. de Wit, and F. Saris, J. Mater. Res. **7**, 2689 (1992).
[82] D. Inia, F. Feiner, W. Arnoldbik, A. Vredenberg, and D. Boerma, Surface & Coatings Technology **83**, 65 (1996).
[83] D. Inia, Ph.D. thesis, Debye Institute, Utrecht University, Utrecht, 1997.
[84] A. Fromhold, Langmuir **3**, 886 (1987).
[85] P. Görts, B. Dorren, and F. Habraken, Surf. Sci. **287/288**, 255 (1993).
[86] P. Görts, Ph.D. thesis, Utrecht University, 1995.
[87] S. Haupt and H.-H. Strehblow, Langmuir **3**, 873 (1987).
[88] J. Kruger and J. Calvert, J. Electrochem. Soc. **114**, 43 (1967).
[89] W. Arabczyk and U. Narkiewicz, Czech. J. Phys. **43**, 869 (1993).

[90] V. Battaglia and J. Newman, J. Electrochem. Soc. **142**, 1423 (1995).
[91] A. Stierle and H. Zabel, to be published in Surf. Sci. (unpublished).
[92] A. Fromhold, in *Oxides and oxide films*, Vol. 3 of *The anodic behavior of metals and semiconductor series* (Marcel Dekker, Inc., New York, 1976), Chap. 1, pp. 1–272.
[93] E. Verwey, Physica (Utrecht) **2**, 1059 (1935).
[94] A. Fromhold, Solid State Ionics **75**, 229 (1995).
[95] *CRC Handbook of Chemistry and Physics*, edited by R. Weast, M. Astle, and W. Beyer (CRC Press, Inc., Boca Raton, 1986).
[96] D. Dwyer and G. Simmons, Surf. Sci. **64**, 617 (1977).
[97] A. Baró and W. Erley, J. Vac. Sci. Technol. **20**, 580 (1982).
[98] W.-H. Hung, J. Schwartz, and S. Bernasek, Surf. Sci. **294**, 21 (1993).
[99] D. Dwyer, S. Kelemen, and A. Kaldor, J. Chem. Phys. **76**, 1832 (1982).
[100] M. Hendewerk, M. Salmeron, and G. Somorjai, Surf. Sci. **172**, 544 (1986).
[101] E. Murray and J. Kelber, J. Vac. Sci. Technol. **A 13**, 2558 (1995).
[102] M. Henderson, S. Joyce, and J. Rustad, Surf. Sci. **417**, 66 (1998).
[103] B. Maschhoff and N. Armstrong, Langmuir **7**, 693 (1991).
[104] D. Baer and M. Thomas, Appl. Surf. Sci. **26**, 150 (1986).
[105] G. Vidali, G. Ihm, H.-Y. Kim, and M. Cole, Surf. Sci. Rep. **12**, 135 (1991).
[106] V. Zhdanov, Surf. Sci. Rep. **12**, 185 (1991).
[107] S. Lombardo and A. Bell, Surf. Sci. Rep. **13**, 1 (1991).
[108] G. Brivio and T. Grimley, Surf. Sci. Rep. **17**, 1 (1993).
[109] M. Somers, B. Kooi, W. Sloof, and E. Mittemeijer, Mater. Sci. Forum **154**, 87 (1994).
[110] S. Rezaie-Serej and R. Outlaw, J. Vac. Sci. Technol. **A12**, 2814 (1994).
[111] J. Venables, G. Spiller, and M. Hanbrucken, Rep. Prog. Phys. **47**, 359 (1984).
[112] J. Venables, Phys. Rev. B **36**, 4153 (1987).
[113] B. Li, K. Griffiths, C.-S. Zhang, and P. Norton, Surf. Sci. **384**, 70 (1997).
[114] H. Brune, Surf. Sci. Rep. **31**, 121 (1998).
[115] P. Atkins, in *Physical Chemistry*, 5th ed. (Oxford University Press, Oxford, 1994), Chap. 27, pp. 928–959.

[116] S. Tougaard and B. Jørgensen, Surf. Sci. **143**, 482 (1984).
[117] D. Shirley, Phys. Rev. **B 5**, 4709 (1972).
[118] S. Tougaard and C. Jansson, Surf. Interface Anal. **20**, 1013 (1993).
[119] W. Werner, Phys. Rev. **52**, 2964 (1995).
[120] S. Tougaard, Solid State Commun. **61**, 547 (1987).
[121] S. Tougaard, Surf. Interface Anal. **11**, 453 (1988).
[122] S. Tougaard, Appl. Surf. Sci. **100/101**, 1 (1996).
[123] S. Tougaard and A. Jablonski, Surf. Interface Anal. **25**, 404 (1997).
[124] J. Lennard-Jones, Trans. Faraday Soc. **28**, 333 (1932).
[125] R. Vincent, Proc. R. Soc. London **A 321**, 53 (1971).

Summary

One of the most important metals on earth is iron: as the most important constituent of steel it is used for construction purposes, it is a valuable catalyst and it is important for its magnetic properties. Corrosion of iron is in most cases undesirable. This thesis investigates the oxidation of iron, one of the most important processes in corrosion. More specifically, the work presented in this thesis aimed at the understanding of the formation of the first 30 atomic layers of oxide on Fe(100) and Fe(110) by exposure to O_2 and H_2O vapor between room temperature and 473K (200℃).

In the introduction of this thesis, we described two drawbacks of the completest and physically most plausible oxidation theory appropriate for this system: **(1)** The Fromhold-Cook theory failed to predict correctly the saturation behavior of iron in O_2 at temperatures below 423K (150℃) and **(2)** the FC theory ignores the kinetics of surface processes such as the arrival, dissociation, recombination and desorption of the O containing gas molecules.

For the characterization of the oxide layer grown, among others quantitative XPS was used in this thesis. In chapter 3, we used quantitative XPS to determine the (average) stoichiometry of the oxide layers grown in O_2 to be $Fe_{0.9}O$. Using a combination of quantitative XPS and ERD, we determined the Attenuation Lengths (AL) of photoelectrons in this iron oxide (in an exponential approximation of the DDF). The ALs found amounted to 9.3×10^{15} O atoms/cm^2 (1.96 nm) at 776 eV (Fe(2p) peak) and 9.9×10^{15} O atoms/cm^2 (2.08 nm) at 957 eV (O(1s) peak). These values are about 10% smaller than predicted by the empirical formula by Seah and Dench. Better agreement was obtained for the Inelastic Mean Free Path (IMFP) of the photoelectrons calculated from the value of the AL, when compared with Tanuma's semi-empirical relation. Knowledge of the values of the AL are important for the quantification of XPS results and, moreover, the ex-

trapolation of the fitted curves to slightly higher electron energies provided us with a value for the AL of N(1s) photoelectrons needed in our marker layer experiments in chapters 5 and 7.

Chapters 4 and 5 describe the oxidation of Fe(100) and Fe(110) in O_2. The most important observation in chapter 4 is the simultaneous change in Fe oxidation state (in the oxide layer, from mainly Fe^{2+} to both Fe^{2+} and Fe^{3+}), refractive index and oxidation mechanism at $N_O = 4{\times}10^{15}$ atoms/cm^2. This was explained with the nucleation and growth of oxide clusters for $N_O < 4{\times}10^{15}$ atoms/cm^2. Typical nucleation and growth kinetics was not observed, because the oxidation rate is limited by the arrival of O atoms from the O_2 gas. Both processes are not included in the FC theory. For $N_O > 4{\times}10^{15}$ atoms/cm^2, where the oxidation rate starts to decrease, an oxide layer containing both Fe^{2+} and Fe^{3+} (stoichiometry $Fe_{0.77}O$) is formed on top. Here, the conditions for applying the FC theory are met: N marker layer experiments reveal that Fe is the mobile species and the reaction between O and Fe takes place at the surface.

Still, the observed saturation behavior differs from the prediction of the FC theory. This temperature dependent saturation thickness is explained in chapter 5 by the (temperature dependent) presence of Fe^{3+}. By annealing in vacuum at 473K (200°C), all Fe^{3+} present in the layer is reduced to Fe^{2+} and the room temperature growth of a homogeneous FeO layer can be compared with the FC theory. Indeed, we find that the presence of Fe^{3+} leads to the "early" saturation: after reduction of Fe^{3+}, agreement was obtained with the FC theory. Using a single parameter set, we were able to fit the oxidation rates at room temperature, 435K (162°C) and 473K (200°C). For the room temperature oxidation, the transport of Fe cations through the oxide layer determines the rate for oxygen coverages from $4{\times}10^{15}$ atoms/cm^2 to $12{\times}10^{15}$ atoms/cm^2. The presence of Fe^{3+} influences the maximum cation diffusion current. (A change in electron conductivity due to Fe^{3+} could be ruled out within the framework of the FC theory, because of non-physical parameter values needed to describe the observed saturation.) The decrease of the oxidation rate enhances the formation of Fe^{3+}, which in a self-amplifying combination of processes reduces the oxidation rate even further. In conclusion, the deviations from the FC theory at $T < 423$K (150°C) were due to the inhomogeneity of the oxide films formed at these temperatures: the system is not a model system for the theory.

Neither is the oxidation of Fe(100) in H_2O vapor. The measurements presented in chapters 6 (room temperature) and 7 (temperature dependence) revealed that during the oxidation in H_2O at room temperature, hydrogen is taken up, probably as OH groups in the oxide layer. The oxidation rate in H_2O which is 3 orders of magnitude lower than the oxidation rate in O_2, is entirely determined by the earlier mentioned surface processes: the oxidation could be completely described with a nucleation and growth model containing rate equations for the surface reactions. The oxidation rate reaches a maximum at $T = 340$K (67℃). Below this temperature, H_2 desorption (from H atoms at the surface) determines the oxidation rate. Above 340K, the decrease of the oxidation rate is due to the recombination of OH and H at the surface and subsequent desorption of H_2O. The rate limiting step is the dissociation of OH at step edges. Further evidence for this model is formed by the oxidation rate of Fe(100) covered with N marker atoms, which were found to facilitate the nucleation and growth of the oxide islands. Experiments where H_2O was replaced with D_2O revealed a distinct isotope effect, which is due to a different energy barrier for one of the surface processes, but possibly also due to a lower exponential prefactor (in an Arrhenius description of rate constants) corresponding to a lower molecular vibration frequency in the D_2O molecule or OD surface species (compared with H_2O of OH, respectively). Again, the differences could be explained completely by surface processes.

The transport properties of the oxide layers formed in H_2O at room temperature, as probed by subsequent oxidation in O_2, could be described in the FC model. The lower oxidation rates (compared with oxide layers formed in O_2, to the same O coverage) could be partly attributed to the effect of Fe^{3+} present in the layer. In addition, the incorporation of H in the layer was shown to lead to a lower oxidation rate as well: both H and Fe^{3+} affect the cation diffusion properties of the oxide layer.

Similar effects were observed for the oxidation of Fe(100) in H_2O/O_2 mixtures. After an initial stage in which the oxidation rate is completely determined by the arrival rate of O_2 molecules, the oxidation decreases and a saturation coverage is reached, which decreases with increasing H_2O vapor partial pressure. However, in this case it was shown that the effect was entirely due to the amount of Fe^{3+} present in the oxide.

Samenvatting

IJzer is het meestvoorkomende metaal op aarde en is sinds de ijzertijd niet meer weg te denken als materiaal voor gebruiksvoorwerpen en in de bouw. Staal bestaat voornamelijk uit ijzer. Bovendien is ijzer een waardevolle katalysator en het is belangrijk vanwege de magnetische eigenschappen. Bij veel toepassingen van ijzer is corrosie, de aantasting van een vaste metaal door chemische reacties met de omgeving, een probleem. Oxidatie is een van de belangrijkste deelprocessen van corrosie: Bij blootstelling van ijzer aan zuurstof bevattende gassen zoals zuurstof (O_2) of waterdamp (H_2O) wordt aan het oppervlak een dunne oxidelaag gevormd.

De chemische en fysische eigenschappen van deze slechts enkele nanometers dunne oxidefilm op het metaal zijn van groot praktisch belang: ze spelen een doorslaggevende rol in, bijvoorbeeld, slijtage en wrijving, het broos worden van staal onder invloed van waterstof, het degraderen van materialen voor waterstofopslag en de passivering van ijzer. Maar ook bij de produktie en werking van moderne electronische componenten worden de eigenschappen van deze oxidelagen steeds belangrijker naarmate de schaalverkleining van deze componenten voortschrijdt.

Daarom is de groei van oxide op ijzer en andere metalen en legeringen uitgebreid bestudeerd. Er is een groot aantal experimentele en theoretische artikelen verschenen over de interacties tussen oxiderende gassen (O_2, H_2O) en metaaloppervlakken bij hoge temperaturen (meer dan 500℃). Bij deze temperaturen verloopt de oxidatie snel en kunnen relatief dikke oxidelagen gevormd worden, die met traditionele experimentele methoden (bijvoorbeeld volumetrie of gravimetrie) gemeten kunnen worden.

Voor lagere temperaturen en dunnere oxidelagen (dunner dan 1 μm, een duizendste millimeter) is de kennis over oxidatiekinetiek (reactiesnelheid en -mechanisme) incompleet. Hoewel er sinds de mogelijkheid ultrahoog vacuüm te bereiken veel experimentele studies zijn gedaan naar het

ontstaan van de eerste atoomlaag van het oxide, zijn er weinig betrouwbare experimentele studies van oxidegroei in het tussengebied, voornamelijk omdat er geen experimentele technieken waren die gevoelig zijn in het hele gebied tussen enkele atoomlagen en enkele μm. Ook was voor de introductie van ultrahoog-vacuümsystemen het prepareren van schone metaaloppervlakken (zonder natuurlijke oxidehuid) onmogelijk.

Desondanks is in de laatste veertig jaar een aantal verschillende oxidatietheorieën bedacht. De meest veelbelovende van deze theorieën is de zogenaamde Fromhold-Cook-theorie (FC), ontwikkeld door Fromhold en Cook in de jaren zestig. Niet alleen is deze theorie natuurkundig consistent, men kan ook laten zien dat verschillende oudere theorieën limietgevallen van de FC-theorie zijn. In de FC-theorie wordt de snelheid van oxidatie gegeven door de mate waarin elektronen en metaalionen door de dunne oxidehuid het oppervlak kunnen bereiken. Een belangrijk ingrediënt in de FC-theorie is de eis dat er ladingsevenwicht is, dat wil zeggen dat de hoeveelheid lading die per tijdseenheid aan het oppervlak arriveert nul is. Omdat de elektronen negatief geladen zijn en de metaalionen positief, kan op deze manier voor elke oxidedikte de oxidatiesnelheid uitgerekend worden met behulp van uitdrukkingen voor de diffusie van metaalionen en het tunnelgedrag (bij temperaturen lager dan 150°C) of de thermionische emissie (bij temperaturen boven 150°C) van de elektronen.

In 1992 was reeds aangetoond dat de oxidatie van het (100)-kristaloppervlak van ijzer in zuurstofgas (O_2) bij temperaturen boven 150°C voldoet aan de voorwaarden om de FC-theorie te kunnen toepassen: de reactie tussen ijzer en zuurstof vindt plaats aan het oppervlak van het gestaag dikker wordende oxide dat bestaat uit FeO. Met realistische waarden voor de verschillende parameters voorspelt de FC-theorie nauwkeurig de gemeten oxidatiecurven en de temperatuursafhankelijkheid van de oxidatie. Voor temperaturen beneden 150°C, waar het elektrontransport geschiedt door tunneling door de barrière van de oxidehuid, geeft de FC-theorie oxidatiesnelheden die afwijken van wat gemeten is. De gemeten en berekende oxidatiecurves lijken wel op elkaar qua vorm, maar in tegenstelling tot wat de FC-theorie voorspelt, laten de metingen een duidelijke temperatuursafhankelijkheid zien van de verzadigingsdikte (de dikte van de oxidelaag waar de zuurstoftoename onder 10^{11} atomen cm^{-2} s^{-1} komt).

In dit proefschrift wordt aangetoond dat deze afwijking van de theorie ontstaat doordat de oxidatietoestand van het ijzer in oxidelagen (gevormd

in O_2) bij deze temperaturen niet overal in de gevormde oxidelaag gelijk is. Bij oxidatie op kamertemperatuur bestaat de oxidehuid uit twee lagen: een laag die alleen Fe^{2+} bevat, die als eerste gevormd wordt, en daarbovenop aan het oppervlak een laag die zowel Fe^{2+} als Fe^{3+} bevat. De aanwezigheid van dit Fe^{3+} resulteert in een drastische verlaging van de oxidatiesnelheid. Dit komt, doordat de bovenlaag met Fe^{3+} bijna ondoordringbaar is voor ijzerionen. Door de gevormde dubbellaag te verhitten tot 200℃ in vacuüm, kan het Fe^{3+} omgezet worden in Fe^{2+} (reductie) zonder dat de dikte van de oxidelaag verandert. Na afkoeling tot kamertemperatuur kan het aldus ontstane systeem weer worden blootgesteld aan zuurstof en door dit oxideren en verhitten een aantal malen te herhalen hebben wij de vormingssnelheid van een FeO-laag (met alleen Fe^{2+}) bestudeerd en gevonden dat de vorming van FeO ook op temperaturen beneden 150℃ in overeenstemming is met wat het FC-model voorspelt, met dezelfde parameterwaarden als voor hogere temperaturen.

De FC-theorie beschouwt alleen de snelheid van de transportprocessen door de oxidelaag. Voor de oxidatie van ijzer in zuurstof gaat dit goed omdat de dissociatie van de O_2-moleculen veel sneller verloopt dan deze transportprocessen. In een systeem waar de oppervlakteprocessen zoals adsorptie, dissociatie van het gasmolecuul, recombinatie en desorptie trager verlopen, moet ook de snelheid van deze reacties in rekening gebracht worden. Door de verschillende aankomst- en vertrekfrequenties en de aankomst van ijzerionen en elektronen door de oxidelaag, vormt zich aan het oppervlak een complex evenwicht van atomen en moleculen, dat de drijvende kracht voor de oxidatie vormt. In principe zou dit gehele evenwicht beschouwd moeten worden voor een complete beschrijving van het oxidatieproces.

In dit proefschrift wordt aangetoond dat voor de oxidatie van het (100)-oppervlak van een ijzerkristal in waterdamp (H_2O) volstaat de oppervlakteprocessen te beschouwen; de aanvoer van ijzerionen en elektronen is altijd voldoende en hoeft niet in de beschrijving opgenomen te worden. De eerste atoomlaag van zuurstofatomen aan het ijzeroppervlak ontstaat binnen 250 seconden, hetgeen met de hier gebruikte experimentele methoden slechts gedeeltelijk kan worden waargenomen. De experimentele resultaten voor de groei na de eerste zuurstoflaag, die in waterdamp drie ordes van grootte langzamer verloopt dan in zuurstof, kunnen volledig verklaard worden met een model waarin watermoleculen aan het oppervlak uiteen-

vallen in hydroxylgroepen (OH) en waterstofatomen (H). Zowel OH als H reizen enige tijd over het oppervlak. Wanneer ze elkaar tegenkomen, kunnen ze weer een H_2O-molecuul vormen. Ontmoeten twee H-atomen elkaar, dan kan een waterstofmolecuul (H_2) gevormd worden, dat vervolgens in de gasfase verdwijnt (desorbeert). Twee OH-groepen kunnen een oxidekiem vormen, waarbij één zuurstofatoom reageert met ijzer, en het andere met de waterstofatomen een H_2O-molecuul vormt. OH-groepen die arriveren aan kiemranden, kunnen met achterlating van een waterstofatoom reageren met ijzer en zodoende de kiem vergroten. Deze combinatie van reacties leidt tot kiemvorming en -groei en typische oxidatiecurven: de oxidatie verloopt langzaam wanneer er nog weinig kiemen zijn, versnelt dan wanneer de kiemen groter worden en vertraagt weer wanneer de kiemen beginnen samen te smelten, totdat het gehele oppervlak met kiemen bedekt is en de oxidatie niet meer kan verlopen. In dit proefschrift wordt een kwantitatief model gegeven voor deze reacties, dat met realistische parameterwaarden de juiste temperatuurs- en drukafhankelijkheid van de oxidatiesnelheid voorspelt voor het eerste deel van de oxidatie (totdat de kiemen ongeveer eenderde van het oppervlak bedekken). Het samensmelten van de kiemen en de daarmee gepaard gaande vertraging van de oxidatie kon helaas niet op realistische wijze in het model gebracht worden.

De transporteigenschappen van de oxidelagen die gevormd worden op kamertemperatuur in H_2O verschillen van eigenschappen van in O_2 gevormde lagen. Dit is aangetoond door een dunne oxidelaag op het Fe(100)-oppervlak te maken door oxidatie in waterdamp, en deze laag vervolgens aan O_2 bloot te stellen: de oxidatiesnelheid is veel lager dan in het geval van een even dikke laag die in O_2 is gevormd. Wij hebben aangetoond dat dit komt doordat de in H_2O gevormde laag minder goed doordringbaar is voor ijzerionen. Dit is het gevolg van de aanwezigheid van Fe^{3+} (dat bij deze dikte in O_2 nog niet gevormd is), maar ook van de opname van waterstof in de oxidelaag (in de vorm van OH-groepen). Deze effecten kunnen binnen het FC-model verklaard worden. Bij de oxidatie in H_2O/O_2-mengsels kunnen verschillende stadia onderscheiden worden. De groeisnelheid van de eerste twee atoomlagen wordt volledig bepaald door de aanvoersnelheid van zuurstof uit O_2. Voor dikkere lagen neemt de oxidatiesnelheid af en deze afname is sterker naarmate de verhouding H_2O/O_2 in het gasmengsel hoger is (bij gelijkblijvende totaaldruk). We hebben aangetoond dat deze afname gekoppeld is aan de totale hoeveelheid Fe^{3+} in de gevormde oxidelaag.

List of Publications

Publications Related to this Thesis

S.J. Roosendaal, A.M. Vredenberg, and F.H.P.M. Habraken, *The Influence of Adsorbed N on the Initial Stages of Oxidation of Iron*, Surf. Sci. **402-404**, 135-139 (1998)

S.J. Roosendaal, I.A.M.E. Giebels, A.M. Vredenberg, and F.H.P.M. Habraken, *Determination of Photoelectron Attenuation Lengths in Thin Oxide Films on Iron Surfaces using Quantitative XPS and Elastic Recoil Detection*, Surf. Interface Anal. **26**, 758-765 (1998)

S.J. Roosendaal, B. van Asselen, J.W. Elsenaar, A.M. Vredenberg, and F.H.P.M. Habraken, *The Oxidation State of Fe(100) after Initial Oxidation in O_2*, accepted for publication in Surf. Sci.

S.J. Roosendaal, A.M. Vredenberg, and F.H.P.M. Habraken, *The Role of the Surface Electronic Structure in the Oxidation of Iron*, accepted for publication in Surf. Rev. Lett.

S.J. Roosendaal, A.M. Vredenberg, and F.H.P.M. Habraken, *Oxidation of Iron: the Relation between Oxidation Kinetics and Oxide Electronic Structure*, submitted for publication.

Other Publications

C.H.M. Marée, S.J. Roosendaal, T.J. Savenije, R.E.I. Schropp, T.J. Schaafsma, and F.H.P.M. Habraken, *Photovoltaic Effects in Porphyrin Films and Heterojunctions*, J. Appl. Phys. **80**, 3381-3389 (1996)

H.J. Whitlow, S.J. Roosendaal, M. El Bouanani, R. Ghetti, P.N. Johnston, B. Jakobsson, R. Hellborg, H. Petersson, P. Omling, Z. Wang, and the CHIC collaboration, *Effects of Energy Deposition by Nuclear Scattering in Silicon p-i-n Diode Detectors*, Nucl. Instr. Meth. **B 135**, 523-531 (1998)

Bedankt!

Wie het doen van promotie-onderzoek ziet als een ontdekkingsreis, moet zich realiseren dat de ontdekkingsreiziger niet alleen op pad gaat. Een groot aantal mensen heeft in meer of minder direkte mate aan de totstandkoming van dit proefschrift bijgedragen. Dit is de plaats om iedereen te danken.

Allereerst mijn promotor Frans Habraken voor zijn spreekwoordelijke enthousiasme. Frans, ik heb je leren kennen als een gedegen experimentator, die altijd weer nieuwe experimenten wist te verzinnen, maar ook als een begeleider die het overzicht wist te behouden, met een goed oog voor de te beklimmen hellingen die inderdaad de mooiste uitzichten boden.

Arjen Vredenberg voor de dagelijkse begeleiding en vooral voor de *close-reading* van mijn werk, of dat nu kwam in de vorm van artikelen, figuren, modellen of proefschrift. In onze expeditie was jij de spoorzoeker met het oog voor detail, de indiaan met de sluipende tred, voor wie geen geknakt takje of vertrapt blaadje onopgemerkt blijft.

Veel dank ben ik verschuldigd aan Theo Klinkhamer voor de technische ondersteuning bij de Octopus. Jouw systematische en degelijke manier van werken en documenteren heeft de Octopus voor veel rampspoed behoed en je afkeer van 'tijdelijke' oplossingen stond garant voor heel veel meetplezier. Defecte kasten met electronica kon ik aan Wim de Kruif kwijt, die dan altijd een oplossing wist. Door zijn werk aan het automatiseren van het uitstoken en de beveiliging van de opstelling heeft hij ook veel bijgedragen aan mijn nachtrust.

'Mijn' studenten Bas, Ingrid, Bram, Jeroen, Jan Willem en Roel zullen veel van de in dit proefschrift gepresenteerde meetresultaten herkennen. Bedankt voor alle hulp bij het sleutelen aan de Octopus, het experimenteren en vooral voor de teamgeest.

Mijn kamergenoten waren achtereenvolgend Dieuwert Inia, Jeroen van Hapert en Edwin van der Wal: we hielden elkaar van het werk met zeer

gewaardeerde discussies over vakantie, sport, politiek en de leegte van de muur aan jullie kant van de kamer, maar ook over foutenrekening, achtergrondaftrek in alle soorten spectra en vergeten onderwerpen uit de middelbare-school-natuurkunde.

Wim Arnold Bik wil ik bedanken voor al die handige routines die beginnen met de letter *w*, voor al die keren dat hij mij (meestal in vliegende vaart) hielp met een umac-probleem, maar vooral voor zijn kennis van ionenbundeltechnieken, versnellers en detectoren, zonder welke het bij elkaar meten van dit proefschrift heel wat moeilijker geweest zou zijn.

Henk Kersemaekers, Gerard van Gelder, Ruud van Stappershoef en Flip van der Vliet bedankt voor het maken van de ionenbundels op de Tandem en de 3MV. Flip zorgde niet alleen voor de ionenbundels op de 3MV, maar ook voor knaleffecten en een keer zelfs een koelwaterfontein in de buurt van mijn opstelling, maar bleek uiteindelijk altijd alles perfect onder controle te hebben.

Peter Görts en Peter Graat hebben mij wegwijs gemaakt op de Octopus. Peter Graat en Lars Jeurgens vormden het Delftse oxidatieduo: met jullie was het altijd aangenaam discussiëren was over oxidatiemodellen, over de onzinnige aannames in sommige daarvan en over de verschillen tussen aluminium en ijzer.

Ernst, Renée, Dieuwert, Kees, Jeike en Jatin hebben mij laten zien dat de Octopus niet alleen geschikt is voor onderzoek naar de oxidatie van ijzer.

Renée Heller voor de gezamenlijke pizzabol-diners en voor het altijd open staan voor onzin, gezeur en serieuzere zaken. Veel succes met de laatste loodjes van je proefschrift.

Iedereen van de sectie Grenslaagfysica voor de goede werksfeer, het onwetenschappelijke én wetenschappelijke commentaar tijdens koffiepauze, lunch en werkbespreking.

Alle medewerkers van de audiovisuele dienst van Chemie voor het omzetten van vage, smoezelige schetsjes en met de hand bijgekrabbelde tekst in prachtige, oogstrelende posters en voor het uitwerken van mijn schetsontwerp van het omslag van dit proefschrift.

Mijn vrienden voor de afleiding, de gezelligheid en de ‘onthaasting’, in het bijzonder paranimfen Mark Schreijen en Arjan Buist.

Mijn ouders voor de interesse in mijn werk en de steun gedurende mijn promotietijd.

En, natuurlijk, Romana voor alle steun en liefde.

Curriculum Vitae

Sander Jurgen Roosendaal kwam op 19 april 1972 ter wereld in Amstelveen. In 1990 haalde hij het VWO-diploma aan het Goois Lyceum te Bussum. Aansluitend studeerde hij natuurkunde aan de Universiteit Utrecht. De titel van zijn afstudeeronderzoek, verricht in 1994/1995 bij de vakgroep Atoom- en Grenslaagfysica, was *Characterization of thin porphyrin layers for organic solar cells*. In 1995/1996 deed hij in het kader van het *Erasmus*-programma experimenteel onderzoek naar de degradatie van silicium *p-i-n*-deeltjesdetektoren voor het Zweedse onderzoeksprojekt *CHICSI* in de vakgroep Kernfysica van Lunds Universitet, Lund, Zweden. In april 1996 behaalde hij het doctoraalexamen Experimentele Natuurkunde (Cum Laude). Vanaf april 1996 was hij als onderzoeker-in-opleiding bij de stichting voor Fundamenteel Onderzoek der Materie (FOM) aangesteld in de sectie Grenslaagfysica van het Debye Instituut, Universiteit Utrecht. De resultaten van het daar verrichte onderzoek onder begeleiding van Prof. dr. F. H. P. M. Habraken en Dr. A. M. Vredenberg vormen de basis van dit proefschrift. Naast het uitvoeren van onderzoek gaf hij werkcolleges natuurkunde aan eerste- en tweedejaars studenten scheikunde. In januari 2000 zal hij in dienst treden bij het Natuurkundig Laboratorium van Philips Electronics Nederland B.V. te Eindhoven.